Fakultät für Physik
Technische Universität München
Institut Laue-Langevin

# A Versatile Device for Studying Ultracold Neutrons and Testing Cryogenic Storage Volumes

Master Thesis in Physics
submitted by

Jürgen Hingerl

Technische Universität München

January 7, 2019

| | |
|---|---|
| Reviewer: | Prof. Dr. P. Fierlinger |
| Second Reviewer: | Prof. Dr. P. Boeni |
| Advisor: | Dr. Oliver Zimmer |

# Erklärung zur Selbstständigkeit

Ich versichere hiermit, dass ich die von mir eingereichte Abschlussarbeit selbstständig verfasst und keine anderen als die angegebenen Quellen und Hilfsmittel benutzt habe, die wörtlich oder inhaltlich übernommenen Stellen als solche kenntlich gemacht.

München, den 7. Januar 2019, _____

Jürgen Hingerl

# Abstract

With ultracold neutrons (UCN) many questions in fundamental physics are investigated. To obtain precise answers at high confidence level within realistic measurement times, high UCN densities are needed. Highest UCN densities are achieved using thermal sources, whereas highest UCN densities are nowadays achieved in superthermal sources. While thermal sources are already almost at their limit, the density delivered by superthermal sources could be greatly increased by optimization of the wall material of the production volume. However, for both sources the efficiency of the neutron handling elements between the sources and the experiments also are a significant factor to achieve high densities.
To optimize the delivered neutron density at the experiment, in this thesis the efficiency and optimization of a new ∅50 mm neutron handling system are investigated. The velocity dependent neutron transmission was measured from zero to $20\,\frac{\mathrm{m}}{\mathrm{s}}$ using a time of flight set-up in horizontal and vertical alignment.
Characterization of the handling system includes transmission of various highly polished stainless steel guide elements and bends. In addition the transmission of glass guides coated with NiMo and non depolarizing Cu was measured. Within this work, a three way neutron switch has been designed, commissioned and characterized with neutrons.
In addition the by theory imposed $1/v^2$ transmission dependence on surface roughness and to improve the delivered UCN beam and to increase its the detection efficiency towards slower neutrons, the transmission of a thin aluminum foil before and after polishing was measured.
Increasing the density in the production volume of superthermal sources, a set-up for storage lifetime measurement consisting of the characterized components has been developed as a test facility. The mechanical design accommodates any shape of storage bottles at ambient and cryogenic temperatures. For initial testing, a storage bottle with the same dimensions as the UCN source prototype SUN II is coated with a fluoropolymer called CYTOP, whose UCN properties were so far unknown. Its neutron optical potential characteristics is similar to Fomblin grease/liquid. This material is expected to resolve the problems of surface thickness uniformity and defects while remaining compatible with operation at cryogenic temperatures. The measurements presented in this work reveal a promising effective lifetime of $\tau_{\mathrm{eff}} = (200 \pm 98)\,\mathrm{s}$ at room temperature. Also, an additional cooling test of the bottle mounted in the test set-up has been successfully conducted. This strengthens the case for CYTOP as coating material for superthermal sources at cryogenic temperatures.

# Contents

*Nix g'wiss woas ma ned*

$$\Delta x \cdot \Delta p \geq \hbar$$

# 1. Introduction

## 1.1. Physics with Ultracold Neutrons

A broad range of scientific fields from condensed matter and biological science up to nuclear and particle physics is impacted by neutron physics. Certain questions in fundamental physics can be investigated using neutrons with velocities below $5\,\frac{\mathrm{m}}{\mathrm{s}}$ whose energies correspond to cryogenic temperatures, therefore are called ultracold neutrons UCN. At these energies neutrons undergo total reflection on surfaces under any angle of incidence and thus can be stored in closed vessels or containers with walls higher than its energy. This enables experiments that study them an extended period of time, much longer than achievable in beam experiments.
A main field investigated with high precision UCN measurements is the search for a non zero electronic dipole moment as predicted by the standard model and theoretical extensions of it. This would violate the combined charge conjugation (C) and parity (P) symmetry and potentially address the huge discrepancy between matter and antimatter.
Another point of interest is the neutron lifetime and corresponding angular correlation measurements of neutron $\beta$-decay which provide information about the weak interactions and the creation of elements in our universe. This sets the timescale where hydrogen can absorb neutrons and built heavier isotopes which is the start of Big Bang nucleosynthesis.
The quantum states of neutrons in the Earth's gravitational field, as well as the transmission between the exited and ground state are probed, testing Newtons law of gravity on a micro scale and testing models of dark energy.
Besides fundamental research, UCN optics and interference effects can be used as an extension for the study of condensed matter.
In order to successfully conduct high precision UCN measurements at high confidence levels a high UCN count rate at the experiment is needed, implying use of powerful UCN sources. Therefore, huge efforts are taken to further optimize the UCN output of operating and prospective high density UCN sources, as well as to deliver directed UCN with the least possible loss from the source into the experiments.

## 1.2. UCN Production

Free neutrons are not stable and thus they have to be extracted from bound states inside a nucleus, since the energy available in neutron decay is lower than the energy needed to insert another proton inside the nucleus. This extraction is done either by using nuclear fission at nuclear research reactors such as the Institute Max von Laue - Paul Langevin (ILL) in Grenoble or at spallation sources like the to be built European Spallation Source (ESS) [1].
At research reactors the liberated fast neutrons (2 MeV) are thermalized within the moderator tank to 20 meV. A small fraction is further cooled at cold sources, which are located inside the moderator tank. Where the cold neutron (CN) regime at about 2 meV is reached by use of liquid hydrogen or deuterium as moderator material. To get a high UCN flux above the limit of the lower tail of the Maxwell-Boltzmann spectrum an additional process is needed. Up to now there exist two different basic concepts: Thermal sources, which provide a constant UCN beam; and superthermal sources, which can deliver higher UCN densities in slow pulsed operation.

### 1.2.1. Thermal Sources

At thermal sources UCNs are obtained by extracting neutrons from the lower energy tail of the Maxwell-Boltzmann distribution of a cold source. The energy of these extracted neutrons is further reduced by guiding the neutrons several meters upwards in the Earth's gravitational field reaching the very cold neutron (VCN) regime. The transition from VCN with velocity $v_\mathrm{n}$ to UCN with velocity $v'_\mathrm{n}$ is achieved by reflection on moving surfaces with a velocity $u \approx v_\mathrm{n}/2$ giving a final neutron velocity of

$$v'_\mathrm{n} = v_\mathrm{n} - 2u \approx 0 \tag{1.1}$$

Since the phase space is only shifted, the final UCN density delivered at the experiment is always limited by the cold neutron production and losses of the guiding system.

#### Steyerl Turbine

The typical example for thermal sources is the neutron turbine at the Institute Max von Laue - Paul Langevin (ILL), which was built in 1986 by Steyerl and is still in operation, providing an UCN density of 50 UCN/cm$^3$ [2]. In figure 1.1 a schematic drawing of the basic parts of the source is depicted.
Neutrons with velocities at 50 $\frac{\mathrm{m}}{\mathrm{s}}$ are vertically extracted from the cold source and are guided upwards by a curved guide to slow down the neutrons using the gravitational interaction (see sec. 2.1.3). The curvature of the guide reduces the high energy neutron and $\gamma$ flux at the exit. At the upper end of the guide the Steyerl Turbine is installed consisting of many nickel coated reflecting mirror blades mounted on a wheel. This is rotating away from the incoming beam at approximately half the speed of the incident beam. Incoming neutrons bouncing on the blades lose most of their remaining kinetic energy according to equation (1.1). Due to the geometry of the blades the UCN flux is directed towards the four UCNbeam ports of the turbine. The VCN and TES beam are run in constant parasitic mode, while between the EDM, UCN and MAM the beam is switched to provide ten times higher UCN flux at reduced duty factor at the experiments [2]. More detailed information on relevant techniques and characterizations can be found in [3] and [4].

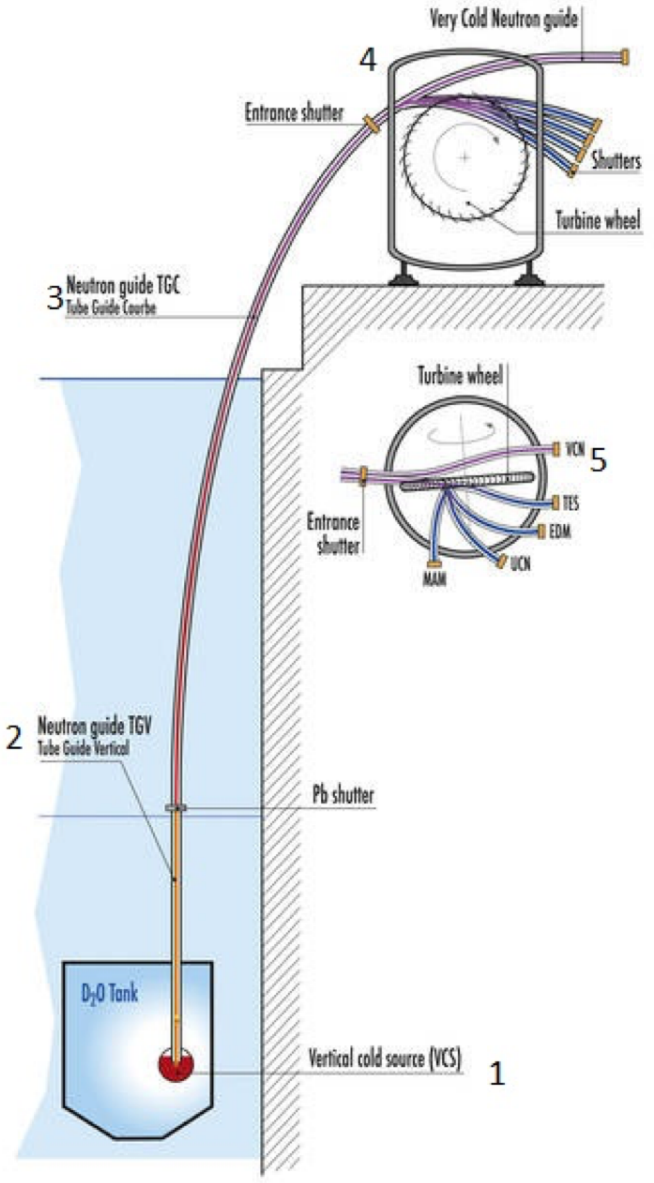


**Figure 1.1.:** Drawing of the Steyerl Turbine installed at the PF2 at the ILL [2] showing the extraction of clod neutrons CN from the cold source inside the moderator tank (1) and the vertical (2) and curved guide (3) to the turbine. When the shutter (4) is opened the remaining very cold neutrons (VCN) are shifted towards the UCN regime and are directed to the beam ports (5).

### 1.2.2. Superthermal sources

In contrast to thermal sources at superthermal sources, the neutrons are not in thermal equilibrium with the moderator. In cryogenic converter media, which is in most cases solid deuterium ($sD_2$) or superfluid $^4$He. The incoming neutrons that are resonant for the donwscattering process guided lose almost their entire energy in single scattering events The heat load implanted inside the moderator material, usually phonons, is removed by actively cooling the converter. Due to detailed balance scattering of UCN back to higher energies is suppressed, and thus the phase space density increases until it reaches an equilibrium value. This is limited by losses inside the moderator vessel. For a perfect loss-less vessel the limiting loss would be ultimately the free neutron lifetime of 880 s [5]. Since loss rates in $^4$He can in principle approach this value, this kind of source can be installed at the end of a cold neutron guide while still producing relatively high UCN densities. On the other hand, in $sD_2$ the neutron life time is less then a second due to absorption and thus this kind of source most typically are installed close to a reactor core or near a spallation target. In superthermal sources high UCN densities of up to 220 $cm^{-3}$ can be achieved [6], but a major issue is the efficient extraction of the neutrons to provide high densities at an experiment. Up to now this is over come by using them in pules mode where high densities are accumulated inside the storage volume for a defined time and then the UCN outlet is opened and the neutrons propagate towards the experiment where the count rate after opening follows an exponential decay. Therefore, at experiments in need of a constant high directed UCN flux its usage is up to now limited.

#### SUN

An example of a superthermal UCN $^4$He source superthermal ultracold neutron source (SUN) is operating at the cold neutron beam lines H172a at ILL developed by Zimmer [7] ( see fig. 1.2). Which has reached a UCN density at the production volume of up to 55 UCNcm/$^3$ [8] in the first stage SUN I and is reaching 220 UCNcm/$^3$ in the second SUN II [6].
The aluminum converter vessel is filled with approximately 7 liters $^4$He cooled below 1 K by a cryostat. Before entering the production volume the CN beam is energy selected with a monochromator for the resonant neutron energy of 1 meV that can be scattered down, due to the kinematics of the dispersion relation of He and neutrons (see fig. 1.3). Energy selection avoids additional heat load caused by the non resonant scattered neutrons. Som CN at higher energies are also scattered down via multiphonon processes leading to a broadening of the gained UCN spectra.
Inside the converter vessel of SUN I a BeO ceramic and SUN II a fomblin coated aluminum volume is located where the produced UCN are accumulated. The UCNs are extracted at a hole in the top of the storage bottle by opening a UCN shutter valve which is connected to the outlet of the bottle via a short section of highly polished steel. The UCNs are further guided through a set of steel tubes into the experiments at a maximum rate for SUN I 1400 UCN/s [8].

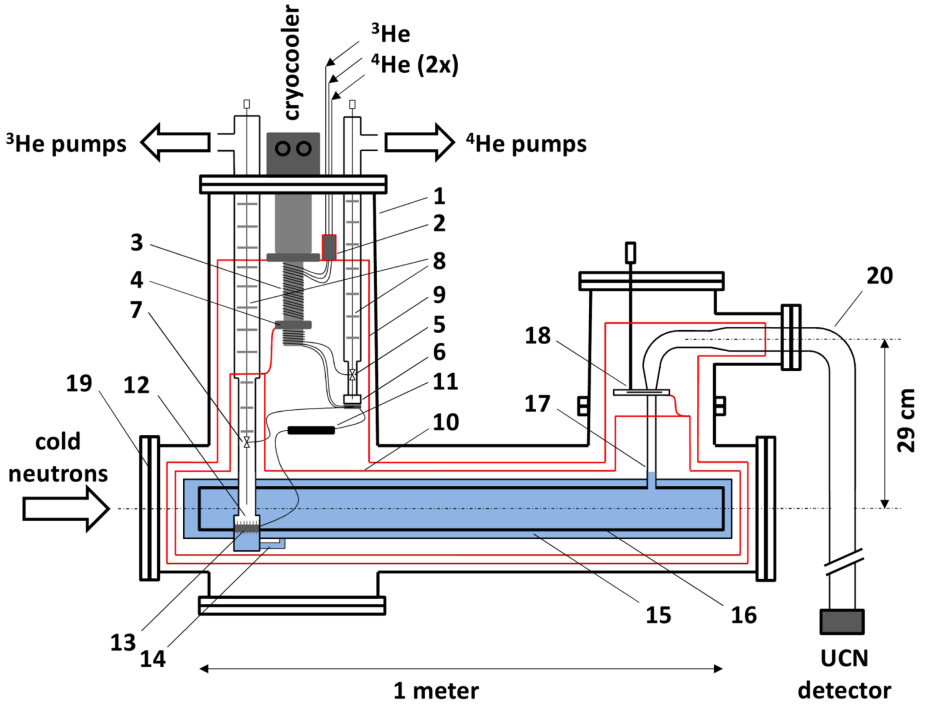


**Figure 1.2.:** Schematic drawing of the superthermal UCN source SUN II at the ILL [8] with the incoming cold neutron beam from the left side and the converter vessel (15) indicated in blue with the storage volume (16) and the neutron outlet (17) with the shutter mechanism above (18). The full description of all depicted components can be found in [8].

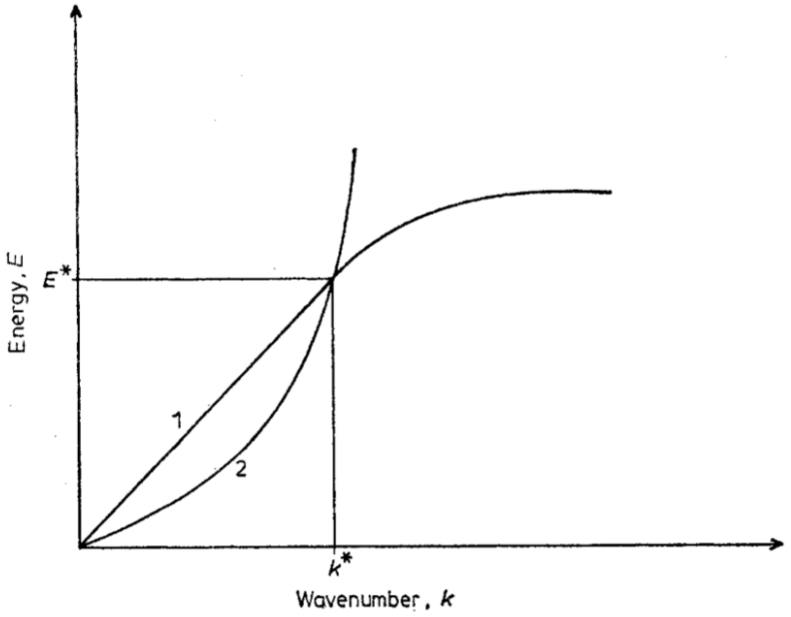


**Figure 1.3.:** The energy and momentum conservation in coherent scattering of UCN from single phonon scattering where 1 indicates the phonon dispersion curve of $^4$He and 2 the curve of a free neutron with energy $E = \frac{\hbar^2 k^2}{2m}$ taken from [9]

## 1.3. Purpose of this Thesis

As emphasized above, current UCN experiments rely on high UCN densities. For thermal sources the UCN the intensity of the beam is limited by applying Liouville's theorem on the neutron system. Contrary, superthermal sources, which are up to now run in fill and empty mode to achieve the highest density, are mostly limited by storage behavior of the converter and storage properties. These are given by the converter media, its geometry and wall materials, as well as the extraction mechanism of the accumulated UCN. Therefore, methods and components are investigated to improve the performance of storage vessels in superthermal sources, as well as UCN handling systems are to deliver higher UCN densities at experiments.
The easiest accessible approach to increase the UCN number density $\rho$ inside the converter vessel of the source is to increase its storage time, which enters linearly:

$$\rho_{\mathrm{UCN}} = \tau_{\mathrm{eff}} \cdot P \tag{1.2}$$

Where the production rate $P$ is limited by the UCN conversion efficiency, the delivered CN neutron flux at the converter and the effective neutron lifetime $\tau_{\mathrm{eff}}$ is derived by

$$\tau_{\mathrm{eff}}^{-1} = \tau_{\mathrm{life}}^{-1} + \tau_{\mathrm{med}}^{-1} + \tau_{\mathrm{loss}}^{-1} \tag{1.3}$$

including the neutron life time $\tau_{\mathrm{life}}$, converter media specific properties $\tau_{\mathrm{med}}$ and additional losses $\tau_{\mathrm{loss}}$ due to the geometry of the bottle, absorption or inelastic scattering in the wall material, and any remaining slits and gaps between the components and sealing mechanism. Since for most wall materials the calculated and measured effective lifetime differ by one to two orders of magnitude, likely due to chemically bound hydrogen on the surface, up to now a hydrogen repelling fluoropolymer vacuum grease called Fomblin is commonly used as wall coating [10, 11].This leads to higher effective lifetimes, despite the comparatively low optical potential 110 neV, implying low loss parameters of $1 \times 10^{-5}$ at room temperature. However, the remaining discrepancy between $1 \times 10^{-5}$ to the theoretical value $10^{-7}$ may be caused by inelastic scattering due to its liquid phase at room temperature. Attempts to use it in solid phase, by freezing at cryogenic temperature are made difficulty due to cracking and crumbling of the thin layer, which also makes its use at superthermal sources challenging.
This situation motivates first tests of the amorphous carbon fluoride molecule CYTOP [12], which should posses similar neutron optical properties to Fomblin while avoiding some of its disadvantages. It can be reliably coated by a dip-coating process on any metal or glass surface and after baking transitions to a glassy phase. Moreover, due to its thermal expansion and elasticity coefficient, it should stick at walls without defects even at cryogenic temperatures.
In order to conduct the first storage time measurements for a storage bottle coated with CYTOP, a new set up for the evaluation of UCN storage bottles at ambient and cryogenic temperatures is developed. A first test is conducted measuring the storage time with CYTOP at ambient temperature for a confinement similar to the converter vessel volume of the superthermal source SUN II at the ILL. This provides a practical means of convenient testing its performance in an environment where it could be used later on.
To further optimize the UCN densities ar experiments, a complete stainless steel handling system with an inner guide width of ⌀50 mm is built and evaluated by measuring its transmission using time of flight (TOF) spectra. The guide width is defined by the relative volume of the converter vessel to the guide system, since reducing the diameter would also reduce the neutron free path, leading to higher losses.
Since, the spectra of certain superthermal sources are shifted to lower velocities compared to the spectra delivered by the thermal source at the PF2 TES beam line, the velocities are shifted down by lifting the measurement set-up. This exploits the neutrons interaction

with gravity, and a method using the TOF set-up in vertical alignment is presented to obtain information from the neutrons with energies below the optical potential of the Al foil at the entrance of the detector. Additionally, with this set-up the transmission for glass guides coated with non-depolarizing copper (Cu) and nickel-molybdenum alloy (NiMo) are measured.
In order to empty and fill the storage bottle through a single aperture, a three way rotary switch is designed and its transmission is defined for a velocity range from 0 to 20 $\frac{\mathrm{m}}{\mathrm{s}}$ using TOF in horizontal and vertical configurations. The relative detection efficiency of the boron-10 based cascade detector used for TOF and a $^3$He detector regularly used at PF2 is also evaluated. This is of significant interest for experiments where both detectors are used simultaneously or where the absolute efficiency of either one may be experimentally important.

# 2. UCN Physics

To guide and store UCN the interacting wall materials must fulfill some physical requirements otherwise the neutrons could simply pass through, be scattered out of the ultra cold regime or be absorbed within the wall. A brief theoretical description of UCN physics and storage properties is presented in the following sections based on the UCN standard reference texts by Goloub [13] and Ingatovich [14].

## 2.1. UCN Properties and Interactions

The neutron is a baryon consisting of one up and two down quarks with an overall mass $m_\mathrm{n} = 1.675 \times 10^{-27}\,\mathrm{kg}$. The energy of UCNs is by definition below 300 neV. According to the particle-wave duality the neutron energy can be expressed either in terms of velocity $v_\mathrm{n}$ or de Broglie wavelength $\lambda_\mathrm{n}$:

$$E_\mathrm{n} = \frac{1}{2} m_\mathtt{n} v^2 = \frac{h^2}{2 m_\mathtt{n} \lambda_\mathtt{n}^2} \tag{2.1}$$

Where $h$ is the Planck constant. The maximum UCN energy $E_\mathtt{n} < 300\,\mathrm{neV}$ is used to obtain characteristic values for $v_\mathrm{n}$ and $\lambda_\mathrm{n}$:

$$\lambda_\mathtt{n} > 52\,\mathrm{nm} \tag{2.2}$$

$$v_\mathtt{n} < 7.6\,\frac{\mathrm{m}}{\mathrm{s}} \tag{2.3}$$

Those properties enable to trace and manipulate the UCN trajectory, as free neutrons undergo all fundamental interactions, except the Coulomb interaction due to its neutrality.

### 2.1.1. Weak Interaction

Due to weak interaction free neutrons are not stable and decay with a mean lifetime $\tau_\beta = (879.5 \pm 0.8)\,\mathrm{s}$ [5]. The so called neutron $\beta^-$-decay reaction is the following:

$$n \longrightarrow p + e^- + \overline{\nu}_e + 782\,\mathrm{keV} \tag{2.4}$$

The fundamental reaction inside in the neutron is represented by the Feynman diagram 2.1. While a down-quark changes its favor to an up-quark - meaning the nuclei becoming proton - a W-Boson is exchanged which decays into an electron and anti electron neutrino $\overline{\nu}_e$.

### 2.1.2. Magnetic Interaction

The neutron is a fermion with spin $\frac{1}{2}$ that possesses a negative magnetic dipole moment $\mu_\mathrm{n} = \gamma \vec{S}$ anti parallel to its spin due to the structure of the charged quarks. Whereas $\gamma = (-183.25\,\mathrm{MHz})/T$ is the gyromagnetic ratio.Thus, if a neutron is exposed to a spatially in-homogeneous magnetic field $B$ force is applied.

$$\overrightarrow{F} = |\overrightarrow{\mu}_n| \nabla |\overrightarrow{B}| \tag{2.5}$$

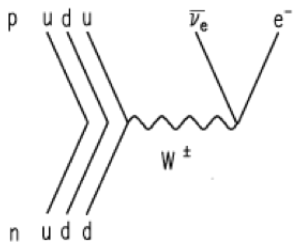


**Figure 2.1.:** Feynman diagram of the neutron $\beta^-$-decay. A down quark transforms to an up quark emitting a W-boson that decays to an electron and $\nu_e^-$ [15]

This means, whether the spin is parallel or decelerated if anti parallel to the magnetic field. For the magnetic potential in an external magnetic field can be described by:

$$\Delta V_{\mathrm{M}} = (2\vec{\mu}_{\mathrm{n}}\vec{B} \approx \pm 60\,\mathrm{neV/T}) \cdot B \tag{2.6}$$

Accordingly one of the two spin states can be either selected or completely dismissed, meaning the transmitted neutrons are selected for the chosen spin state. Polarized neutrons can be studied in experiments with high magnetic fields are applied and can also be stored easily with a magnetic trap.

### 2.1.3. Gravitational Interaction

Gravity is negligible for experiments with faster neutrons, as their kinetic energy far exceeds the potential energy in the Earth's Gravitational field. On the contrary, the kinetic energy of UCN is at the same order of magnitude and therefore the motion of UCNs is strongly affected by the gravity.

$$\Delta V_{\mathrm{G}}/\Delta h = m_{\mathrm{n}} g = 102 \times 10^{-9}\,\frac{\mathrm{eV}}{\mathrm{m}} \tag{2.7}$$

Where $g$ is the gravitational acceleration on earth and $\Delta h$ the height difference from the initial to the final position of a neutron. By in- or decreasing the height of an experiment, within handy dimensions, one can influence the velocity spectra of UCNs provided by the sources. Therefore, this is a commonly used tool for adapting the UCN velocity spectra when this is required for experiments. It is also used to overcome the potential barrier of vacuum separation foils to enter UCN detectors or pass material windows in a guide.

### 2.1.4. Strong Interaction

Nucleons are bound by the strong interaction inside a nucleus, which can be represented at low energies as a spherical square-well potential with a depth of 50 MeV (see fig. 2.2).
Due to the electirc neutrality of neutrons, strong interaction is the main force during collisions with nucleus, whereas the neutrons can either be scattered elastic and inelastic or can be absorbed inside the nucleus. However, the effective interaction due to the strong force between the surface atoms of a wall material and neutrons allows to manipulate their trajectory and even to store UCN. A neutron does 'see' a averaged potential of many surface atoms which is described in detail in the following section.

## 2.2. Scattering of UCN on surfaces

As in equation (2.2) the wavelengths of UCN are greater than 50 nm which is already for the fastest neutrons more than a factor 100 above the lattice parameter in most solids. Thus neutrons see an averaged potential according to the atomic composition of the wall material, the so called neutron optical potential $V_{\mathrm{f}}$. For ideal loss-less surfaces containing

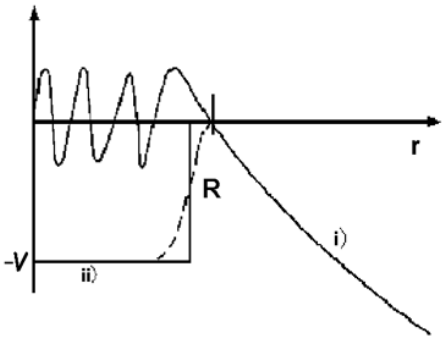


**Figure 2.2.:** Square well approximation of the neutron-nucleus interaction. Depicted are the i) neutron wavefunction inside a nucleus with radius $R$ and the ii) Potential with a depth $V$ for a positive scattering length. The dashed line shows the more accurate Fermi potential [13].

of $K$ different atomic species with different scattering length $a_\mathrm{k}$ and number densities $n_\mathrm{k}$ the potential is given by:

$$V_\mathrm{f} = \frac{2\pi\hbar^2}{m_\mathrm{n}} \sum_{k=1}^{K} a_\mathrm{k} n_\mathrm{k} \tag{2.8}$$

In the classical picture this means that the potential step is higher than the kinetic energy of the neutrons $E_\mathrm{n} \leq V_\mathrm{f}$ they are totally reflected under any angle of incidence and one can easily derive the critical maximum neutron velocity for that wall material.

$$v_\mathrm{c} = \sqrt{V_\mathrm{f}/2m_\mathrm{n}} \tag{2.9}$$

This is an important figure of merit for experiments in order to later on manipulate the neutron velocity spectra provided by an UCN source by adapting the height according to equation (2.7). Whereas, the source and changed spectra can be measured with a time of flight set up, providing an one dimensional energy information of the neutrons. In table 2.1 an overview of the optical potential of commonly used materials is provided.

**Table 2.1.:** Calculated optical potentials for materials commonly used at UCN experiments

| Material | Abbreviation | optical potential $V_\mathrm{f}$ in neV |
|---|---|---|
| aluminum (alloys) | Al (AlMg3) | 54 |
| amorphous fluoropolymer (sec. 4.2) | CYTOP [16] | 117 |
| liquid fluoropolymer | Fomblin | 110 |
| beryllium oxide | BeO | 257 |
| copper | Cu | 168 |
| deuterated polyethylene | dPE | 210 |
| diamond like carbon [17] | DLC | 250 |
| Nickel molybdenum alloy | NiMo | 220 |
| stainless steel | inox | 190 |
| titanium | Ti | -48 |

### 2.2.1. Ideal loss-less surfaces

By use of the optical potential (2.8) the quantum treatment can be simplified to an one dimensional problem. The neutron wave with energy $E_\mathrm{n} = \frac{\hbar^2 k^2}{2m_\mathrm{n}}$ propagating from the

left to the right side hits the potential step at the origin $x = 0$ and is both reflected and transmitted, as depicted in figure 2.3. This leads to the state functions $\Psi_{\mathrm{I}}$ for the incident and reflected wave (left side) and $\Psi_{\mathrm{II}}$ for the transmitted wave (right side).

$$\Psi_{\mathrm{I}} = e^{ikx} + Re^{-ikx} \tag{2.10}$$

$$\Psi_{\mathrm{II}} = Te^{ik'x} \tag{2.11}$$

where $R$ and $T$ are the amplitude of the reflected and transmitted waves, respectively. With the boundary conditions $\Psi_{\mathrm{I}}(0) = \Psi_{\mathrm{II}}(0)$ and $\partial_x\Psi_{\mathrm{I}}(0) = \partial_x\Psi_{\mathrm{II}}(0)$ the reflection probability can be calculated.

$$|R|^2 = \frac{k - k'}{k + k'} = \frac{E^{1/2} - (E - V)^{1/2}}{E^{1/2} + (E - V)^{1/2}} \tag{2.12}$$

For neutrons with $E_{\mathrm{n}} < V_{\mathrm{f}}$, $k'$ is imaginary and thus the reflection probability $|R|^2 = 1$ providing the same result as in the classical picture. Whereas one has to keep in mind that the transmitted amplitude $T \neq 0$ and thus the wave is penetrating to some extend into the wall material. Therefore, interactions with the bulk atoms take place leading to an UCN los, which is described by an imaginary part.

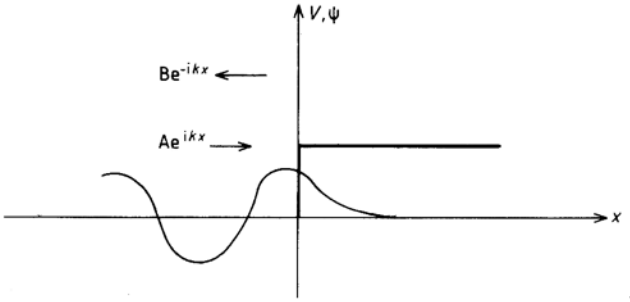


**Figure 2.3.:** The incoming wave with an energy $E_{\mathrm{n}} < V_{\mathrm{f}}$ is totally reflected from the potential step, but still has a finite penetration into the wall material [13]

### 2.2.2. Loss probability coefficient

The UCNs which penetrate into the wall material interact with the atoms of the wall, where the main interactions are:

- **Absorption** A neutron makes a transition to a bound state in the deep potential of a nucleus (see fig. 2.2) under emission of a $\gamma$-ray.
- **Inelastic up-scattering:** Hence the atoms of the material are at an initial energy at temperature $T$, this energy can be transmitted to a reflected neutron with an initial momentum $\hbar k_{\mathrm{i}}$ leading to a final state $\hbar k_{\mathrm{f}}$ with $E_{\mathrm{n}} > V_{\mathrm{f}}$ which is no longer store able. The reverse transition is usually negligible due to the possible number density of states.

Both loss channels can be represented by a material-specific scattering loss cross-section $\sigma^{\mathrm{l}}$ giving an imaginary potential.

$$W = \frac{\hbar}{2} \sum_{k=1}^{K} n_{\mathrm{k}} \sigma_{\mathrm{k}}^{l} v_{\mathrm{n}} \tag{2.13}$$

The loss scattering cross section is added to the elastic scattering cross-section obtaining the total scattering cross section $\sigma^{\mathrm{tot}} = \sigma^{\mathrm{real}} + \sigma^{\mathrm{im}}$ and together with the correlation $a_{\mathrm{k}}$ equation (2.8) can be rewritten.

$$U = V - iW = \frac{2\pi\hbar^2}{m_\mathrm{n}} \sum_{k=1}^{K} \left(a^\mathrm{real} - ia^\mathrm{im}\right)_\mathrm{k} n_\mathrm{k} \tag{2.14}$$

For a specific material the loss coefficient per wall collision $\eta$ is defined by dividing the loss potential in given in equation (2.13) by the optical potential equation (2.8) providing a figure of merit for UCN guiding and storing.

$$\eta = \frac{W}{V} = \frac{\sigma m k}{4\pi a} \tag{2.15}$$

Because $\sigma \propto \frac{1}{v}$ $\eta$ is velocity independent and is for commonly appropriate for UCN guiding and storage materials at about $10^{-4}$.
To calculate the losses during storage and guiding the loss probability $\mu$ is needed, which is obtained by using equation (2.12) for the amplitude of a reflected wave and the relation $\eta = W/V \ll 1$. Taking the average over all angles of incidence, as the movement of neutrons stored in a box can be seen as isotropic after a few bounces, one obtains the energy-dependent loss probability for planar surfaces.

$$\bar{\mu}(E) = 2\eta \left[ \frac{V_\mathrm{f}}{E_\mathrm{n}} \sin^{-1}\left(\frac{E_\mathrm{n}}{V_\mathrm{f}}\right)^{1/2} - \left(\frac{V_\mathrm{f}}{E_\mathrm{n}} - 1\right)^{1/2} \right] \tag{2.16}$$

#### 2.2.2.1. Losses due to Surface Roughness

The considered loss probability up to now is still limited to perfectly planar surfaces. In real experiments such a surface is not achievable and some roughness remains, causing two main effects:

- **Non-specular reflection:** Surface roughness strongly influences an initial directed neutron flux, as the neutrons are reflected at different angles, leading to more and more non-specular behavior with increasing roughness . This needs to be limited in order to guide neutrons with energies above the guide material optical potential. If they propagate at larger angle than the critical refection angle they are not reflected any more. Also more bounces are needed to pass a given guide length, leading to higher losses for a constant loss probability per bounce. Contrary to guide systems this is favorable for neutron storage bottles, since equation (2.16) is only valid under this condition.
- **Increasing UCN loss probability:** The loss probability itself is affected in two different ways. On the one hand, waviness, where the surface roughness correlation length is far above the neutron wavelength, simply increases the surface area (see (2.25)) and on the other hand, micro roughness, for surface roughness correlation lengths far below the neutron wavelength $\lambda_\mathrm{n}$, smoothing out of the potential step and therefore causing additional losses due to influence on the reflection probability and preparation depth/time.

#### 2.2.2.2. Micro Roughness Model

The micro roughness model introduced by Steyerl [18] provides an expansion of the loss probability per bounce by including the surface roughness for correlation length $w \ll \lambda_\mathrm{n}$ using the exponential ansatz for the autocorrelation function of rough surfaces [13, 18].

$$|f(\vartheta)|^2 = 2\pi\tilde{b}\rho^2 b_\mathrm{coh}^2 w^2 e^{w^2 q^2/2} \tag{2.17}$$

Where $b_{\mathrm{coh}}$ is the coherent scattering length in barns, $\rho$ the number density of the atoms inside the material and $q$ the momentum transfer parallel to the surface. The material roughness is defined by the correlation length $w$ and the mean square amplitude $\tilde{b}^2$, which can be measured independently by surface roughness measurements. Further application of perturbation theory and Green's functions for the surface provide a statement about the probability distribution for non specular reflection, described in detail in [13]. The result indicates that for good guiding behavior a low surface correlation $w$ is needed.
This ansatz provides also an additional surface roughness loss channel. Including the surface-specific properties mean square amplitude $\tilde{b}^2$ and correlation length $w$, for the loss rate probability we have:

$$\mu = \mu_{\mathrm{eff}} \left( 1 + \frac{2\tilde{b}^2 k_{\mathrm{c}}^2}{1 + 0.85 k_{\mathrm{c}} w + 2 k_{\mathrm{c}}^2 w^2} \right)^{1/2} \tag{2.18}$$

Where$k_{\mathrm{c}}$ is the critical wave number for total reflection on the material optical potential. To give an order of magnitude for the size of this effect, a worst case approximation for $w \to 0$ and common material properties is done in [13], revealing an increased loss of 25 %.

#### 2.2.2.3. Transmission Loss Due to Surface Roughness

The scattering cross section's dependence on the surface roughness can be calculated by using the exponential ansatz (2.17), together with the perturbation ansatz used in [18].

$$\sigma = \int_{q=0}^{q=2k} |f(\vartheta)|^2 d\Omega = \frac{\tilde{b}^2 S}{4} \frac{k_{\mathrm{c}}^4}{k_{\mathrm{i}}^2} \tag{2.19}$$

Where $S$ is the planar surface area and $k_{\mathrm{i}}$ the wave number of the incident neutron. Division by $S$ finally gives the 'loss' due to surface roughness.

$$L_{\mathrm{loss}} = \frac{\sigma}{S} = \frac{\tilde{b}}{4} \frac{k_{\mathrm{c}}^4}{k_{\mathrm{i}}^2} \tag{2.20}$$

Since $\tilde{b}$ still remains in this equation, the surface roughness dependence of the neutron velocity includes an additional $1/k_{\mathrm{i}}^2$ factor, which means that slow neutrons should be less efficiently transmitted than fast neutrons for any rough surface.

## 2.3. Guiding UCNs

To give standardized statements about the guide quality in [13] and [14] theoretical models are developed describing the transmission of neutrons through guide systems. In the following, the transmission $T$ of a UCN guiding system is determined by measuring the neutron flux before and after the to be examined assembly [14].

$$T = \frac{N_{\mathrm{sample}}}{N_{\mathrm{ref}}} \tag{2.21}$$

Where $N_{\mathrm{ref}}$ is the count rate before and $N_{\mathrm{sample}}$ after the investigated assembly. For a straight guide assembly without additional losses the transmission should follow an exponential decay in length and therefore is given by:

$$T = T_{\mathrm{norm}}^{l/\mathrm{m}} \tag{2.22}$$

However, for a real experiment other loss channels such as surface contamination, misalignment and gaps between the guide elements occur. Also the initial preparation of the guiding surfaces, including coating and polishing method, influence roughness and waviness which both lead to reduced performance. In figure 2.4 the theoretical transmission for different $T_{\mathrm{norm}}$ illustrates the importance of a high UCN transmission, since for an transmission efficiency of 90 % per meter at a guide length of 2 m already 1/3 of the initial intensity is lost.

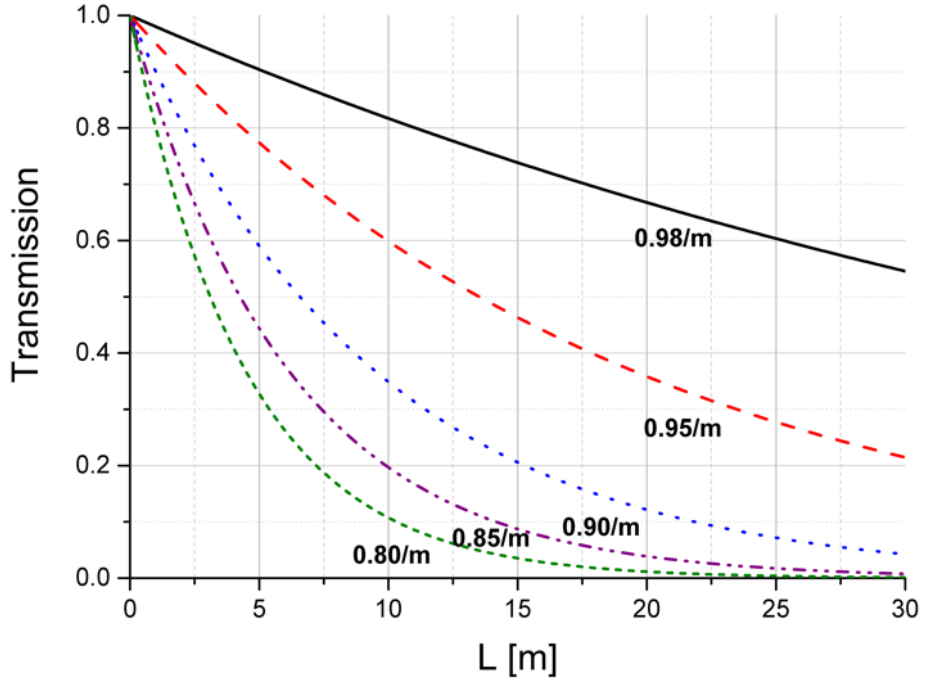


**Figure 2.4.:** Calculated transmission as a function of guide length, taken from [19].

## 2.4. UCN Storage

### 2.4.1. Theoretical approach

The most important property of UCN is that they are totally reflected under any angle of incidence, therefore they can be stored in any confinement. For perfect loss less materials the storage time is ultimately limited by the neutron lifetime $\tau_\beta = (879.5 \pm 0.8)\,\mathrm{s}$ [20]. For real devices gaps between the assembled bottle components almost inevitably lead to a significant loss channel $\tau_{\mathrm{gap}}$. Additional losses due to inelastic wall collisions further reduce the effective storage time by $\tau_{\mathrm{wall}}$:

$$\frac{1}{\tau_{\mathrm{eff}}} = \frac{1}{\tau_{\mathrm{gap}}} + \frac{1}{\tau_{\mathrm{wall}}} + \frac{1}{\tau_\beta} \tag{2.23}$$

Now $\tau_{\mathrm{wall}}$ strongly depends on the geometry of the storage vessel which is given by:

$$\tau_{\mathrm{wall}} = \bar{l} \cdot \frac{1}{v_{\mathrm{n}} \mu_{\mathrm{eff}}} \tag{2.24}$$

$v_{\mathrm{n}}$ is the neutron velocity, $\mu_{\mathrm{eff}}$ the in equation (2.18) obtained over all angles of incidence averaged material specific loss probability and $\bar{l}$ the mean free path between two wall collisions, determined by the fraction of the storage volume $V$ to its inner wall surface $S$. For a cylindrical storage confinement in horizontal alignment with a radius $R$ and length $L$ as for example used in this thesis and neglecting gravitational interaction this holds:

$$\bar{l} = \frac{4V}{S} \overset{\text{Cyl.}}{=} \frac{2LR}{(R+L)} \tag{2.25}$$

This means by decreasing the vessel volume, $\bar{l}$ decreases proportionally and thus more wall interaction take place in the same time scale. Therefore, according to equation (2.24) the

wall loss time $\tau_{\text{wall}}$ decreases as well. On the other hand, for an infinite volume $\tau_{\text{wall}}$ is limited by gravity, to $2v/g$. This shows that the geometrical storage time strongly depends on the incoming neutron spectra. It should be measured in advance to enable a proper analysis of the storage experiment.

### 2.4.2. Storage Time Experiments

The combined geometrical, gap and wall losses can be determined by measuring storage curves and estimating the mean loss probability per bounce $\overline{\mu}$. The storage curve is obtained by repeating several measurements with different storage times, where each measurement counts the remaining neutrons at the end. First, the storage bottle is filled to the maximum achievable neutron density and then closed. After a certain storage time the bottle is opened again and neutrons are detected. Plotting the integrated neutron counts against storage time, a exponential dependence is typically observed.

$$N\left(t_{\text{exp}}\right) = N(0) \exp\left(-\frac{t_{\text{exp}}}{\tau_{\text{eff}}}\right) \tag{2.26}$$

Here $N(0)$ is the number of accumulated ultra cold neutrons after closing the bottle and $\tau_{\text{eff}}$ is the effective storage time.
Plotting the counts arriving at the detector as a function of time should in turn reveal a exponential dependence. Since the loss time constant $\tau_{\text{wall}}$ depends on the neutron angular distribution and the neutron velocity $v_{\text{n}}$, the theoretical and the measured storage curve could differ from each other. Thus, in many cases that the experimental data can not be described by only one exponential decay and therefore a double exponential decay is used fitting the data describing the storage behavior of fast and slow neutrons.

### 2.4.3. Excess UCN Losses

First storage time measurements with neutrons trapped inside non magnetic material walls with high neutron optical potentials, such as Be and diamond like carbon (DLC), revealed an effective lifetime one to two orders of magnitude lower than expected from theory [21,22]. This cannot be explained by including losses due to surface roughness or gaps. Due to large differences between theory and measurements a neutron-absorbing contaminant on the surface can seems unlikely because the amount would need to be quite large.
A contamination layer consisting of chemically bound hydrogen is a more likely cause for the excess losses, since it efficiently up-scatters the UCN. The amount of hydrogen on real surface could be large enough to explain this excess loss. First experiments to remedy this losses by baking the storage volumes under vacuum and afterwards cooling them, as well as a deuterium treatment revealed promising results. Additionally, tests with hydrogen repelling surfaces, such as Fomblin, could help to close the gap between theory and experimental results [22].

# 3. Neutron Handling System

In this chapter details of the neutron handling components that are used for storage time measurements in chapter 4 are presented and characterized (sec. 3.1, 3.3, and 3.5).Methods and models are investigated to increase and analyze the neutron density delivered and detected at UCN experiments. A vertical TOF measurement is introduced and tested to determine the transmission for coated glass guides of neutrons with energies below the optical potential of the separation foil at the detector entrance (sec. 3.4). The dependent transmission of UCNs through aluminum separation foils is measured (sec. 3.2) for different surface roughness.

## 3.1. Time of Flight Measurements

The time of flight (TOF) technique is a general method to determine the velocity of detected neutrons, by measuring the transit time it between two fixed, where the distance is known, as depicted in figure 3.1. The start time is determined, in the ideal case, by a finite short delta peaked opening time of a chopper system, to avoid uncertainties in the measured time of flight and the end time is defined by the detection of the neutrons at the detector. Using the time of flight for each neutron its velocity can be calculated, as explained in the following sections. Summing up the counts in time or velocity bins and plotting them provides a typical spectral distribution of the neutrons. Whereas, this is only a one dimensional projection of the three dimensional movement of the neutrons. With this information the velocity dependent transmission of an examined sample can be calculated by normalizing the measured spectra after the sample to the measured spectra before.

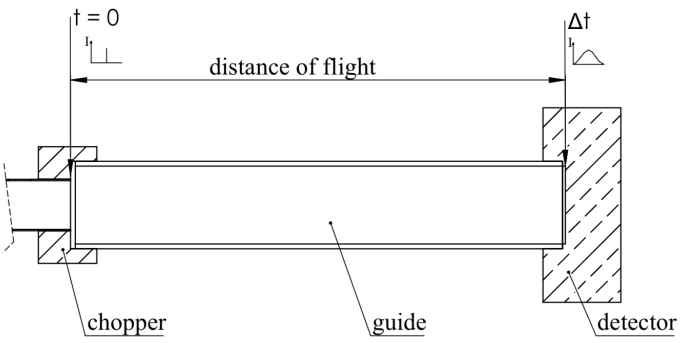


**Figure 3.1.:** Diagram of a horizontal time of flight (TOF) set-up used in this thesis, where the neutrons propagate from left to right. The chopper defines the start of the time measurement by a short opening pulse $t = 0$. The neutrons travel along the distance of flight and are detected after the corresponding time $\Delta t$ at the detector, leading to a broadened spectrum due to the velocity differences of the neutrons.

The velocity dependent neutron count rate and thus the transmission for each investigated part or assembly of the neutron handling system are measured with a TOF set-up consisting of a commercial chopper from Movatec [23] connected to a ∅90 mm×500 mm glass guide coated with $TiB_2$ and a commercial boron based detector (cascade 2D-200, CDT GmbH) [24]. Where the counted neutrons are binned in time bins with a width of 0.5 ms. The settings of the time of flight are listed in table 3.3. Since the detector system provides a 1D projection,

**Table 3.1.:** Time of flight measurement settings.

| | | |
|---|---|---|
| distance of flight | $l$ | 508 mm |
| opening time | $t_{\text{open}}$ | 17.4 ms |
| offset | $t_{\text{off}}$ | 20.25 ms |
| pulse frequency | $\nu$ | 2.5 Hz |

the velocity component along the guide axis of the three dimensional neutron velocity vector, a $TiB_2$ coated guide is chosen due to its low optical potential and high absorption cross-section. This suppresses neutrons with large velocity components in the perpendicular and inverse directions. Hence, they are bouncing more often and at a wider incident angle at the guide walls before entering the detector, thus are more likely absorbed.
The chopper opening function depicted in figure 3.2 resembles more two overlapping Gaussian due to the inertia of the moving parts. Since convolution of the initial spectra with the opening function conducted in [25] and [26], this is approximated with an rectangular opening function with opening time $t_{\text{open}}$. The time is set to leverage the full chopper opening while keeping the time window as short as possible avoiding significant influence of the chopper opening function on the investigated spectra. Since the chopper is not completely leak tight for neutrons, the frequency $\nu$ is chosen to obtain a proper constant background of the leaking chopper, not influenced by the tail of the TOF spectra anymore, as well as to avoid frame overlap. The measurement time is set to 180 s, which means that a full measured set with pulse frequency of $\nu = 2.5$ Hz consists of roughly 475 *sweeps* differing at about ±3 *sweeps* per measurement due to dead times in the chopper electronics.

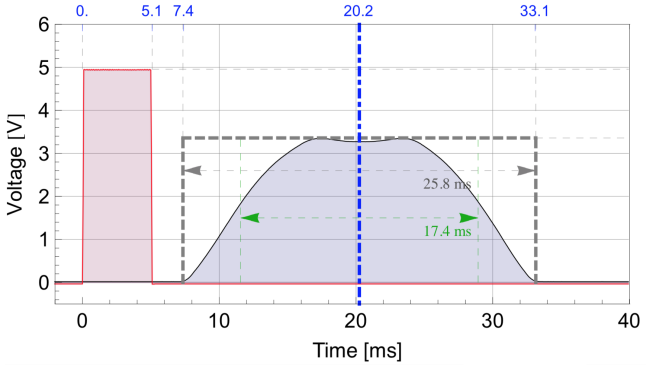


**Figure 3.2.:** Diagram of the chopper opening function measured with light conducted in [25]. The opening function can be replaced by a perfect chopper with rectangular opening function, which has the same integral light intensity coming through. The chopper offset $t_{\text{off}}$ arises from the detector trigger on the rising slope of the signal.

### 3.1.1. Horizontal Set-Up

To convert the time of flight spectra, measured in the horizontal plane (see fig. 3.8), to velocity dependence the correlation is given by:

$$v(t) = \frac{l}{t} \tag{3.1}$$

Where $l$ is the time of flight distance. This distance is 508 mm for all experiments in this thesis, including some offsets from the chopper closing aperture and distance between the installed guide to the aluminum separation foil of the detector. One should note, if the set-up is not properly leveled perpendicular to the Earth's gravitational field an additional term adds to equation (3.1) complicating the interpretation of the TOF spectra.
The count rate in time $f_\mathrm{t}$ is calculated by dividing the measured counts $c$ per bin by the overall opened time per measurement $t_\mathrm{meas} = sweeps \cdot t_\mathrm{open}$. Transforming the rate in time $f_\mathrm{t}$ to the velocity dependent count rate $f_\mathrm{v}$ additional differentiation is needed.

$$f_{\mathrm{v}_i} = f_{\mathrm{t}_i} \left| \frac{\partial t_i}{\partial v_i} \right| \cdot \frac{1}{Norm} \tag{3.2}$$

The differentiation is given by $\frac{\partial t}{\partial v} = \frac{t^2}{l}$ obtained by solving equation (3.1) for $t$ and differentiation in $v$ and the final statement is given by replacing $v$ with the correlation in equation (3.1). The normalization $Norm = \sum c_{i(\mathrm{v})} / \sum c_{i(\mathrm{t})}$ is applied to recorrect the total number of counted neutrons in the time regime.
The errors are assumed as Poisson distributed and are given for count statistics as the square root of the number of counts $\sigma = \sqrt{c}$. For further mathematical treatment of the data the Gaussian error propagation is applied. Hence, the precision per run differs a simple averaging cannot be done which means each average for a measured series has to be calculated by weighting each data point with the inverse square of its own error.

$$\langle c \rangle = \frac{\sum_{i=1}^{N} \frac{1}{\sigma_{c_i}^2} c_i}{\sum_{i=1}^{N} \frac{1}{\sigma_{c_i}^2}} \tag{3.3}$$

The resulting error for each measurement is then given by:

$$\frac{1}{\sigma_{\langle c \rangle}^2} = \sum_{i=1}^{N} \frac{1}{\sigma_{c_i}^2} \tag{3.4}$$

It has taken into account that the errors up to now only consider statistical error. Any systematically errors by systematical effects of the experiment, such as occurring gaps and misalignment, or of the UCN is added linearly added $\sigma_\mathrm{sum} = \sigma_\mathrm{stat} + \sigma_\mathrm{syst}$ giving a more conservative statement and are explained in detail for each case when they are applied.

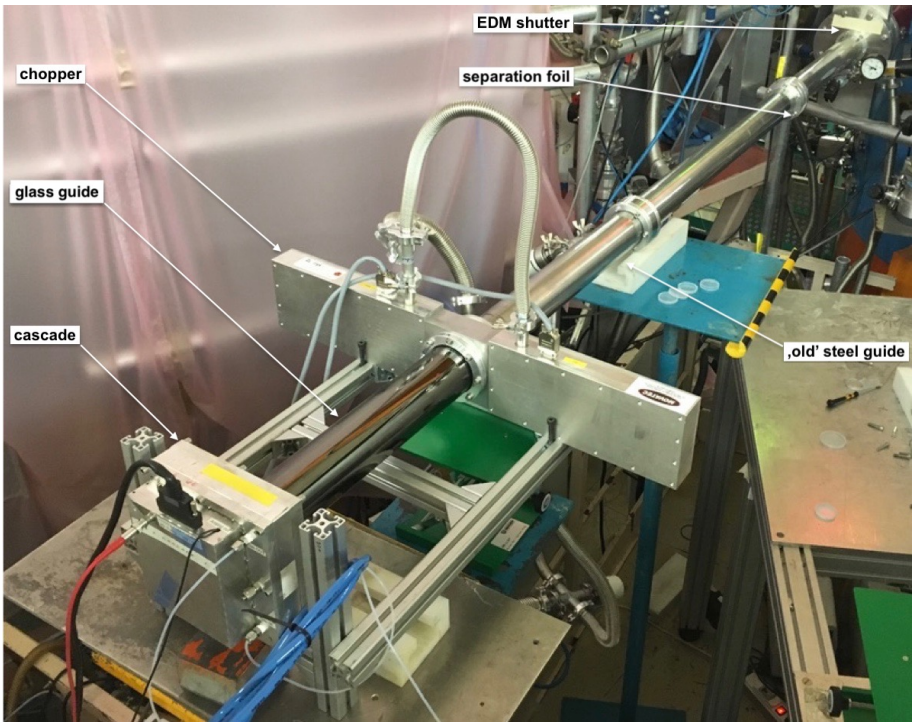


**Figure 3.3.:** Picture of the time of flight set up attached to the EDM beam line measuring the initial spectra delivered by the Turbine 1.6 m after the separation foil.

### 3.1.2. vertical set-up

Operating the TOF set-up perpendicular to the horizontal plane special treatment is needed, hence the earth gravitational force $g$ acts along the TOF path. This adds a second term to the velocity on time dependent equation (3.1) by accelerating the neutron within the TOF distance.

$$v(t) = \frac{l}{t} \pm \frac{1}{2}gt \tag{3.5}$$

Hence, the spectra is recalculated to the time where the chopper was opened and therefore to its height the sign depends whether if the chopper is below the detector (+) or above **(-)** as **in our case** (see fig. 3.4). In order to calculate the differentiation $\frac{\partial t_i}{\partial v_i}$ the above introduced equation is solved for $t$ by multiplying with $t$ and then set to zero, to apply the quadratic formula.

$$t_\pm = \frac{-v \pm \sqrt{v^2 + 2gl}}{g} \tag{3.6}$$

The negative solution for the time in equation (3.6) can be neglected as negative solutions in time are physically not possible. Equation (3.6) is differentiated in $v$ and $v$ is replaced according to equation (3.5) with $t$ giving the full differentiation.

$$\left|\frac{\partial t_i}{\partial v_i}\right| = \frac{1}{g}\left(-1 + \frac{l/t_i + gt/2}{\sqrt{(l/t_i + gt/2))^2 + 2gl}}\right) \tag{3.7}$$

To calculate the spectra arriving at the chopper, further data processing is similarly done as described in the previous section from equation (3.2) onward. Whereas, the influence of the 90° bow between the experiment and the TOF set-up on the 3D neutron velocity spectra has to be considered. Additionally, one should keep in mind that the neutron already dropped down a short path due to the bend and guide $l_{\mathrm{drop}} = 210\,\mathrm{mm}$ and therefore, the spectra is already shifted by $v = \sqrt{2gl_{\mathrm{drop}}} = 2\,\frac{\mathrm{m}}{\mathrm{s}}$. For visualization of the vertical TOF a picture of a raised measurement conducted at the PF2 TES beam line is given in figure 3.1.2.

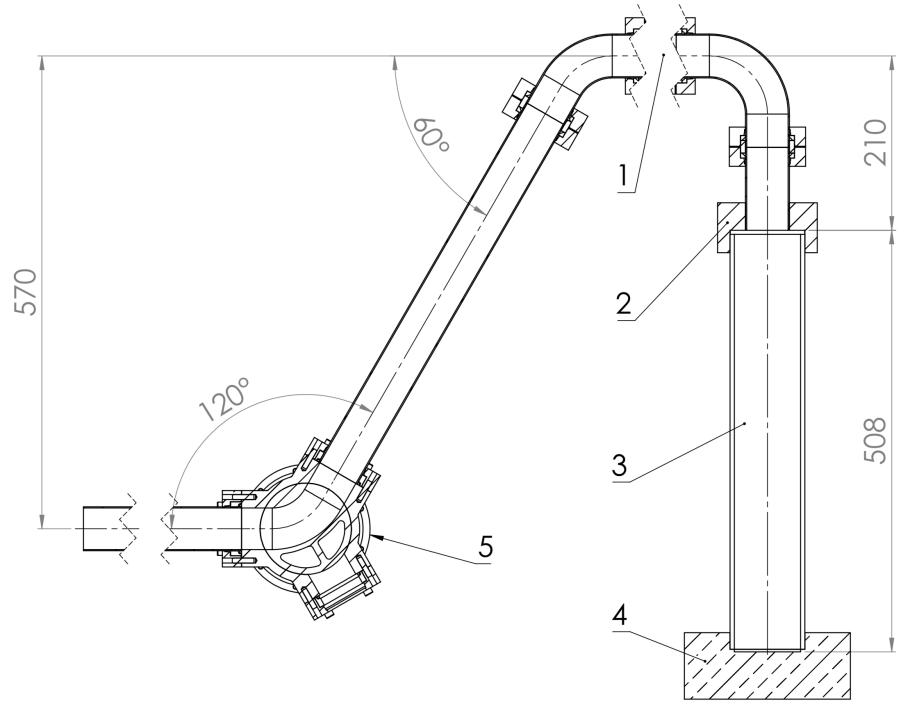


**Figure 3.4.:** Draft of the vertical TOF set-up used for the characterization and storage time measurements (dimensions in mm). The brackets indicate the lifted experiment (1) before the 90° bow with a short guide section attached to the TOF set-up. Consisting of a chopper (2), a vertical aligned $TiB_2$ coated glass guide (3) and a cascade detector (4).

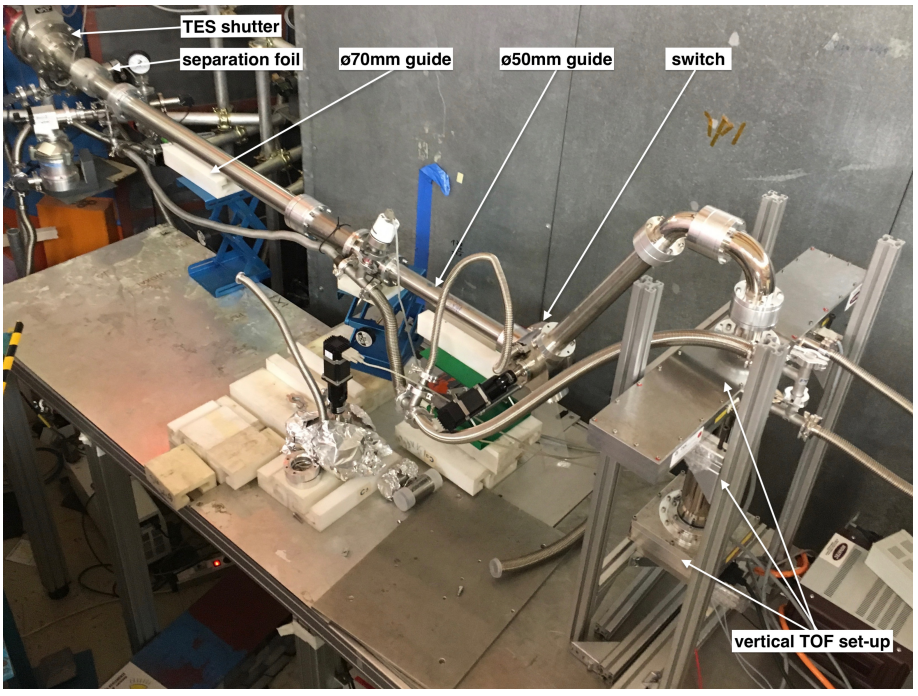


**Figure 3.5.:** Picture of the vertical TOF set-up measuring the initial flux before the lifted switch transmission measurements.

## 3.2. Surface Roughness Influence on UCN Transmission

An aluminum separation foil is installed after the beam shutter between the connection of two stainless steel guides to prevent the Turbine from damage, in case by accidental vacuum loss after the beam ports. Therefore, almost no neutrons with energies below the aluminum neutron optical potential are supplied to the user experiments. Following the theory in section 2.2.2.2, in addition to loss inside the bulk material the velocity dependent neutron transmission is also affected by the surface roughness of the foil with dependence $\propto 1/v^2$ (see eq. (2.20)). This loss factor can be determined by measuring the initial count rate without any sample and then with a thin foil, minimizing the exponential loss inside the material.

$$T = \frac{f_{\text{foil}}}{f_0} = \frac{\tilde{b}}{4}\frac{k_{\text{c}}^4}{k_{\text{i}}^2}\left(1 + e^{-n\sigma_{\text{abs}}d}\right) \tag{3.8}$$

A series of TOF measurements including the up to now used separation foil, an empty measurement without any foil, and a new AlMg3 foil first unpolished and then polished are taken. In figure 3.6 the measured spectra at the EDM beam line at PF2 are shown. Comparing the measurement without any foil to those with foils, at high velocities almost no difference is visible. At lower velocities the spectra become more and more depressed which is explained by the $1/v$ velocity dependence of the absorption cross section of the bulk aluminum. The difference between the old and new foil is mainly caused by the higher thickness of the foil and the possibly slightly different material composition of the aluminum.

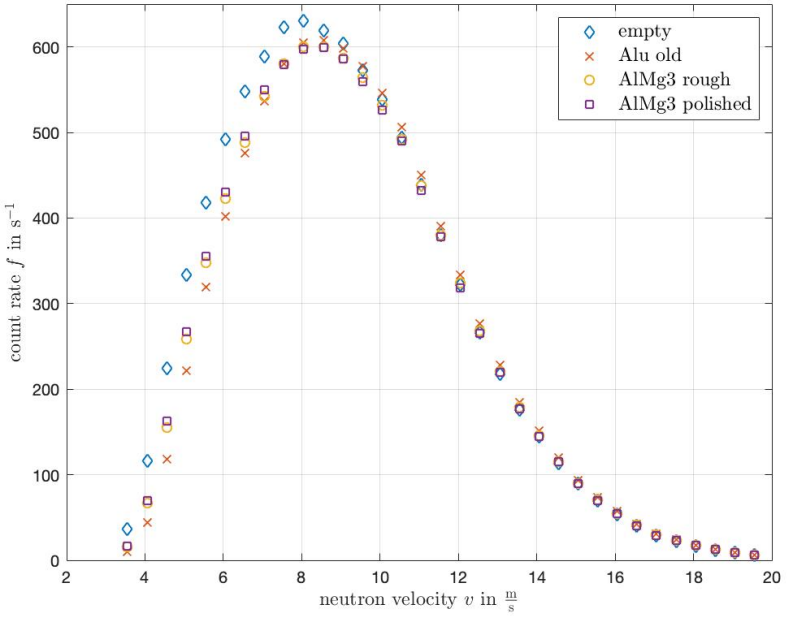


**Figure 3.6.:** Neutron spectra of the old aluminum separation foil, without any foil in between and with a new AlMg3 foil unpolished and polished taken at the PF2 EDM beam line. The error bars are smaller than the marker sizes.

Detailing the difference in transmission between the AlMg3 foil unpolished and polished, the surface roughness are defined by using the Garant ST1 [27], taking the roughness profile with a mechanical needle sliding a distance of 5.6 mm in one direction across the examined surface. This measurement was repeated two times perpendicular to each other, at six randomly selected positions on the surface, to reveal if any preferred direction was imposed by polishing. This gives an initial roughness for the unpolished foil of

$R_a = (0.36 \pm 0.03)\,\mu m$ & $R_z = (2.62 \pm 0.17)\,\mu m$ and after the manually polishing a surface roughness of $R_a = (0.04 \pm 0.01)\,\mu m$ and $R_z = (0.20 \pm 0.02)\,\mu m$. An additional evaluation of the raw surface roughness profile data was performed to determine the micro roughness and correlation length according to equation (2.18), applying the method presented in [28]. Similarly to the outcome in [28] no correlation length could be detected which might be limited by the resolution of the measurement equipment itself.
In figure 3.7 the transmission of the polished foil is divided by the transmission is shown, where the increasing transmission of polished surfaces at lower velocities is explained with the surface roughness model in equation (2.20). The slightly lower transmission for high velocities might be explained by flux differences of the provided beam. No beam monitor could be used due to the closeness to the turbine, hence this can not be reconstructed. The data is fitted weighted with its inverse squared errors with $T_{rel} = v^{-2} + off$. The fit parameter and the goodness of fit are depicted in table 3.2.

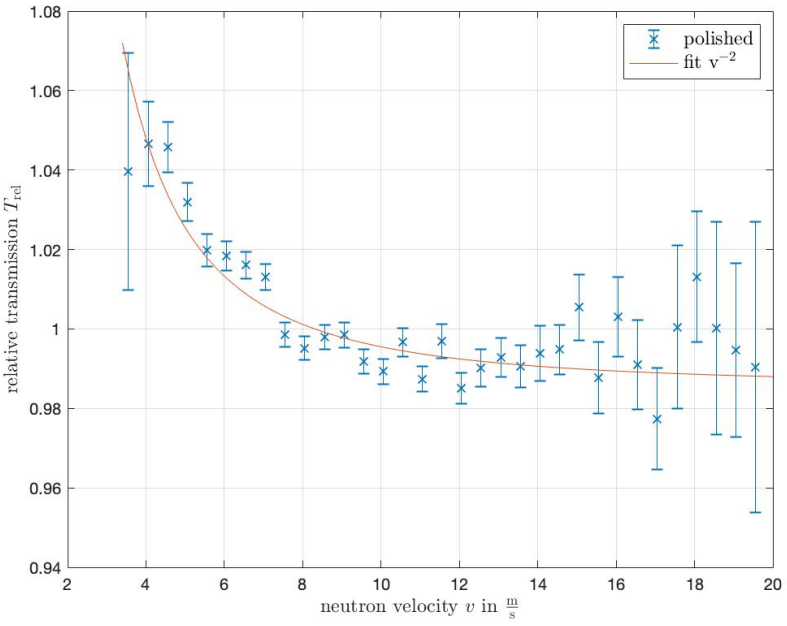


**Figure 3.7.:** Transmission of the polished foil normalized to the unpolished foil fitted with $v^{-2} + off$ according to equation (2.20). The errorbars arise from counting statistics

**Table 3.2.:** Goodness of fit and fit parameter of the surface dependent transmission correlation $1/v^2$.

| | |
|---|---|
| TOF offset | $(98.6 \pm 0.1)\,\%$ |
| $\chi^2_{dof}$ | 1.56 |

## 3.3. Stainless Steel Guides

A commonly used material for UCN guiding is stainless steel ISO 1.4401 and 1.4404, which is additionally non magnetic, due to its high stress resistance, availability and quite high neutron optical potential (see tab. 2.1), corresponding to a maximum reflection velocity of $v = 6\,\frac{\mathrm{m}}{\mathrm{s}}$. Reducing losses and to minimize non-specular reflection they are highly polished to very low roughness far below the guided neutrons wavelength (see 2.2.2.2). Since a high fraction of the neutron flux provided by the turbine is directed more or less parallel to the guide walls the incident angles are small and thus even UCNs with higher energies are transported towards the experiment. No hard cutoff can be seen at the time of flight spectra (see fig. 3.6).

### 3.3.1. Other Guide Standard

Highly polished stainless steel guides with 79 mm inner diameter are commonly used guides at the PF2 EDM beam line which are additionally coated with a NiMo thin film increasing the guided the optical potential (see tab. 2.1). With a flux maximum at $v_{\mathrm{max}} = 8.3\,\frac{\mathrm{m}}{\mathrm{s}}$. Since these guides can be used for years it is of interest how good still the transmission of these guides is and if they could be improved such as by cleaning.
The spectra of the PF2 EDM beam line at a distance of 1.65 m behind the beam shutter and the spectra after an additional guide length $L = 952\,\mathrm{mm}$ are measured. The corresponding velocity dependent transmission is calculated with equation (2.21) and shown in figure 3.8. The lower cut off velocity is defined by the minimum horizontal velocity $v_{\mathrm{Al}} = 3.4\,\frac{\mathrm{m}}{\mathrm{s}}$ neutrons need to have to overcome the potential of the aluminum alloy separation foil between the beam port and the experiment, as well as of the detector. The transmission for high velocities reaches a maximum at roughly 94 % and decreases for lower velocities. The decrease can be explained, since slow neutrons stay longer inside the guide and bounce more often on its surface, increasing the chance to be absorbed or scattered out of the UCN regime. Hence, the loss rate depends on the number of bounces.
Applying equation (2.22) to the integrated count rate over the whole spectra the normalized velocity averaged transmission $T$ per guide length $l$ in meter is obtained.

$$T_{\varnothing 79} = (0.91 \pm 0.01)^{l/\mathrm{m}}$$

The loss rate itself could be influenced by a thin contamination layer (see chap. 2.4.3) condensed onto the guide surface, consisting for example of hydrogen or greases, which might have build up over time. Thus, methods are investigated to increase the transmission by cleaning them in order to give a better comparison to new electro polished guides which were only exposed for a relatively short time to air.
A $\varnothing 67 \times 600\,\mathrm{mm}$ guide is measured at the PF2 TES beam line without any preparation and a second time after cleaning it by hand with acetone and isopropanol using lint-less tissues. The relative transmission of the cleaned to the uncleaned guide is determined (see fig. 3.9). This reveals an increasing transmission towards slower neutrons of up to 2.3 %, whereas at the beam maximum at $8.3\,\frac{\mathrm{m}}{\mathrm{s}}$ its 2 %.
With this rough method already a gain is observable, which could mean for cleaning them properly with an ultasonnic bath and backing them under vacuum in a oven an even higher transmission could be achievable.

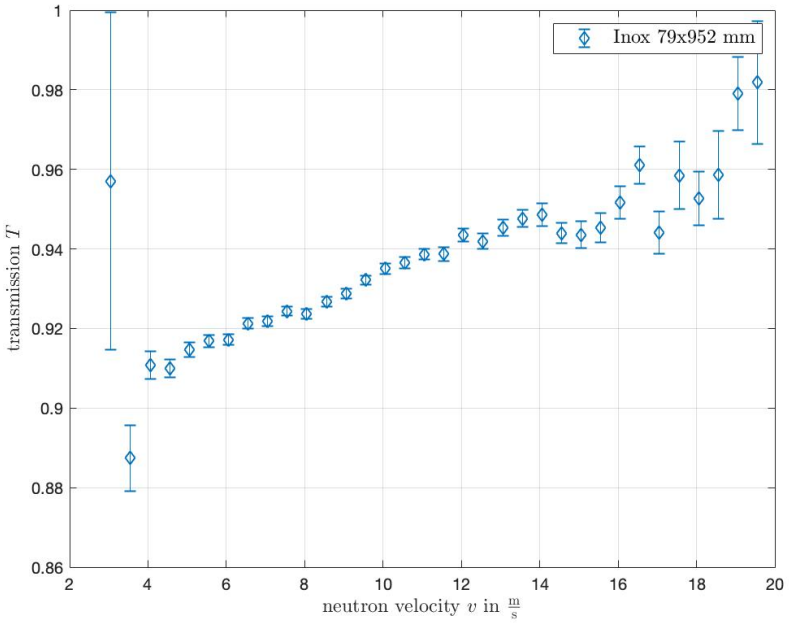


**Figure 3.8.:** At the PF2 EDM beam line determined velocity dependent transmission of a $\varnothing 79 \times 952\,\mathrm{mm}$ long stainless steel guide coated with a NiMo thin film, normalized to the spectra of the measured 1.65 m behind the beam shutter with the horizontal TOF set-up.

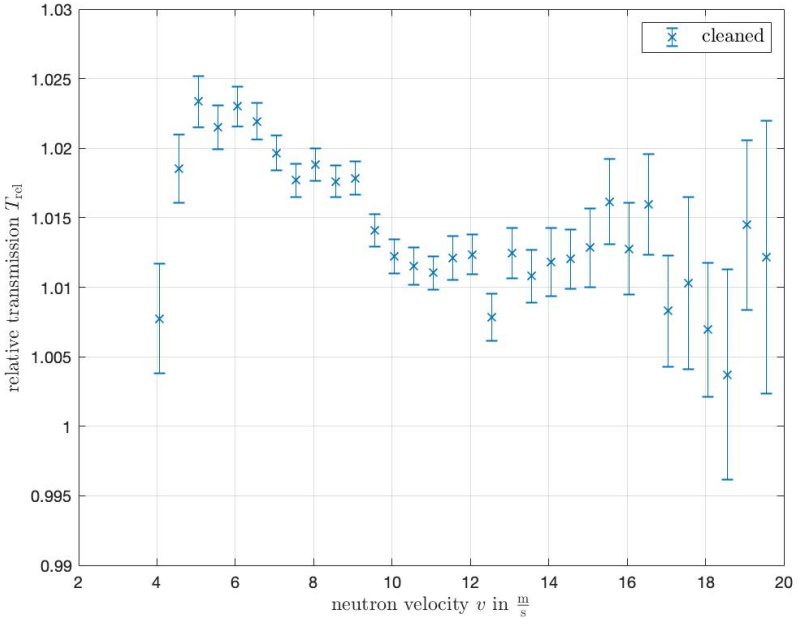


**Figure 3.9.:** At the PF2 TES beam line determined transmission of a hand cleaned steel guide normalized to its spectrum before cleaning.

### 3.3.2. ∅50 mm Guides

For superthermal $^4$He sources operated in 'fill and empty' mode the delivered UCN density at the experiment strongly depends on the ratio between the production volume and the volume to be filled. However, the UCN guide width also limits the neutrons mean free path and therefore cannot be arbitrarily reduced, as increasingly wall collision rates lead to higher losses as discussed above. Compromising between the optimum width and commonly available guides with highly polished inner surfaces, DN50 tubes with an inner diameter of ∅50 mm and electro polished surfaces from Kiesel Steriltechnik are chosen. The roughness of the guide segments is measured with the tool ST1 from Garant [27] to $R_\mathrm{a} = (0.06 \pm 0.01)\,\mu\mathrm{m}$ and $R_\mathrm{z} = (0.42 \pm 0.06)\,\mu\mathrm{m}$.

#### 3.3.2.1. Straight Guides

The transmission of the guides is measured for three different guide lengths 0.1 m, 0.5 m and 1 m and, since the method used to reduce the guide cross section could influence the transmission by shaping the spectra. This is repeated for each kind of reduction: Tapered and hard-edged. The total transmissions for each length and reduction is plotted in figure 3.10, whereas the normalized transmission of the guide is obtained by fitting each data set with an exponential decay, neglecting effects of gaps and alignment. The fit has two free parameters $c(l) = a \cdot \exp(b * l)$, where $a$ represents the initial count rate at zero length and $T(l) = \exp(b)$ the transmission per meter guide length. The errors arises from Poisson statistics and the fit is weighted with its inverse squared error. An additional error for gaps and alignment differences between each set up is assumed to 1 % and added to the statistical error. This is estimated from optical alignment with a manually positioned laser measure and the manual horizontal alignment with a spirit level.

$$T_\mathrm{edge} = (0.88 \pm 0.04)^{l/\mathrm{m}}$$
$$T_\mathrm{tap} = (0.89 \pm 0.02)^{l/\mathrm{m}}$$

Since the neutron propagation in both guide reduction systems is equal within its errors, it can be assumed that it is not affected by the kind of reduction apart from possible velocity dependence not seen here. Therefore, the normalized transmission is calculated taking the mean transmission of both values with its weighted errors.

$$T_\mathrm{norm} = (0.89 \pm 0.03)^{l/\mathrm{m}}$$

The 2 % difference to the old guide, with an inner diameter of ∅79 mm, can be explained by the lower mean free path, therefore more scattering events at the same guide length which is proportional to more losses.
Obtaining a more sophisticated statement about the transmission without any effect of the kind of reduction a measurement should be conducted putting a long guide section of the same dimension as those to be tested and measuring one length after another. Possible gap losses between two guides could be determined by measuring guides with different lengths separately, then assembled in row. Comparing to the transmission of a guide which has the same length as the assembly would then provide an estimate of the effect of gaps and misalignment.

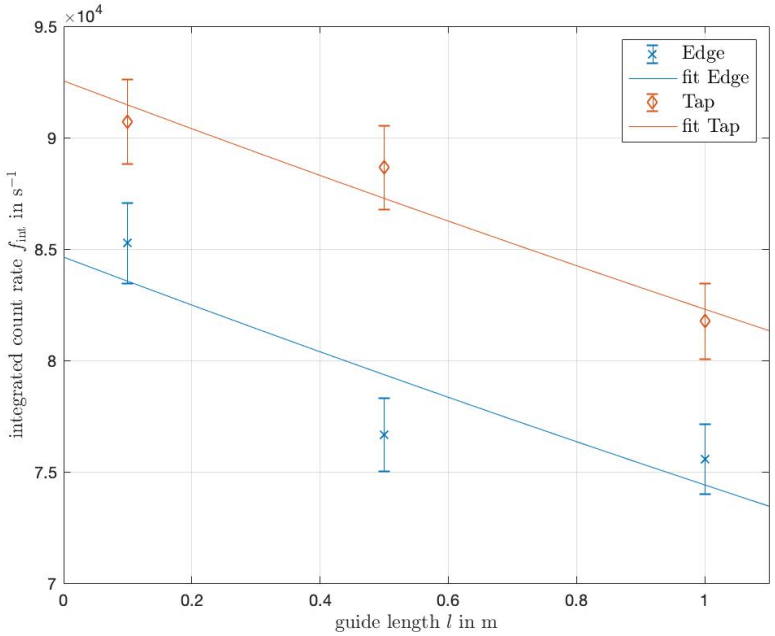


**Figure 3.10.:** Integrated counts for different for three different guide lengths measured for the hard-edged and tapered reduction. To the statistical error a systematic 1 % error due to misalignment and gaps is added. The data are fit with an error-weighted exponential function $c(l) = a \cdot e^{(b \cdot l)}$ providing the initial count rates $a_{\mathrm{edge}} = (8.8 \pm 0.4) \times 10^4\,\mathrm{s}^{-1}$ and $a_{\mathrm{edge}} = (9.7 \pm 0.2) \times 10^4\,\mathrm{s}^{-1}$, and the transmission $T(l) = \exp(b)$ for the edge $0.88 \pm 0.04$ and tap $0.89 \pm 0.02$.

#### 3.3.2.2. Reductions

In order to further improve the neutron density delivered to the experiments the relative transmission after a one meter guide section is measured for two different kind of reductions from ∅79 to 50 mm, determining if any flux can be gained by geometry. The angle and length of the taper are defined by geometrical considerations allowing a greater angle of neutrons to enter the smaller guide section at a minimized diffusive behavior after the tap. This is solved by setting the reduction angle as low as possible while keeping the length short, reducing the amount of bounces needed per incident neutron on the taper which would in turn would lead to diffusive behavior up to redirection and a higher fraction of scattered out neutrons.
A quick approximation of the expected count rate can be done by dividing the cross section of the reduced diameter 20 cm$^2$ by the initial 47 cm$^2$ leading to a transmission of 42 % assuming the flux as uniform within the guide. The first one measured is a 15° tapered 12 cm long highly polished stainless steel reduction piece (see fig. 3.11) (a)) and the second is a simple reduction piece with an hard edged step (see fig. 3.11) (b)).

Comparing the count rates at each length in figure 3.10 an offset between the taper and the edge is already recognizable, and by taking the average of the transmission for the edge and tapered reduction and dividing them with the above obtained normalized transmission $T_{\mathrm{norm}}$ gives transmission of $0.37 \pm 0.03$ and $0.44 \pm 0.04$.
Gaining more information, the velocity dependent transmission is examined for both kind of reductions after 1 m guide section (see fig. 3.12). It has to be mentioned that the spectra of the shorter guide sections show the same behavior as the 1 m guide. This is chosen as representative hence the beam already propagated long enough suppressing any not considered side effects of reducing the diameter. The data for the other guide lengths are provided at the appendix B. The transmission for the edge slightly decreases from

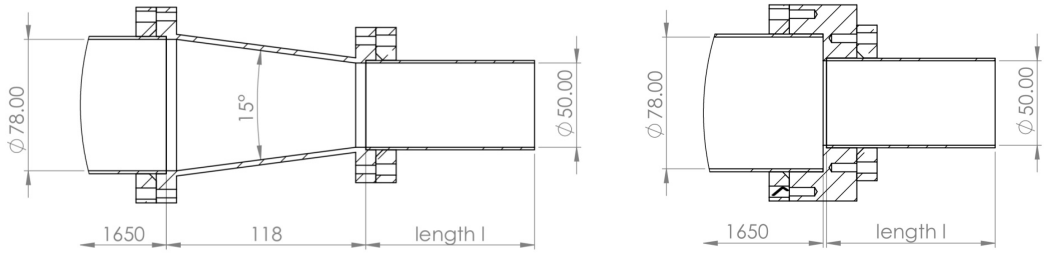


**(a)** **(b)**

**Figure 3.11.:** Drawing of the (a) tapered and (b) hard-edged reduction with the assembled guides.

0.38 to 0.35 from higher to lower velocities, due to the increasing rate of wall reflections. Contrarily, the transmission of the taper increases towards lower velocities starting at the same level up to 0.39 at $6\,\frac{\mathrm{m}}{\mathrm{s}}$. Hence, the TOF set-up only resolves the velocity component directed along the beam axis the increase could explained by the above already geometrical considerations, allowing a higher fraction of neutrons to entering the smaller guide by bouncing 'up' the taper which are more likely not as good directed as at the initial beam. The steep increase for velocities lower than $6\,\frac{\mathrm{m}}{\mathrm{s}}$, which was already seen in previous measurements [25], might result from background treatment which could still include the lower tail of the spectra. To define if any physical effects are in- or excluded further examination and different background methods should be applied. Additionally the observed behavior could be investigated by Monte Carlo simulations of the neutron flight path, together with measurements for reduction with different taper angle. Reducing uncertainty in the total energy by suppressing transverse components, a collimator could be placed before the TOF set-up allowing only directed neutrons to enter the set-up.

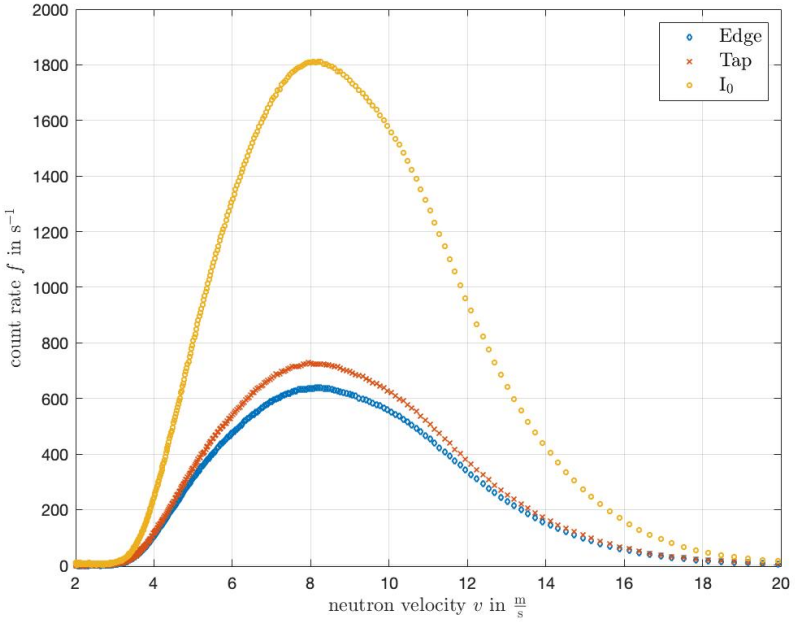


**(a)**

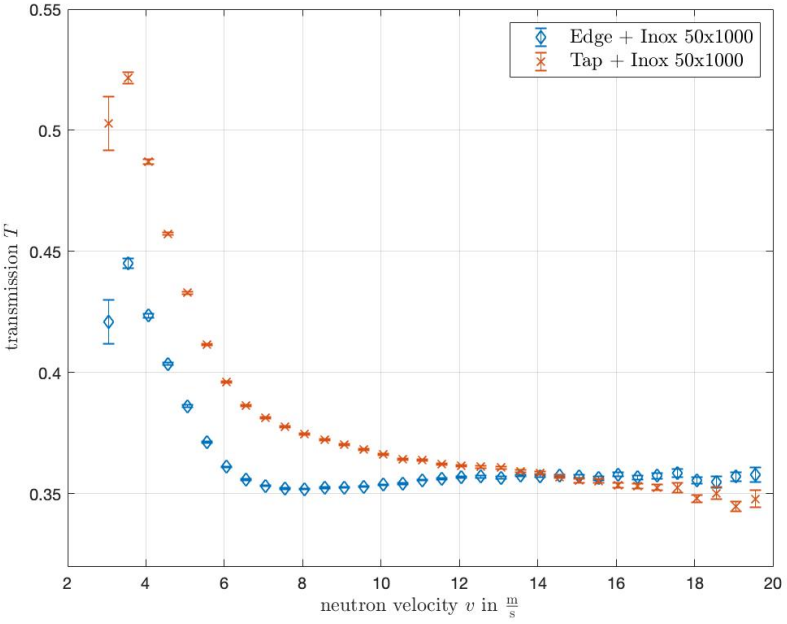


**(b)**

**Figure 3.12.:** Velocity spectra (a) and transmission (b) of the tapered (red) and hard-edged reduction (blue) reduction after an additional ⌀50 mm×1 m guide section normalized to the measured initial spectrum (yellow) before the reduction pieces.

#### 3.3.2.3. Bend Sections

Changing the direction of UCN beams can be done using of simple bent guide sections. In this thesis bent guide sections are used, due to the ease of mounting, enabling an easy spectra change by mounting any length of guide sections in between, obtaining the wanted velocity spectra, and due to the bottle closing mechanism constraints explained in section 4.3.4. The transmission of bent guides is velocity dependent through the curvature radius, angle of the bend, and diameter of the guide. Whereas, smaller diameter, radius and angle lead by geometry to higher angular spread of the beam as well as the reflection angle for a higher fraction of the incoming neutrons are larger leading to a higher loss, hence a higher fraction is above the critical reflection angle. Therefore, each guide section is characterized with neutrons.
Together with the by measurements obtained information and by measuring the transmission spectra of the switch (see sec. 3.5), which has the same guiding dimensions as the 60° bend, statements about the transport efficiency of the switch can be made. Also the final delivered spectra at storage bottle due to the lifting and the transmission through the full set up can be estimated. Additionally, by knowledge of the transmission of the 90° bend the initial spectra before the vertical TOF set-up at the experiment can be estimated (see sec. 3.1.2).
The transmission of two bends with equal radii of curvature $r = 70\,\text{mm}$ for different angles 60° and 90°, shown schematically in figure 3.4, are measured and are plotted in figure 3.13. As above explained, in figure 3.13 neutrons with lower velocities have a higher transmission than faster ones and the transmission for the 60° is higher than the 90° bend. The crossing, at $10\,\frac{\text{m}}{\text{s}}$ might be explained by the reactor power change from 50 to 35 MW between the measurement, leading to a 20 % reduced integrated count rate. However, the relative spectrum change shows a velocity dependence, differing from 15 % at the maximum and increasing towards the tails by more than 8 % (see. app. A.1). This together with the probably non constant flux during the operation at reduced power might lead to a spectral shift for the measurements of the second normalization and bend.

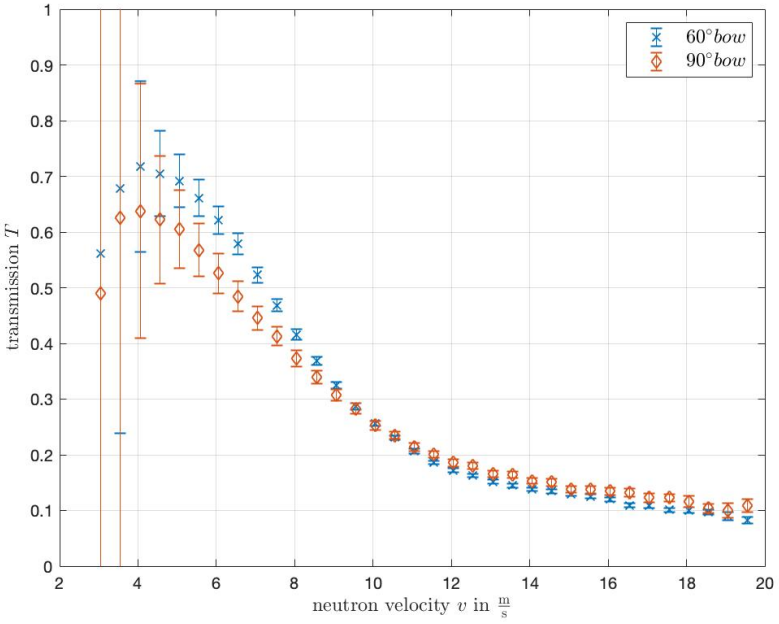


**Figure 3.13.:** Transmission of 60° and 90° bends with radius of 70 mm. The errors arise from Poisson statistics. An additional error due to the power change of the reactor between the two measurements is not considered.

## 3.4. NiMo and Cu Coated Glass Guides

At experiments where the neutrons need to be delivered in an specific polarization state, such as at neutron EDM measurements, it is very important to use non depolarizing guides. At the PF2 NiMo coated glass guides are used fro efficient guiding of faster neutrons. The spectra produced by superthermal $^4$He sources is far below the the spectra delivered at PF2. Therefore, the velocity dependent transmission of NiMo and Cu guide of velocities in the range $0 < v < 10\,\frac{\mathrm{m}}{\mathrm{s}}$ needs to be known. Since $3.2\,\frac{\mathrm{m}}{\mathrm{s}}$ is the minimum velocity provided at the PF2 beam lines the characterization is done by raising the beam line using the previous calibrated steel guides and vertical TOF set-up described in section 3.1.2.

### 3.4.1. Experimental Set Up

The neutrons' interaction with the gravity is used to shift the spectrum (see sec. 2.1.3) by lifting the experiment, assembling the calibrated NiMo and uncoated switch after each other connected vertically with a 0.5 m long guide section in between. This leads to a height difference of 0.57 m at the experiment (see fig. 3.14), similar to the draft in figure 3.4. Therefore, the velocity is lowered by $3.3\,\frac{\mathrm{m}}{\mathrm{s}}$ providing an expected count rate maximum for the TES beam line without any transmission losses by the bent sections of $5\,\frac{\mathrm{m}}{\mathrm{s}}$. Respectively the $\varnothing 50 \times 700$ mm NiMo and Cu coated glass guides are measured using the vertical TOF set-up, by mounting the 90° bend characterized in previous section and a 0.1 m stainless steel guide between the glass guide and the chopper. Hence, measuring with the chopper and detector at the same height as the raised guide, no information could be recorded for neutrons with energies below the detector aluminum separation windows Fermi potential would again be lost.

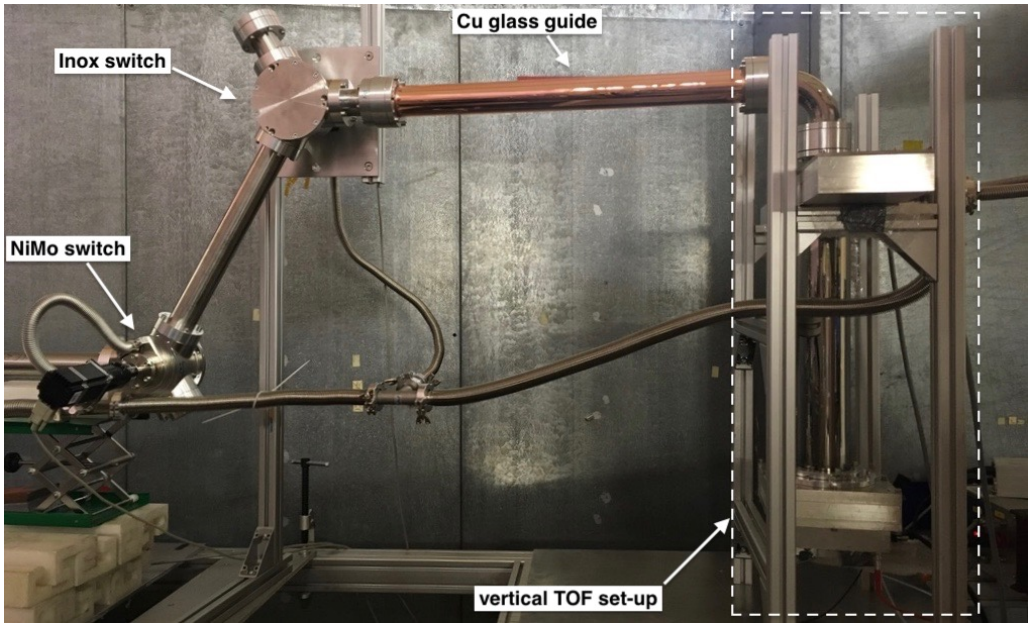


**Figure 3.14.:** Picture of the raised set up measuring the transmission of the Cu coated glass guide which was leveled in the horizontal plane. The lifting is realized by mounting the two switches vertically connected with a 0.5 m long guide in between. The TOF set-up is aligned vertically (dashed lines) and connected by the previous measured 90° bend with an additional guide leading to an overall dropping distance of 0.7 m.

### 3.4.2. Lifted TOF Measurements

With the above described set-up, the UCN beam is not only shifted towards lower velocities but also transformed to a distribution propagation vectors with lager average angle to the guide axis due to the bend sections. The lifting can be neglected, as the system before the glass guide is kept constant, contrary to the changed TOF set-up with its 90° bend that severely affects the transmitted spectra. Therefore, no certain absolute statement can be given, but by comparing the transmission of the glass guides to each other, obtained by division with the measured spectra at the vertical set-up without any guide in between still gives detailed information about the guided velocities. The lifted spectra measured in the set-up with two switches is dented around the maximum (see fig. 3.15 (a)). This is not observed at spectra measured with a switch and the 60° bend and therefore might be an effect of the switch positioning and gaps in between. Since, this effect seems to be persist even after the glass guides the transmissions are calculated and depicted in 3.15 (b))
Comparing the transmission for the NiMo and Cu guide, NiMo tends to have a slightly higher transmission for neutrons with velocities below $5\,\frac{\mathrm{m}}{\mathrm{s}}$. Taking the difference between the averaged transmission in this range the NiMo coated guide has a $(2.3 \pm 0.4)\,\%$ transmission. Providing a more precise statement a measurement should be conducted repeatedly at a higher flux beam such as the PF2 EDM using a set-up that only allows horizontal neutrons to propagate through the guide. However, the obtained transmission already shows that the non depolarizing copper coated glass guide can be used instead of the NiMo guide without additional losses.

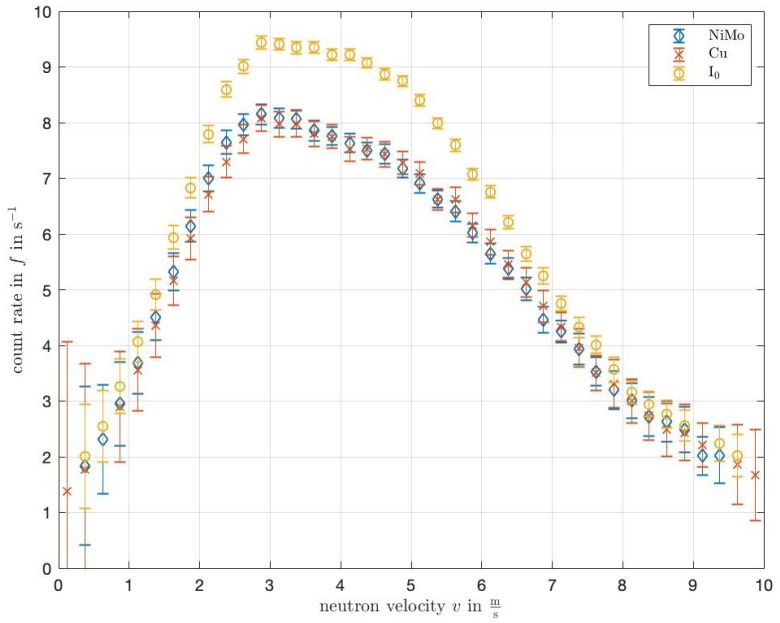


**(a)**

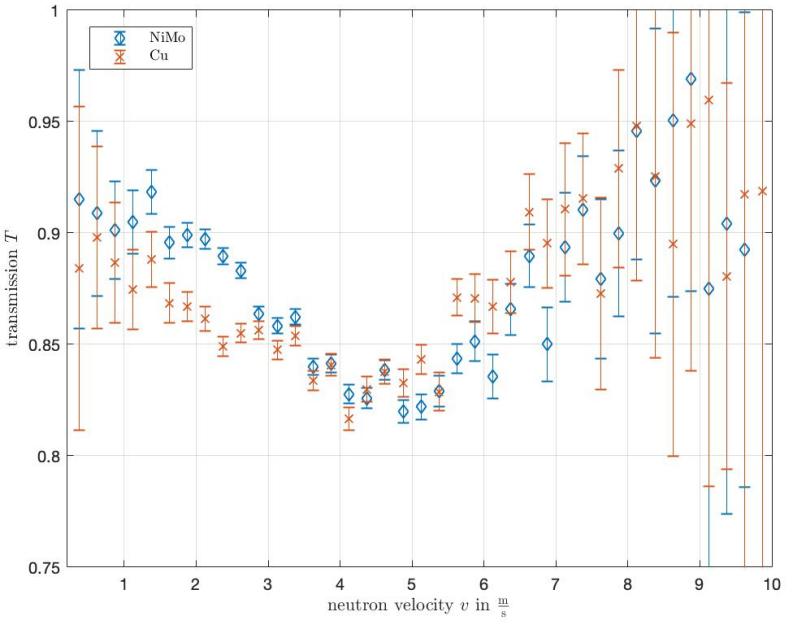


**(b)**

**Figure 3.15.:** Velocity dependent spectra (a) of the $\varnothing 50 \times 700$ mm NiMo and Cu coated glass guides at the 0.57 m lifted set-up measured with vertical TOF an the corresponding transmission (b) normalized to the spectra measured in the same configuration without the guide.

## 3.5. Three Way Neutron Switch

In order to fill and empty the storage bottle through a single aperture a switch with high transmission and low leakage rate is needed. With these goals, together with low weight and the possibility of conveniently operating it in any three dimensional alignment, the three way switch is designed reaching the lower technical limits of mechanical manufacturing. It follows the idea of an existing stationary switch at the ILL. The transmission of the switch is measured at the PF2 EDM eam line in horizontal alignment with a $^3$He detector on one output port and the velocity resolved transmission is measured with the TOF set-up at the other output port. At the TES beam line additionally the transmission at a 0.57 m lifted level with the vertical TOF set up is defined, providing information for the transmission at low velocities.

### 3.5.1. Mechanical Design

In the following a detailed description of the design and functional elements of the switch are given. Whereas, a focus is set to reach high transmission and low leakage at an optimized performance.

#### Inner dimensions

The first limit of the switch design is set by its three in-/outlets which should deliver neutrons with equal transmissions. Therefore, a rotating switch design with equally spaced openings at 120° is chosen. As a compromise between the outer dimensions, weight and desire for the maximum applicable radius of the curvature, the latter is set to $r = 70$ mm (see fig. 3.16 cross section A-A). The dimensions of the inner rotary part with the milled pockets are chosen to reduce weight without compromising stiffness, and to keep the center of mass on the rotation axis to minimize torque at the feedthrough and motor. To reach a high UCN transmission with low gap losses, the clearances between the body and the insert are set to f7/H7 allowing a frictionless movement while constraining the gaps between 28 µm in the best and 108 µm in the worst case. This includes the maximum play for the 20 mm×42 mm SKF 6004 ball bearings, with an achievable play of 8 µm [29] and enough free space for additional thin material coating, such as titanium to absorb leaking neutrons. As depicted in figure. 3.16 (cross section B-B), the lower bearing is completely fixed within the bearing seat of the body and the upper one is centered by the top center ring and pressed in its vertical position by a specially designed spring washer, which is tensioned by the mounted sealing cap. The stationary sealing is done by a circular grove in the body suited for a 3 mm Viton o-ring. In order to reach high vacuum at the bottom of the body a KF16 flange for vacuum pumping is foreseen.

#### Guide connection

Apart from the functional inner body design good alignment with the connected guides is mandatory to avoid losses by steps, gaps and misalignment. Each flange is kept in position by two ∅6 mm dowel pins, which are aligned to the center of the guide hole better than 20 µm. The guide sections are kept perfectly centered and aligned by the flange, whereas the design is adapted from Babin [30]. The flange consists of two parts: The outer ring presses the guide onto the surface of the body, via a stainless steel o-ring clamped in a small machined grove on the guide; and the center piece, which is centered by the outer shell and due to its dimensions aligns and centers the guide inside. The vacuum sealing is achieved by Wilson flange technique, which is a simple face at the end of the inner ring dimensioned for a 3 mm viton o-ring. Contrary to commonly used fitting holes in bodies for guides, this design enables to dis-/assemble the guides on and off without moving the switch, which therefore can be mounted in a fixed position.

**Surface finish**

To achieve the highest neutron transmission the bent hole inside the rotary part is machined at a five axis CNC milling machine and later on polished by hand. It and together with the other guiding surfaces of the body are polished to a roughness $R_a = (0.04 \pm 0.01)\,\mu m$ and $R_z < (0.32 \pm 0.02)\,\mu m$, as measured with the ST1 surface measure from Garant [27], which is even below the roughness of the electro polished neutron guides (see sec. 3.3). The surface profiles from the roughness measurements are additionally examined with the method presented in [28] in order to determine any micro roughness correlations, which could lead as explained in section 2.2.2.2 to losses of up to 25 %. Variation of parameters does not reveal any by the polishing technique caused micro roughness correlations, which might be due to the limited resolution of the measurement tool. Additionally one of the two switches is coated on the guiding surfaces with a 0.5 µm NiMo layer, allowing higher angles of incidence due to its higher neutron optical potential, and the outer walls of the well and inner wall of the body are coated with Ti to avoid leakage of neurons by absorbing any that escape the guide (see tab. 2.1).

**Weight**

By conducting simulations with the CAD tool SolidWorks, the minimum allowable wall thicknesses of the switch without significant bowing due to the pressure differences between the high vacuum of $10^{-7}$ mbar inside towards the atmospheric pressure 1 bar is calculated. This includes a by good engineering judgment defined safety margin of 25 %. Together with the other mentioned measures above, the weight of the switch is reduced to 9 kg for non magnetic stainless steel DIN-ISO 1.4404 as material, which is chosen to additionally guide polarized neutrons at low loss rates.

### 3.5.2. Operation and Positioning

Because, the switch needs to drive to more than three positions in any 3D operation mode, three possible in-/outlet connections plus possible storage positions, no simple mechanical position switches can be used. The positioning problem is overcome by the use of a linear stepper motor with micro positioning operated in closed loop, giving information about the motor while it moves and holds. The motor is directly connected to the feedtrhough (MDC, ZBRM-275-Enc) and controlled with a single axis motor controller (MDC, MCS-1), which allows to store positions as needed [31]. However, the feedthough shows a backlash of 1° when changing the sense of rotation. Therefore, an initial calibration point is programmed to pretension the feedthrough, which needs to be approached counterclockwise. The three set points are approached clockwise keeping the tension inside the feedhrough to avoid misalignment due to the backlash.
Unfortunately, the motor controller loses the initial point after powering off. In such cases the feedthrough needs to be positioned manually with the angular scale at the feedthrough counterclockwise to the marked position and then the power can be switched on. The motor positions automatically to the next full step, which gives the needed initial precision. Although the switches performed well during the measurements reported in this thesis, some measures could be taken to improve the performance. These include a high precision feedthrough with less than 0.1° play instead of the current one, and an initialization marker such as a laser barrier with an input to the MDC controller, which would make the first manual positioning obsolete.

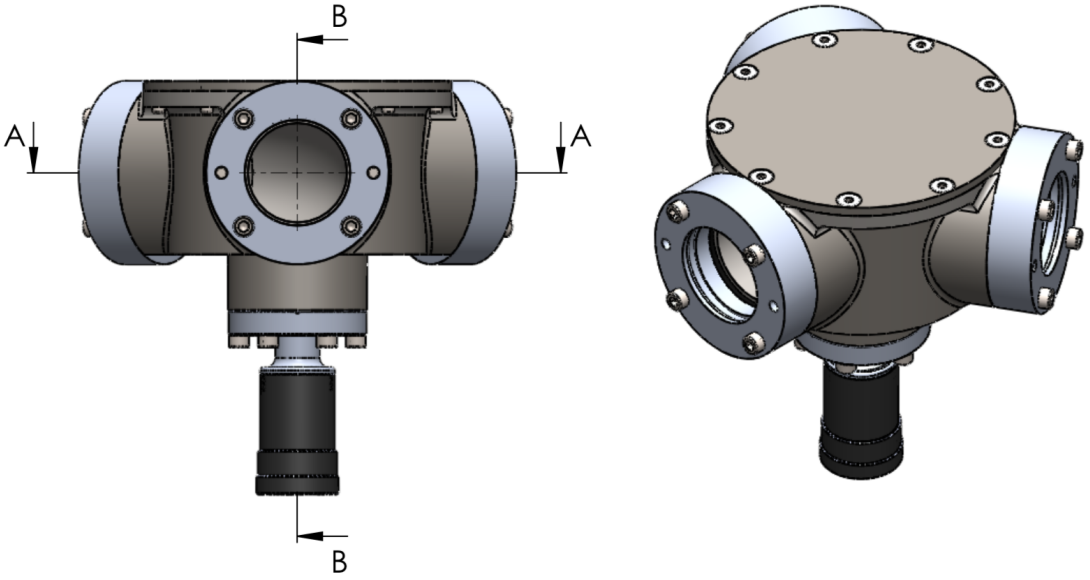


**(a)** front and 3D isometric view of the switch with connected feedthrough

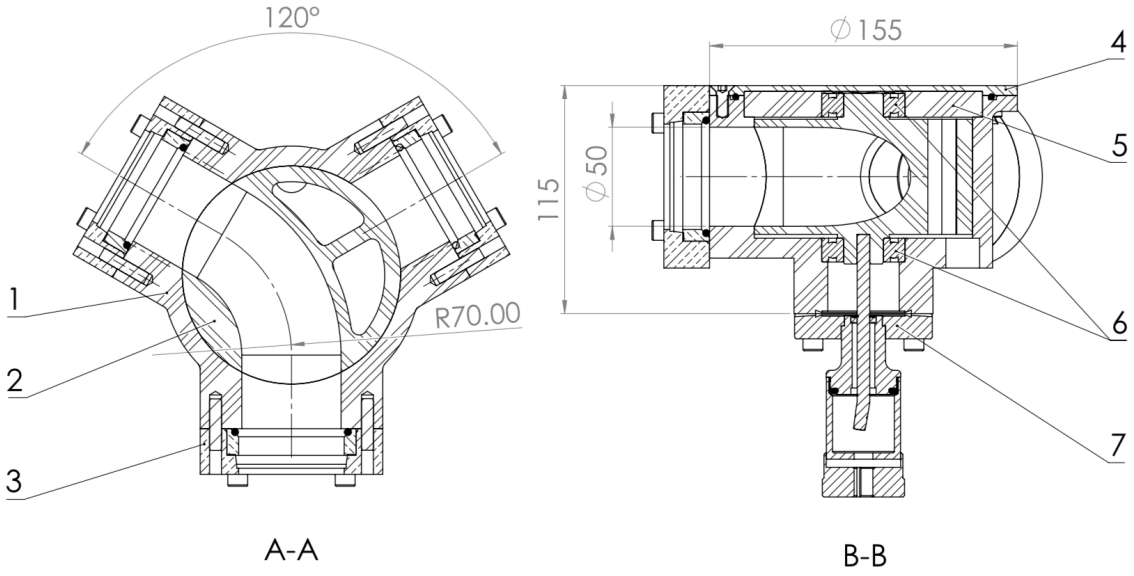


**(b)** Traverse and coronal cross section indicated in (a)

**Figure 3.16.:** Plan of the assembled three way neutron switch made of non magnetic stainless steel with dimensions in millimeters at the in (a) indicated traverse A-A and coronal B-B cross sections (b). In A-A are depicted the body (1) with the turnable inlet (2). The aluminum flanges (3) are attached with screws and centered by dowel pins. In the side cross section B-B the sealing with the top cap (4) and top centering of the well bearing with the center ring (5) is shown. The insert is kept in position by steel bearings (6) at the top and bottom and is rotated by a mechanical welded bellows feedthrough (7) from MDC vacuum, driven by a stepper motor.

### 3.5.3. Characterization of the Switches with UCNs

Two identical switches are manufactured and calibrated, with different coatings applied to the body and insert. One switch stays uncoated and the other one is coated with NiMo on the guiding surfaces, which should lead to a higher transmission of faster neutrons due to its higher optical potential, and coating of the inner walls of the body and outer walls of the insert with Ti minimizing the leakage by absorption.

#### 3.5.3.1. Calibration

In order to calibrate the switch's rotation position to a maximum transmission by saving the set-points as described in the manual of the motor controller, the switches are first roughly aligned by eye and three set points are saved. The point of maximum transmission is calibrated with neutrons by changing the angle in small steps 0.1° and measuring the integrated counts with the TOF set-up until the maximum is reached for the left and right exits. Before turning to a different angle for the calibration, the initial point is always approached as described above, and afterwards the new set-point is driven. The third set point which connects both calibrated exits is determined by counting the steps of both calibrated set points, subtracting the smaller number from the higher (left - right), dividing it by two and adding the step number of the left exit. Figure 3.18 shows the transmission at an angular deflection of up to ±2.5° normalized to the identified maximum of both exits. Within a range of ±0.5° the rate decreases by 3 %, which could be, apart from the geometry, either due to possible play in the feedthrough or the fact that mainly very slow neutrons that are guided on the walls of the curvature might be affected which are not measured with the horizontal TOF set-up. For the right exit the count rate seems to decrease less within a rotation angle of ±1°, which could be caused by the short measurement time for each set point or a up to now not considered higher play due to possible friction at the feedtrhough or the bearings.
However, since the maximum count rate differ less then 3 % the time of flight spectra are taken for both calibrated set-points of the NiMo coated switch, showing equally count rates and identical spectral distribution. The maximum integrated count from the left to the right differs by 2 %, which could be caused by surface contamination or even small difference from construction. Comparing them to the initial spectra, after the calibrated straight ∅50 mm guide section, a shift towards lower velocities, similar to the 60° bend can be recognized. Further analysis of the transmission of the switches is presented in the following chapters.

#### 3.5.3.2. Leakage

The complementary leakage rate of the NiMo coated switch is measured with two different detector systems attached on the exits of the switch, at the PF2 EDM beam line. On one side the TOF set-up is mounted and on the other side a $^3$He detector, which are interchanged after several runs. The leakage rate is measured while the switch is guiding the neutrons towards the other exit, where the maximum count rate is measured with the other detector system. For the $^3$He detector the sum of the total counts are taken and divided by the detector live time leading to a count rate of $f_{^3\mathrm{He}} = (1.1 \pm 0.4)\,\mathrm{Hz}$ and for the cascade detector with the TOF set-up the leak rate of $f_{\mathrm{cas}} = (0.9 \pm 0.3)\,\mathrm{Hz}$. An additional short leakage test for the third set-point, connecting both detectors, did not reveal any increased leakage.
The uncoated switch is only measured with theTOF set-up at the PF2 TES beam line revealing a leak rate of $(0.4 \pm 0.3)\,\mathrm{Hz}$. To determine the leakage, the obtained count rates

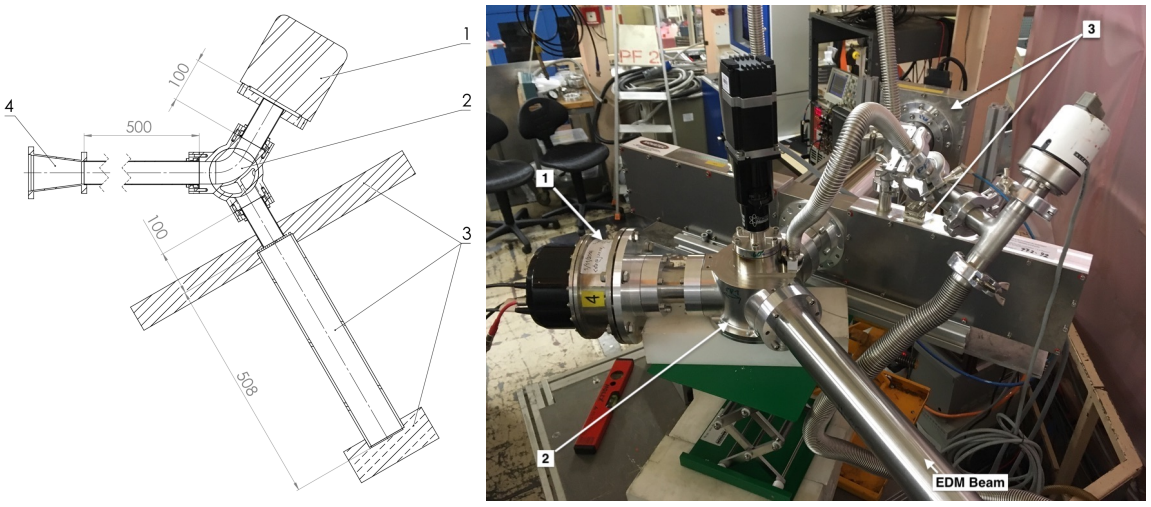


**(a)** Top cross section **(b)** Assembly at PF2 EDM beam line

**Figure 3.17.:** Plan and assembly of the NiMo coated switch (2), installed at the PF2 EDM beam using the reduction piece (4). The calibration measurements are conducted by use of the TOF set-up (3) on the right and the $^3$He detector (1) mounted on the left side.

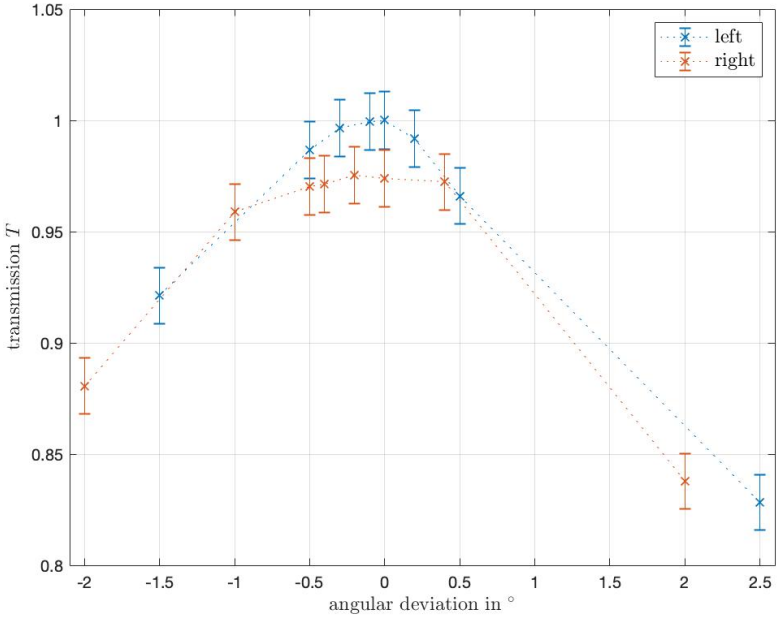


**Figure 3.18.:** Transmission depending on the angular deviation from the flux maximum. The transmission is normalized to the maximum integrated count rate of both exits. The errorbars arrise from statistics with an assumed 1 % error due to the short measurement time.

are divided by the measured initial counts before the switch.

$$L_{\mathrm{NiMo}} = (0.6 \pm 0.2) \times 10^{-5}$$
$$L_{\mathrm{uncoated}} = (4 \pm 2) \times 10^{-5}$$

Comparing the results gives a 6.6 times higher leakage for the uncoated switch, which is already in the leakage regime of commonly used shutter valves between $10^{-5} - 10^{-6}$. The coated switch is already at the lower end of this range. The leakage despite of the Ti coating might be explained by reflection between the body and the insert, where even for a negative potential of Ti the neutrons have a finite reflection probability without absorption. Additionally neutrons might enter the unshielded detectors from outside. To improve the bounds on leakage, longer measurements with shielded detectors and calibrated backgrounds are needed. This would have exceeded the measurement time available at PF2 for this work.
A possible measure to further suppress the leakage would be geometrical optimization of the rotary insert design, such as concave regions on the side with the same outer dimensions as the guide width, directing neutrons into the material and absorbing them. The quality of the coating should be also imporved, since it did not adhere perfectly to the stainless steel on several points. At other points it was and was far thicker than the allowed tolerance and had therefore to be sanded off.

#### 3.5.3.3. Full spectral transmission of the NiMo coated Switch

The full transmission spectrum of the uncoated switch is determined at the PF2 TES beam line in two steps. The spectra above the threshold velocity of 3.2 $\frac{\mathrm{m}}{\mathrm{s}}$ calculated from the neutron optical potential of the aluminum separation foil is measured with a horizontal TOF set-up aligned to the turbine exit. For lower velocities a 0.57 m lifted set up is used leading to an expected shift of the maximum velocity from 8.3 $\frac{\mathrm{m}}{\mathrm{s}}$ to 5 $\frac{\mathrm{m}}{\mathrm{s}}$. The transmission is determined similarly to in section 3.4 with the vertical TOF set-up (see sec. 3.1.2).
The comparability of the initial horizontal count rate to the count rate measured with the vertical set-up is experimentally determined by measuring the TOF spectra at the lifted set-up twice: Once in direct mode with the horizontal TOF set-up and then a second time with the vertical set-up. The spectra are compared by multiplying the horizontal spectra with the transmission of thd90° as determined in section 3.3.2.3, see figure 3.19. The obtained velocity maximum at 4 $\frac{\mathrm{m}}{\mathrm{s}}$ is below the expected peak velocity without transmission loss. The shift can be explained by a higher transmission towards lower velocities, as observed for the switch calibration and verified for transmission of the bends.
Contrary to the expectations for the horizontal measurement the spectrum reaches its maximum at 5.2 $\frac{\mathrm{m}}{\mathrm{s}}$ and seems already to decrease more steeply than in the horizontal plane, before the Al threshold velocity reached. This might be explained by the shaping of the initial directed beam towards a broader angular distribution at the two bent sections and therefore many still faster neutrons with a lower perpendicular velocity to the separation foil are less likely to pass the separation foil. Whereas, for the vertical set up all neutrons dropping down the full length gain enough energy to pass it.
Another explanation of the difference between the calculated to the actual measured count rate could be the creation of a 'storage' volume due to the vertical guide components above the chopper. Although the chopper blades are made of an neutron absorbing material neutrons bouncing on shallow angles have still a high probability not to be absorbed. This could lead to a buildup density of neutrons propagating at high angles to the guide axis, and artificially enhance the low-velocity tail of the measured spectrum, explaining also the non zero tail at the lower velocity end

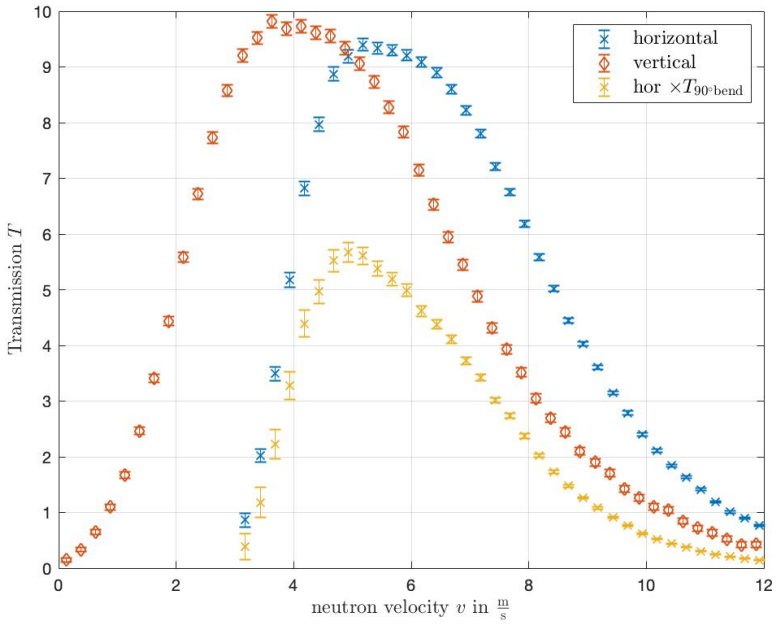


**Figure 3.19.:** Count rate after the switch as a function of velocity measured for the lifted set up with both horizontal TOF and vertical TOF set-up. The o indicate the by use of the 90° bend transmission approximated count rate by multiplying the horizontal with the in section 3.3.2.3 obtained transmission.

As discussed above the projection of the 3D velocity vector onto one component at the TOF measurements the count rates are not comparable. Albeit, for the transmission of the switch only relative statements of the initial maximum count rate measurements can be made and therefore, comparing them might still be valid. The transmission of the switch in horizontal alignment, shown in figure 3.20, has nearly the same behavior as the 60° bend. Whereas, the relatively worse transmission towards lower velocities could be explained by gaps between the rotating part and the body and the additional guide. A further suppression is perhaps explained by the hand polishing of the guide surfaces, which leads inevitably to a higher surface waviness then electro polishing due to pressure differences during the first grinding steps.
However, the more than 20 % difference in transmission in the overlapping velocity regimes for the lifted and not lifted measurements needs to be discussed in more detail. One reason might be the relatively good transmission of very slow UCN (more than 85 %) and the quite high propagation angle of the neutrons, due to the two bend sections before. This is only minorly affected by the additional curvature of the switch, as shown in the following experiment with two switches (sec. 3.5.4). Another already mentioned, is that all neutrons passing the 90° are dropping down and are detectable due to the vertical energy gain, whereas, for the horizontal measurement this is not the case.
In conclusion, the combination of both set ups shows an increasing transmission towards velocities below 3.2 $\frac{\text{m}}{\text{s}}$ of up to 95 % and a transmission rate similar to a simple bend with the same dimensions can be achieved. To properly determine the transmission of the switch, measurements have to be done to only transmit the still directed beam parts for both set-up, as for example by a collimator. Another possibility could be measuring the whole lifted measurement set up 90° rotated onto the horizontal plane to get information about the increasing angular propagation losses.

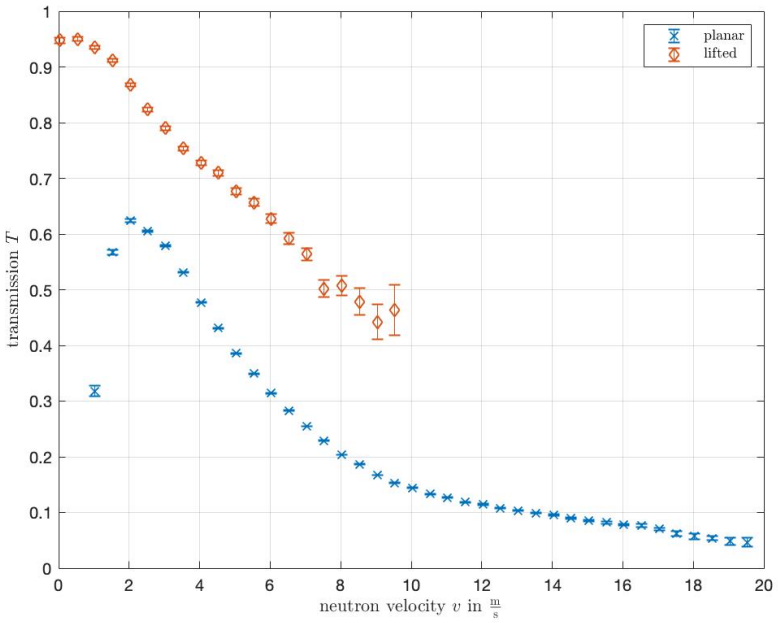


**Figure 3.20.:** Transmisson of the switch for the horizontal measured spectra (blue) and of the transmission of the 0.5 m lifted (red) measured with a vertical TOF set-up obtaining velocities below the by the Aluminum foil limited minimum velocity 3.2 $\frac{\mathrm{m}}{\mathrm{s}}$.

### 3.5.4. Assembly of two Switches

In order to determine if the spectra further changes after it has been already shaped by a first bend the velocity dependent transmission is measured by assembling the NiMo switch after the uncoated switch, as shown in figure 3.21. The transmission after each switch normalized to the spectra before the assembly is depicted in figure 3.22. As expected and previously discussed, a higher transmission is observed at low velocities declining towards higher velocities. The offset at the high velocity tail can be explained by the additional gaps at the switch and the guide section. Also should be mentioned, that the normalization and transmission measurements are conducted at the to 35 MW lowered reactor power after shut down.
The relative transmission is obtained by dividing the transmission after the second switch with the transmission after the first one, revealing a lower velocity sensitivity giving a higher transmission towards faster neutrons. The further depression might be explained by the fact that the neutron propagate at larger angles per added bent section and therefore are more likely scattered out or are absorbed. Additionally some of the less directed neutrons might not overcome the potential barrier to enter the detector, as already discussed above. This observation also provides also an explanation for the increased transmission for the lifted switch set-up relative to horizontal in the previous section.

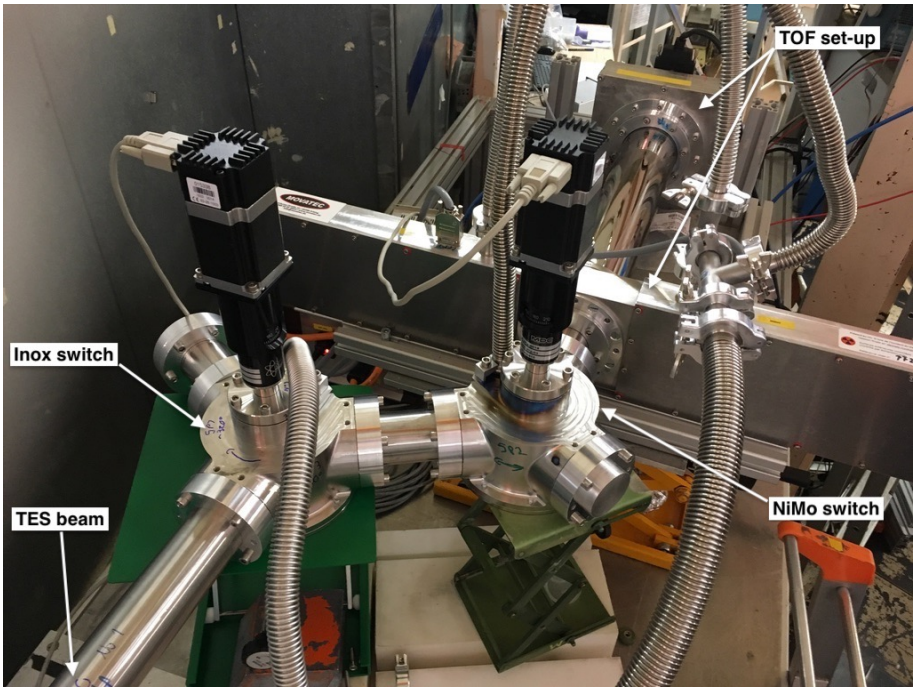


**Figure 3.21.:** Picture of the TOF set-up of the switches assembled in series connected with an 0.1 m long guide section in between. The unused exits of the switches are blind flanged.

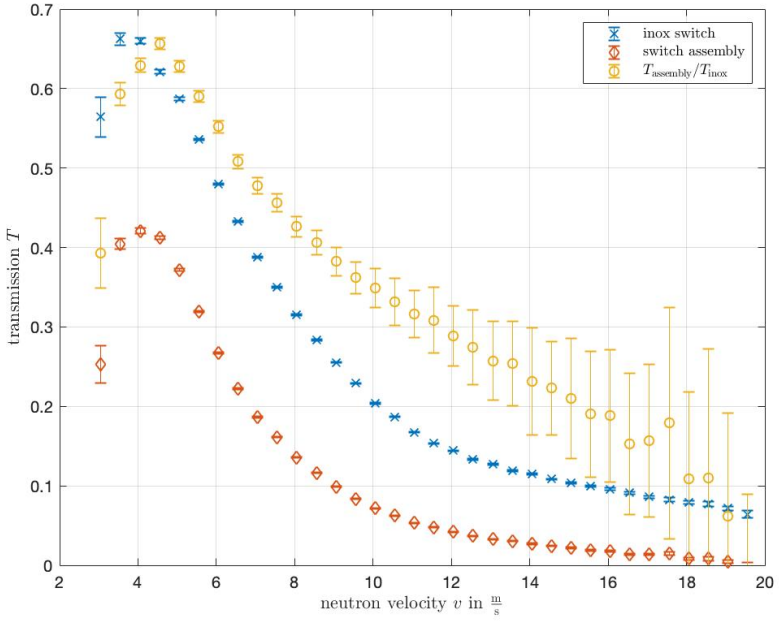


**Figure 3.22.:** Velocity dependent transmission after two switches assembled in series compared to the transmission after the first switch and the relative transmission of the second switch to the first one.

### 3.5.5. Relative Detector Efficiency

In this thesis two different UCN gas proportional counters which rely on different neutron absorption media are used. On the one hand, the cascade detector absorbs UCN in a thin 10-Boron layer using the 10B(n,alpha)7Li reaction, together with a in a common gas electron multiplier detector system [24]. The charged $^4$He and $^7$Li ionize the counting gas,producing an electron cloud which is directed toward the readout by the applied electrical field. Consequently, the count rate strongly depends, besides the absorption cross section, also on the applied high voltage, the thickness of the absorbing material as well as the purity and flow of the detection gas. It may additionally depend to some extend on the material, thickness and surface roughness of the separation foil, as shown in section 3.2.
On the other hand, a $^3$He detector is used, where neutrons are detected by absorption inside a volume filled with $^3$He, which decays into a proton and a tritium, ionizing gas in the tube by losing their decay energy. These electrons are directed by an electrical field to the anode, where a charge pulse event for each absorbed neutron occurs, giving a pulse height distribution. Therefore, the system also depends on the roughness and properties of the separation foil and even more on the gas pressure which determines the sensitivity of the energies of the detected neutrons through the absorption cross-section, as well as the level of the applied high voltage. Therefore using both detectors simultaneously a calibration has to be done since the previously described effects for each detector leads to different overall neutron detection efficiency.
The efficiencies are obtained by use of the data from the calibration measurements of the switch (see sec. 3.5.3), where both detectors are respectively attached to the left or right exit measuring the maximum flux by switching between both positions. The calibration measurement with the TOF set-up of the switch reveal almost the same count rates, merely differing by 2 %. For both spectra the integrated counts are taken and their inherent detector backgrounds are subtracted. For the TOF set-up this is done as described in section 3.1 and for the $^3$He detector by dismissing counts below the threshold bin for the proton detection, defined by the left minimum of the neutron pulse spectra. Pile up events in the $^3$He detector are also dismissed manually by a cut off after the combined tritium and proton event, which is set at the end of the steeply decreasing flank. The count rates are defined by dividing the actual live time of the detector using the same weighted averaging and error propagation as described in 3.1. To recalculate the spectra for the cascade detector initially arriving at the chopper, a factor for 1/2 is proposed for measurements with neutrons by [32] due to the geometrical aperture of the chopper. Since, optical and mechanical measurements reveal a factor of $(36 \pm 1)$ % [25, 26]the average is taken of both values with an assumed uncertainty for the 1/2 factor of 5 % leading to $0.44 \pm 0.05$. This gives a final $^3$He to cascade efficiency of:

$$\text{cascade}/^3\text{He} = 0.41 \pm 0.07$$

The error arises from counting statistics combined with the relative experimental uncertainties like the small count offset for both exits of. The errors of the 3He detector are defined by the only several ten seconds long live time that might deviate, as well as its possible sensitivity to higher energy neutrons are taken into account. For the TOF set-up the recalculation of the amount of neutrons arriving at the chopper by its geometry has a significant effect, as well as the background treatment.

The quite high difference might result from several circumstances, in particular the thickness of the 10-Boron layer. For thin layer thickness many neutrons will just pass through without being detected and for very thick layer the produced ions could not leave the detection material anymore. If the pressure of the $^3$He detector is set too high the fraction of detected faster neutrons might have an significant effect. Also the detector electronics and changing

the voltage has a high influence on the detection efficiency which is for the $^3$He detector to $V_{\mathrm{He3}} = 1100\,\mathrm{V}$ and cascade detector to $V_{\mathrm{cascade}} = 1300\,\mathrm{V}$
However, the obtained efficiency is in good agreement with two other experimental results conducted at the ILL with the same detectors: A gold foil activation experiment [25] at the EDM beam line and measurements in direct mode for both detectors measured at the UCN beam line [26].

**Table 3.3.:** Estimated systematic errors for the measurements to determine the detector efficiency.

| error source | estimate in % |
|---|---|
| $^3$He live time | 2 |
| $^3$He fast neutron sensitivity | 2 |
| chopper geometry | 5 |
| cascade background treatment | 2 |

## 3.6. Conclusions on the Handling System

The guiding elements and switch presented in this chapter, which are used for the storage time measurements in the following chapter, are characterized by measuring the TOF spectra in a standard horizontal configuration. To investigate the velocity regime below $3.2\,\frac{\mathrm{m}}{\mathrm{s}}$ a lifted set up is successfully conducted with a vertically oriented TOF set-up. Since TOF measurements just provide are only selective to a one-dimensional projection of the 3D velocity vector of the neutrons, only relative transmission statements for the vertical TOF can be given.
An overview of the results for all elements and assemblies examined in this chapter is given in the following:

1. The proposed $1/v^2$ **transmission dependence on the surface roughness** discussed in section 2.2.2.3 could be demonstrated by measuring the transmission of an AlMg3 foil before and after polishing.

2. The average **transmission of the highly polished stainless steel guides** with an inner diameter of ∅50 mm is determined to a normalized transmission of $T_{\mathrm{norm}} = (0.89 \pm 0.03)^{l/\mathrm{m}}$. The present guide standard of highly polished and NiMo coated stainless steel guides with an inner diameter ∅79 mm is evaluated at $T_{\mathrm{norm}} = (0.92 \pm 0.02)^{l/\mathrm{m}}$. Whereas, cleaning by hand revealed a slight increase of transmission of $(2.0 \pm 0.2)\,\%$, which could be perhaps increased by more sophisticated cleaning methods. The velocity dependent transmission for two ∅50 mm guide sections 60° and 90° bent with a radius of $r = 70\,\mathrm{mm}$ is determined. An average transmission for the 60° bend of 38 % and for the 90° bend of 42 % was obtained at the spectral maximum count rate of $8.3\,\frac{\mathrm{m}}{\mathrm{s}}$.

3. Comparison of the transmission of the **NiMo and Cu coated glass guides**, measured at the lifted set-up with vertical TOF, gives similar transmissions of $(82 \pm 1)\,\%$ at the highest count rates, suggesting that Cu coating has equally high transmission as NiMo. Whereas, towards lower velocities the transmission of the NiMo coated guide seems to increase to 90 % while Cu reaches only 85 %. For increasing velocities the transmission for both guides increases, where, contrary to the expectations on the optical potential, for the velocity range above $6\,\frac{\mathrm{m}}{\mathrm{s}}$ the transmission of Cu is $(1.1 \pm 0.6)\,\%$ higher.

4. A new designed stainless steel **three way Neutron switch**, enabling to fill and empty the storage bottle through one aperture, is designed and characterized for a uncoated switch and a switch, which guide walls are coated with a NiMo thin film and outer walls coated with Ti. Leading to a transmission spectra similar to the 60° bended guide section at the same dimensions. Where the transmission at the TOF spectra maximum delivered velocity reaches merely $32 \pm 1\,\%$ for the uncoated switch. The leakage rate for both switches is determined to $L_{\mathrm{NiMo}} = (0.6 \pm 0.2) \times 10^{-5}$ and $L_{\mathrm{uncoated}} = (4 \pm 2) \times 10^{-5}$, which is already within and at the lower end of the leakage range of commonly used shutters.

5. Since two different neutron detector systems are used at the storage time measurement, the **relative detector efficiency** of a cascade and $^3$He detector is determined using the NiMo coated switch with both detectors attached on the left and right outlets, by switching the neutron beam between them. The final calculated and corrected detector efficiency of the cascade to the $^3$He is $0.41 \pm 0.07$, which is in agreement with two other experiments conducted at the PF2 [25, 26].

# 4. Storage Time Experiment

Increasing the UCN density in the production volume of superthermal UCN sources is one of the key elements to improve statistics at UCN experiments. According to (1.2) this can be only achieved by: increasing the production rate, which depends on the CN flux or by a better conversion media; and increasing the effective lifetime in the storage bottle. The storage can be realized by magnetic traps or non-magnetic wall materials with high optical potentials.
A effective process to obtain high quality walls is thin film coating of the chosen material on any substrate. In previous works a wide range of wall materials have been tested in various experiments and set-ups showing for most wall materials a far worse storage behavior than calculated, in [22] a broad overview is given. These 'anomalous losses' are mostly caused by a thin hydrogen contamination layer on the surfaces, where experiments with water repelling fluoropolymers closed the gap between theory and experimental results.
Therefore, in this chapter the previously characterized guide elements and three way NiMo switch are assembled together with a newly constructed storage time set-up, enabling experiments at ambient as well as cryogenic temperatures. A first storage time measurement at room temperature is conducted with this set-up for a storage volume coated with the fluoropolymer CYTOP, which has not previously been tested with UCN.

## 4.1. UCN Storage Bottle

The bottle used for the storage time measurement has the same dimensions as the one used at the superthermal source SUN II [8]. Its design is optimized to produce high UCN densities for experiments at the end of a cold neutron beam, see figure 4.1. At SUN II cold neutrons enter the bottle from the right through the 0.5 mm thin aluminum CN window. Inside they are converted into UCN by inelastic collisions with superfluid $^4$He gas inside the vessel, as described in 1.2.2. The UCNs accumulate inside the storage volume due to total reflection at the walls of the bottle and are finally extracted through a ∅50 mm extraction aperture at the left side on the top.
For the storage time measurement in this thesis the neutrons enter the bottle from the left side. The extraction aperture is closed with an aluminum blind flange and the left end flange is replaced with a mounting flange to screw the bottle onto the UCN guide feeding the storage time set-up. The neutron in-/outlet aperture is designed to enable a UCN leak tight sealing of the bottle with a plug closing the bottle from the inside and is moved in inward to open the bottle, as describe in detail in section 4.3.4. The width of the inlet is chosen to reduce the maximum occurring gap and minimize the heat radiated from the guide into the bottle. At the same time a focus is kept on maximizing the possibility of neutrons to enter and leave the bottle. The material of the bottle is aluminum to provide a good heat conductance. Due to the low optical potential of aluminum, it has to be coated with a thin film of material with a higher potential and low loss rates to store the UCN, as listed in table 2.1. A commonly used solution to reach high effective lifetimes is a thin film coating of Fomblin grease. Despite its disadvantages of outgassing and little control over

the surface thickness and its quite low potential 110 neV [10]. The potential is adressed with previous coating with high optical potentials such as NiMo in order to keep a fraction of higher energy neutrons inside the bottle. However, since at cryogenic temperatures Fomblin greases without any additional helping material tend to crack and crumble its usage is superthermal sources is limited.
In this thesis for the first time a thin CYTOP film is applied to a UCN storage volume. CYTOP has similar characteristics to Fomblin while solving some of its problems: it is in the solid phase at room temperature; and thin films can be simply dip-coated by dissolving in a special solvent. Attempts to coat the bottle with other promising materials, such as deuterated polyethylene (dPE) as developed in [33], were not successful due to constraints of time and needed modifications to the existing system. Due to the geometrical limitations of the design of the volume, no company could be found to coat it with diamond like carbon (DLC).

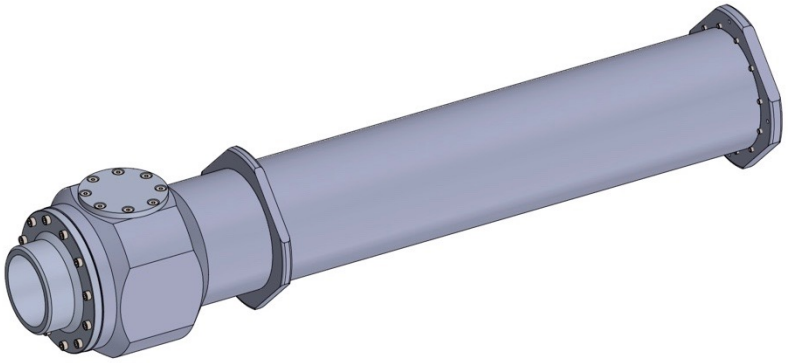

**(a)** 3D view


**(b)** left side cross section

**Figure 4.1.:** Plan of the storage bottle assembly, which is coated with CYTOP and tested in the storage time set-up. The CN flange (1) mounted on the right side of the storage bottle body (2),which has the same dimensions as the one used at SUN II. On the other end the connection flange (3) is mounted. The UCN extraction aperture is blind flanged with an aluminum cap (4).

## 4.2. CYTOP coating

Searching for new easy-to-coat storage materials, which could enable long storage times identified CYTOP, which seems to have fitting properties. The amorphous fluoropolymer CYTOP, as depicted in figure 4.2, is originally used in semi conductor industries as a dielectric coating and in optics as anti reflective coating. Its optical transparency, electric insulation, water and oil repellency, mould release and chemical resistance are desirable in a wide variety of technical applications [16] (see tab. 4.1).


**Figure 4.2.:** Draft of a cytop molecule and its amorphous chain taken from [16]

### 4.2.1. Properties of CYTOP

The most important factor for UCN storage wall material is the neutron optical potential, which can be obtained by calculating the number density of molecules from the mass density $\rho_{\mathrm{CYTOP}} = 2.03\,\frac{\mathrm{g}}{\mathrm{cm}^3}$, using the abundance and atomic masses of the molecule composition, for one oxygen ($m_{\mathrm{O}} = 15.999\,\mathrm{u}$), 10 fluorine ($m_{\mathrm{F}} = 18.998\,\mathrm{u}$) and 6 carbon ($m_{\mathrm{C}} = 12.011\,\mathrm{u}$). With the calculated molecular number density $n_{\mathrm{CYTOP}} = 4.397 \times 10^{21}\,\frac{1}{\mathrm{cm}^3}$ and the isotopically averaged scattering length for each atom in the molecule $b_{\mathrm{O}} = 5.805\,\mathrm{fm}$, $b_{\mathrm{F}} = 5.654\,\mathrm{fm}$ and $b_{\mathrm{C}} = 6.6484\,\mathrm{fm}$ [34] the optical potential for CYTOP can be calculated in equation (2.8):

$$V_{\mathrm{CYTOP}} = 117\,\mathrm{neV}$$

Even though, the to other wall materials (see tab. 2.1) comparably low optical potential, such as NiMo and dPE, it is still slightly above the value for Fomblin of 110 neV.
Additional the loss rate per bounce $\eta$ can be roughly estimated by use of equation (2.13) for the maximum store able velocity of $4.7\,\frac{\mathrm{m}}{\mathrm{s}}$ and using the sum of the theoretical inelastic scattering $\sigma^{\mathrm{sc}}$ and absorption cross section $\sigma^{\mathrm{abs}}$ for thermal neutrons [34] and using the correlation $\sigma \propto 1/v$.

$$\eta_{\mathrm{CYTOP}} = 3 \times 10^{-7}$$

The high effective lifetime of neutrons inside Fomblin is interpreted as partly slit sealing of the grease. The same effect can be achieved by the dip coating method of CYTOP. The special fluorocarbon solvent used for this has a boiling point at $100 - 180\,^{\circ}\mathrm{C}$, and contrary to Fomblin coats, the surface thickness can be easily controlled to below 1 µm by the pullout velocity [12,16]. By repeating the the dip process several times, thicker coatings are possible as long as the coating has not solidified by evaporation of the solvent. The solid phase is an additional benefit of CYTOP, since it does not outgas in high vacuum unlike Fomblin. It can be brought into a glass phase by baking out between 30 to 60 min at a temperature of 180 to 200 °C. A common advantage of Fomblin and CYTOP is their hydrogen repelling surface due to the structure of the molecules. For CYTOP the water absorption ratio is below 0.01 %, which means that hydrogen surface films are suppressed and therefore anomalous UCN losses are supposed to be avoided. Due to its electro-chemical properties CYTOP might be even usable at high magnetic and electric fields, or for storing and guiding polarized neutrons due to the high break down voltage and non-magnetic behavior of the long fluoromer chains may be compared to the properties of deuterated polyethylene [21]. In view of the surface strength and thermal expansion coefficient (see tab. 4.1) use of the coating on metals and glass at cryogenic temperatures should be possible without damaging or peeling off of the coated thin film.

**Table 4.1.:** Important material properties of CYTOP taken from [16].

| | |
|---|---|
| Density | $2.03\,\frac{\mathrm{g}}{\mathrm{cm}^3}$ |
| Break down voltage | $90\,\frac{\mathrm{kV}}{\mathrm{mm}}$ |
| Volume resistivity | $> 101 \times 10^{17}\,\frac{\Omega}{\mathrm{cm}}$ |
| Water absorptivity | $< 0.01\,\%$ |
| Linear expansion coefficient | $7.4 \times 10^{-5}\,\mathrm{K}^{-1}$ |
| Glass transition temperature | $108\,^{\circ}\mathrm{C}$ |

### 4.2.2. Coating process

Because CYTOP has not been used up to now for neutron optics or storage, a new method to coat the aluminum bottle and stainless steel plug had to be developed. The recipes for the different components were defined by adapting methods for previous successfully coating examples. These are documented at the application notes from the supplier AGC [12]. To coat the parts in one step the CYTOP Starter Kit was chosen.This consists of 100 ml CTL-107MK with 7 g of CYTOP polymer and 300 ml of CT-SOLV100K fluorosolvent. The objective was to cover the inner wall surface $A_{\mathrm{bottle}} = 1800\,\mathrm{cm}^2$ of the 3.8 l storage volume with an average 20 µm thick thin film. The coating adheres by a CONH-chain on the material surface, whereas for a dip coat speed of 60 mm/ min a surface thickness of <1 µm is achieved [12]. This process can be repeated several times as long as the surface is not completely dried, with an optimum waiting time of 1 to 10 minutes between successive dips and a substrate temperature of 70 to 120 °C. The substrates are cleaned before coating with a tissue and common cleaning agent by hand. Afterwards they are put in an isopropanol filled ultrasonic bath for 30 min. As last step they are cleaned with lint-free tissues and acetone by hand to remove any potentially remaining surface contaminations.

- **Assembled Bottle:** The dip-coating is conducted using the slightly modified oven for dPE coating [21], to enable coating bottles with greater length. The temperature during the coating process is set to 100 °C and a rotation speed of 6 rpm is used to reach surface thickness higher than 1 µm. To coat both flanges at the same time, the whole apparatus is tilted for 15 min to each side. The maximum tilt towards the inlet is chosen to avoid pouring out of the dissolved CYTOP. For the, the solvent level is set just a few millimeter above the center of the bottle rotation axis. At this point the temperature is increased to 150 °C to start evaporating the solvent. The whole apparatus is again tilted towards both ends ins sequence for 10 min. The coating process is finished when the solvent is completely evaporated.The CYTOP coating is baked after leveling the oven and increasing the temperature to 200 °C for 30 min. The high temperature baking also transforms the amorphous CYTOP phase to a glassy phase with a smooth surface. With this method a sufficiently thick coating should be achieved at the flange center. This gets thicker with increasing radius due to the evaporation of the solvent over time, and correspondingly reduction of the level of the liquid. Comparing the coating times of the flanges to the coating time period for the cylindrical wall of the bottle and assuming linear layer growth, the thickness on the walls should be roughly 2.5 times thicker than in the centers of the flanges. The minimum thickness is estimated to be greater than 15 µm assuming a minimum linear layer growth of 0.1 µm/turn. Here a lower value is given than in the manual due to the higher than recommended repetition rate that was chosen for thick layers.
- **Plug:** The plug is coated by manual dip coating with a pull out speed of the plug from the CYTOP solvent of $\approx 1\,\frac{\mathrm{mm}}{\mathrm{s}}$. This process is repeated 30 times with drying times of $1 - 5$ min and additional heating to roughly 80 °C at an oven in between the

dips. After the last step the plug is also mounted inside the oven to bake out the coating at 200 °C for 30 minutes. A minimum thickness of 15 µm is estimated for a growth rate per dip of 0.5 µm.

Evaluating the adhesion and uniformity of the coating by eye is barely possible due to its optical transmission higher than 95 % for visible light (see fig. 4.3). For the plug the difference of the coated to the uncoated surface is only visible by a slight difference in brightness under illumination. Evaluation of the closed bottle is impossible without destruction of the gap sealing coating. However, for mounting the inlet flange the plug needs to be unscrew and thus the interior could be examined. The edge of the coating perceptible as slightly milky in color. No further irregularities of the coating could be observed by eye. Therefore, the thin film layer was assumed as being successfully coated and the bottle was mounted at the storage time set-up. If the storage time already leads to a long storage time, this would be a strong hint for a successful coating.
Verifying the goodness of the coating as well as the optical potential further measurements are needed, such as neutron reflectometry and other optical methods.

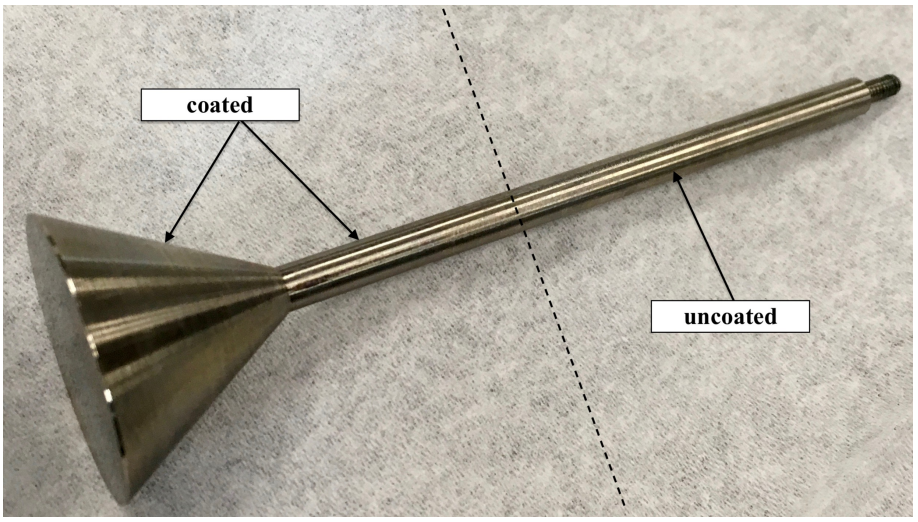


**(a)**

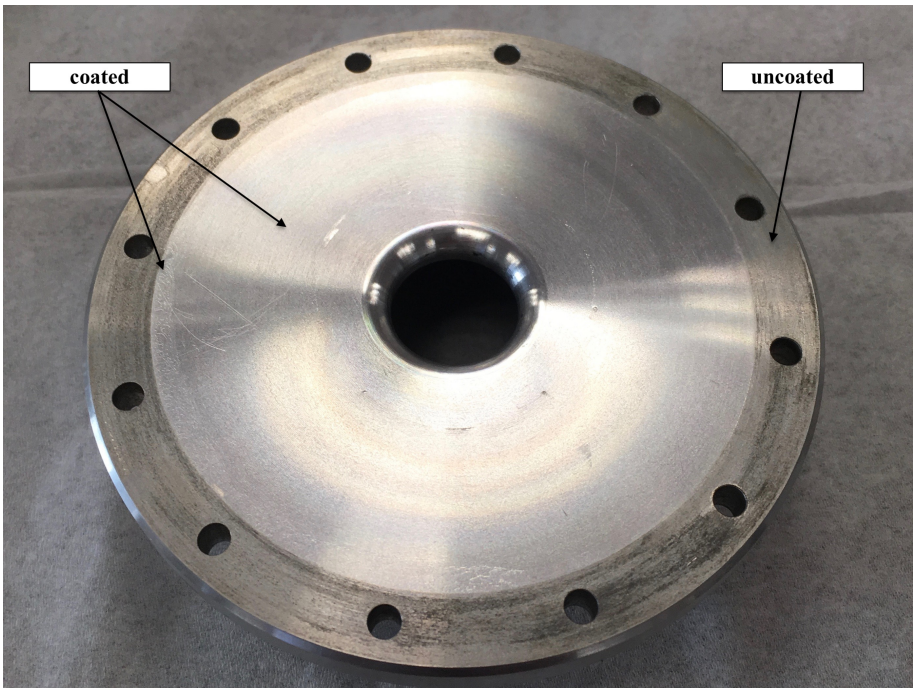


**(b)**

**Figure 4.3.:** Detail picture of the CYTOP coated parts. At the inox plug (a) almost no difference is visible. At the Al inlet flange (b) a clear difference in brightness is visible. The scratches on the surface already existed before the coating.

## 4.3. Experimental Set-Up

The storage time experiment itself relies on a apparatus that can be grouped in four main parts:

1. **The neutron handling system** to deliver a storeable spectrum with a high density in the storage bottle, as well as guiding them towards the detector with the least possible loss. The detector should also have a high efficiency.
2. **The vacuum environment** providing a suitable vacuum in the $10 \times 10^{-6}$ mbar, to minimize losses by scattering with residual gas and avoid contamination of the storage bottle walls at cryogenic temperatures.
3. **The cryogenic set-up** including the cooling mechanism, thermal shielding, and mechanical connections is needed to reach cryogenic temperatures.
4. **Storage mechanism**, apart from the storage bottle design and its wall material, the sealing mechanism plays a major role. It defines the incoming flux and affects the storage time by any gaps in its seal.

Considering the given boundaries together with further spatial and operating limitations the experiment depcited in figure 4.10 is developed. This provides a flexible set-up for testing different kind of bottles due to the modular design with DN250 flanges. The needed spectra with a high fraction of neutrons, with energies below the optical potential of the aluminum separation foils of the turbine and detector, are obtained by lifting the storage set-up by 0.57 m, as in the measurements reported in section 3.4.2 and 3.5.3.3. The storage bottle is mounted horizontally as at the superthermal source SUN II. Emptying and filling of the bottle through one opening is enabled by a rotating three way neutron switch. A linear plug closing mechanism is driven by a pneumatic cylinder, sealing the bottle from the inside. After storage the neutrons effuse out of the bottle, propagate through the guides and fall into the $^3$He detector, which is mounted onto the third exit of the switch. Due to the vertical velocity gain falling all neutrons arriving at the detector should be able to pass the aluminum separation foil. The storage bottle can be additionally cooled to cryogenic temperatures by use of a cold head, which is attached by thermal anchors with elastic hinges, to avoid damaging shear forces. In order to reach the lowest possible temperatures a thermal shielding around the storage bottle is connected to the first 40 K stage of the cold head. In the following sections detailed explanations of main components are given.

### 4.3.1. Providing neutrons

To minimize loss in the primary delivery guide, the set-up is installed 0.5 m behind the safety separation foil of the TES beam line at PF2. The guide width is first increased with a short $\varnothing 70 \times 300$ mm guide section, and then reduced with the tapered reduction piece, described in section 3.3.2.2. This is connected to the switch with a 100 mm guide. The raising is done, as described in section 3.5. The NiMo coated switch is mounted vertically and connected to the 60° bend with a 500 mm inox guide, leading to a height difference of 570 mm equivalent to a 3.3 $\frac{\mathrm{m}}{\mathrm{s}}$ down shifted velocity spectra.
The delivered spectrum is measured after the 60° bend with the vertical TOF set-up, which is shown in figure 4.5. For comparison, the spectrum measured with the horizontal TOF before the switch is also provided. The spectra arriving at the bottle is recalculated using transmission of the guides and bends defined in sec. 3.3.2. The transmission of the 90° bend is assumed to be constant towards velocities lower than 3.2 $\frac{\mathrm{m}}{\mathrm{s}}$. However, further losses have to be taken into account since the calibration was done before drilling the holes for the plug feedthrough and vacuum pumping at the right end of the one meter guide section. Also the steering rod reduces the neutrons mean free path leading to more wall interactions

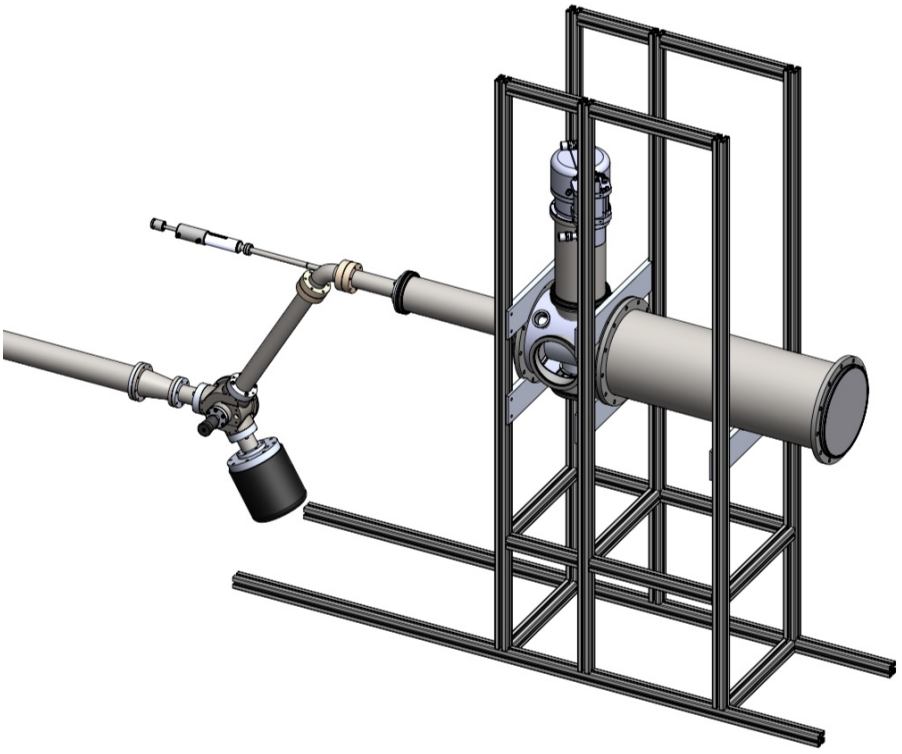

**(a)** 3D view

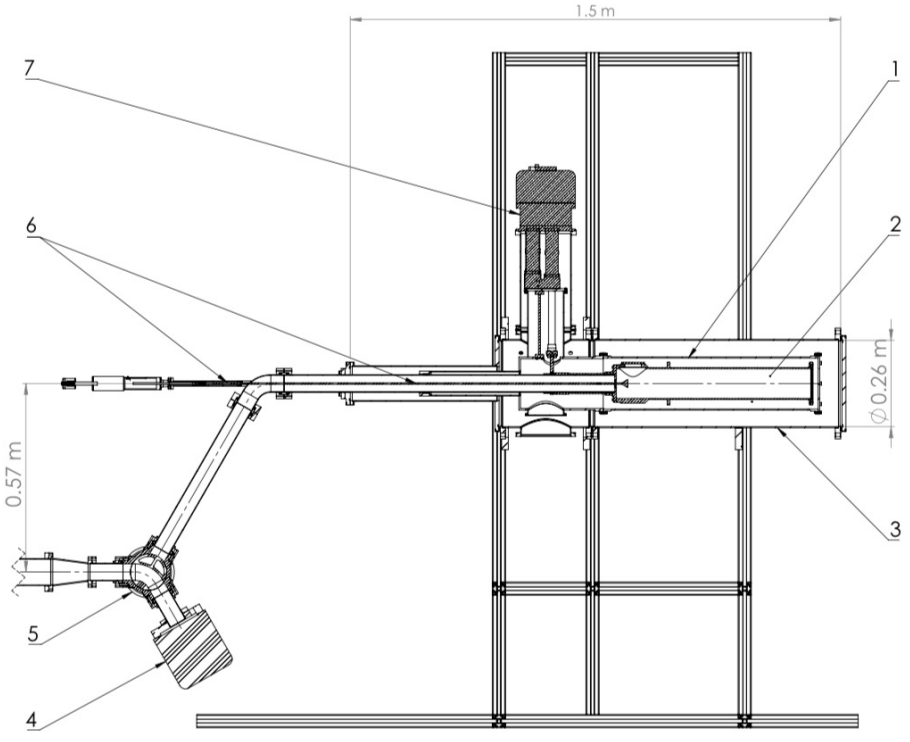


**(b)** left side cross section

**Figure 4.4.:** Design of the storage time measurement set-up. The vacuum vessel (3) is mounted in an aluminum profile assembly. The thermal shielding (1) is connected to the 40 K stage of the cold head (7). The neutrons from the turbine can be guided upwards by rotating the switch (5) and are directed by a 60° bend into the storage bottle (2), attached to the 5 K stage of the cold head. The bottle is sealed by a plug connected via a rod to a pneumatic cylinder (6). The stored neutrons are counted with a $^3$He detector, after turning the switch into the emptying position and opening the bottle.

and increasing loss rate for a worst case approximation by roughly 10 %, as explained in section 4.3.4.
By raising, a velocity spectrum is provided that corresponds well to the expectations for what can be stored in a CYTOP coated container. Hence, a high fractional gain is achieved for neutrons with velocities below the optical potential of aluminum. The approximated spectrum maximum is roughly at the maximum velocity for total neutron reflection on CYTOP.

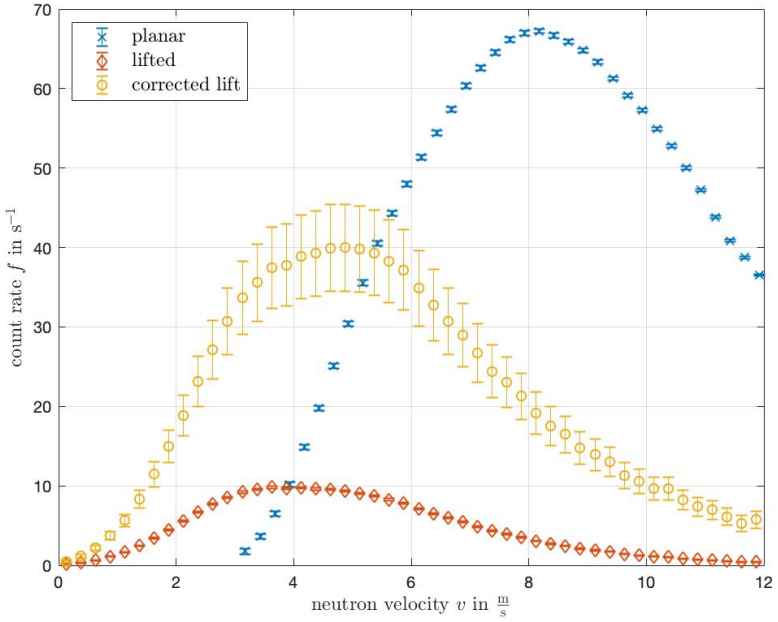


**Figure 4.5.:** Comparison of the uncorrected spectra after lifting (planar), measured with the vertical TOF set-up, to the initial neutron spectra (lifted) measured with the horizontal TOF set-up. The o indicate spectrum corrected the with transmission of the bends and guides. For the losses due to the closing mechanism aperture a constant loss of 10 % is estimated.

### 4.3.2. Vacuum vessel

The vacuum vessel consists of four parts: the central, reduction, cold head and storage bottle vessel. The design is chosen to minimize the pumping volume while enabling high flexibility of dimensions for the investigated storage volume. The vacuum pumping of the vessel is done with a turbo pump from Oerlikon /Turbovac 450iX) connected on the horizontal KF150 flanges of the central part. The guide is pumped with a separate turbo pump connected by KF25 flanges at the switch and directly after the aluminum separation foil and its vacuum is measured separately at the switch. The pressure of the vacuum vessel is measured at a KF40 flange on the central part. With both pumps connected, a vacuum at the lower $10^{-6}$ mbar regime is reached at the vessel the upper $10^{-6}$ mbar is reached at the guide. This pressure difference leads a direction of particles inside the vacuum towards the storage bottle leading to a possible contamination of the storage bottle vacuum and walls. Therefore, a small hole in the one meter guide is foreseen on the left side of the cold head mount, providing a vacuum 'sink' at the coldest point. This may reduce ballistic trajectories in this pressure regime of particles towards the bottle.

### 4.3.3. Cryogenic Environment

According to the improved storage time performance by cooling to low temperatures [35] and need for testing new materials at low temperatures before putting them in a superthermal source, a cryogenic system is added to the set up. The cryo cooling is done by the cold head RP-052A from Sumitomo connected to a SRP-052A cryocooler. The 5 K stage of the cold head is connected to the one meter long UCN guide, which delivers neutrons to the bottle, roughly 100 mm before the storage bottle inlet. Thermal shielding is provided, reduce the thermal load on the 5 K stage, as detailed in figure 4.6. This is connected to the 40 K stage and also to the UCN guide by a M60 $\times$ 1.5 thread of copper soldered onto the UCN guide. This connection redirects a significant heat load from the 5 K stage. Hence, the guide is a direct temperature bridge from room temperature to the cold stage and the heat capacity far low temperatures. The M60 $\times$ 1.5 is to chosen guarantee a large contact area, and thermal contact is increased by applying a small amount of vacuum grease. The distances are set to a minimum by 1D-simulation of the heat transfer within the construction tool SolidWorks and an additional 10 % safety margin.

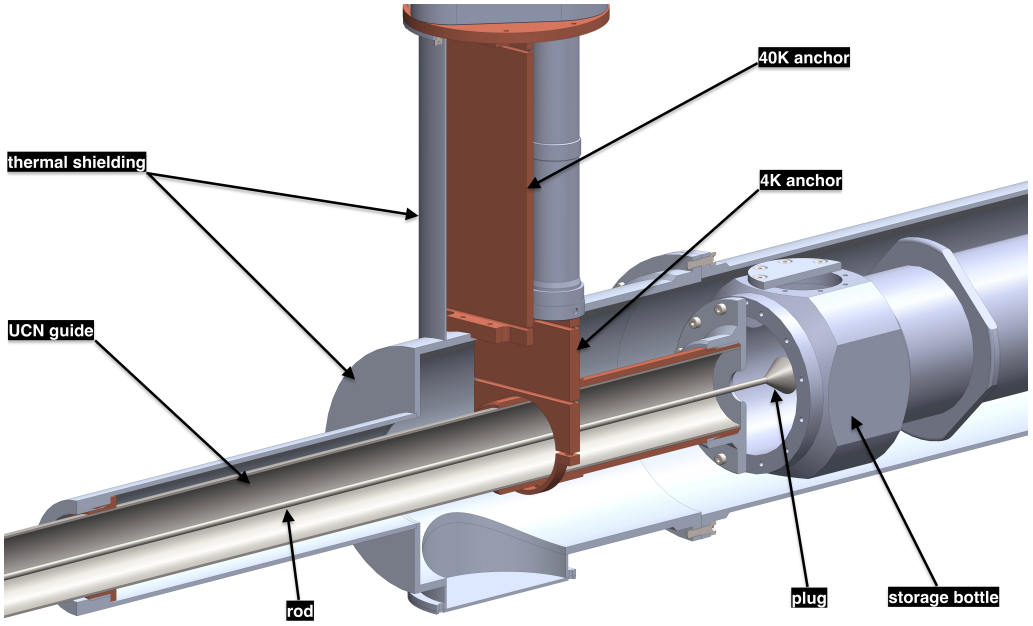


**Figure 4.6.:** Separated partial cross section of the cryogenic environment with the detailed opening/closing mechanism of the bottle

A huge temperature gradient occours along the guide, from ambient to cryogenic temperatures. Three fixed points provide anchors between room temperature to 40 K at the heat shield, and down to 5 K at the first stage. Thermal contraction of the bend might lead high shear stresses at the cold head, which could damage the cooling apparatus. Therefore, the elastic hinges at the 40 K and 4 K thermal anchors are designed to reduce any such stresses, while still bearing the full weight of the inner assembly and preserving a sufficient heat transfer area. The calculation to chose the dimensions is done according to the equations provided in [36], together with the rule of thumb for the elastic hinge parameter $\beta$ defining the functionality of the hinge with an elastic range between $0.01 < \beta < 0.5$, where the lower bound presents the minimum machineability and the upper the hinge functionality.

$$\beta = \frac{D}{2R} - 1 \tag{4.1}$$

Here$R$ is the radius and $D$ the minimum distance between the centers of the corresponding circles. To find an optimum between the given boundaries, the minimum heat transfer area is identified by solving the one dimensional heat transfer equation while respecting the variable heat capacity of copper towards cryogenic temperatures and simulating the maximum applicable lateral forces within SolidWorks. The final dimensions are given in figure 4.7 with a hinge functionality of $\beta = 0.3$. In order to reduce the lift effect by bending of the anchor hinges, the distance between them is set as large as possible.

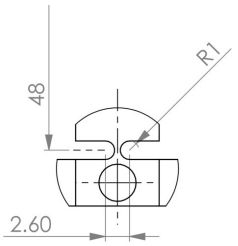


**Figure 4.7.:** Detail drawing of a hinge from the thermal anchors.

### 4.3.4. Closing Mechanism

The design of the closing mechanism is chosen on geometrical considerations of the whole storage assembly (see fig. 4.6). Opening towards the inside of the bottle fulfills two functions: On the one hand any unnecessary barrier to neutrons before the bottle is avoided during filling, and on the other hand, the tapered shape of the plug opening inwards automatically directs a stored neutron towards the outside. The combination of the radius at the flange and the tapered plug create a thin contact zone. The taper of the plug is chosen with respect to the radius of its counterpart to direct neutrons away from the sealing ring during storage (see. fig. 4.8).

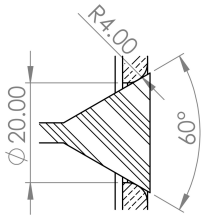


**Figure 4.8.:** Detail drawing of the storage bottle sealing mechanism.

However, a main concern is how to steer any closing mechanism with simple mechanics while occupying only a small spatial area.The opening and closing is actuated by a ⌀4 mm stainless steel rod along the guide's central axis, fed through a small hole at the center of the 60° bend. Since adding such a rod inside a guide might have a significant effect on the neutron transmission, an estimation of the additional loss due to the reduced mean free path is made. The fraction of the additional added surface cross section to the cross section of the UCN guide is taken giving an factor of 8 %, which seems quite reasonable compared to its simplicity and performance. The rod is pneumatically driven outside the vacuum via a linear ultrahigh vacuum feedthrough from Tectra (L-2172-4-1D-SM) with a linear travel of 100 mm, and operated at a pressure maximum 8 bar pressure. The additional gap loss for guiding can be assumed as negligible according to [37], which concluded that for neutrons directly propagating toward a slit with the same dimensions as the radial gap (0.25 mm) almost 80 % are reflected back. This means if 10 % of all neutrons are directed to the gap only 2 % are lost. This is rather low in comparison to the transmission loss of the bend, i.e. 30 % at the maximum total reflection velocity for CYTOP of 4.7 $\frac{\mathrm{m}}{\mathrm{s}}$.

## 4.4. Cooling Test

In order to test the adhesion of the coated CYTOP at cryogenic temperatures and to verify the function of the designed hinges at the thermal anchors (see sec. 4.3.3) a cooling test was conducted. The temperature is measured with a cernox sensor X49051, installed at one of the tapped holes on the inlet flange side.
For the test the center part and the cold head thermal screens were packed in super insulation foil to minimize the heat load on the cold head. The cool down curve is depicted in figure 4.9, where the minimum temperature 27 K at the inlet is reached after 15 hours cooling time. The difference of the measured of 22 K to the minimum achievable temperature with the cold head can be explained by the temperature dependence of the coolable heat load power of the first and second stage, which decreases towards lower values. Since there is no thermal barrier between the blind flanged end of the UCN guide, an area of 20 cm at room temperature is directly exposed on the UCN inlet. This leads to a maximum additional irradiated power of 0.8 W on the 5 K stage. Also the thermal shield of the storage bottle is not wrapped in superinsulation foil, which leads to a higher heat load on the thermal shield.
However, the achieved temperature of the bottle is already far below the freezing temperature liquid fluoromers which tend to crumble and crack [22, 38]. The bottle is disassembled to check the coated surface for any defects. Examining the inlet flange and the interior of the bottle by eye, no defects at the surface or peeling off is visible. Pictures of the interior of the bottle after the cooling test are provided in the appendix C.
Also the examination of the cryogenic assembly shows no damage on the thermal anchors or any other part, verifying the functionality of the hinges.
This first result provides a strong hint that CYTOP could be used for UCN measurements at cryogenic temperatures, and confirms general functionality of the cryogenic components of the storage time set-up. Lower temperatures could be achieved by a better insulation of the thermal shielding and installation of a thermal block in the neutron delivery guide.

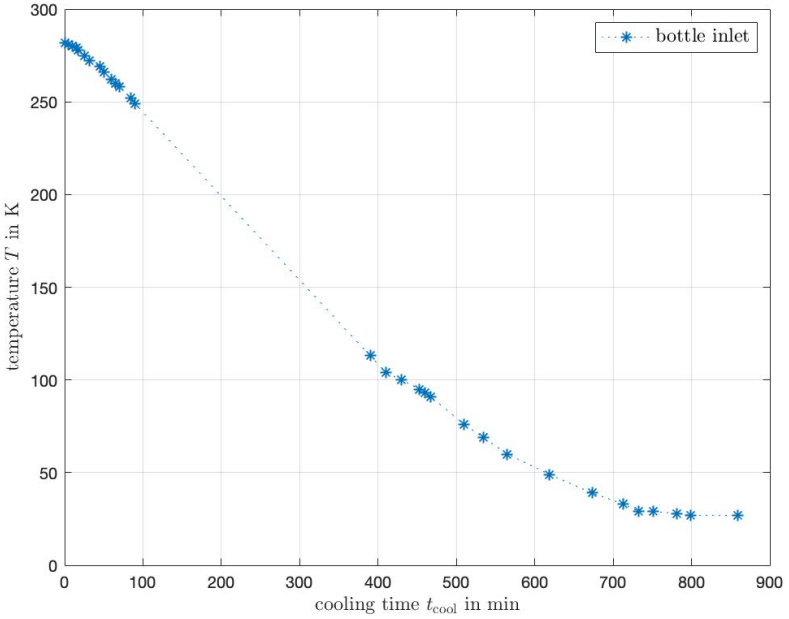


**Figure 4.9.:** Cooling curve of the conducted cooling test of the storage time set-up. The curve of the temperature sensor depict the temperature at the inlet of the storage bottle.

## 4.5. Procedure of the Storage Time Measurement

The storage time measurement set-up was fully assembled for the first time at the TES beam line of PF2 at the ILL (see fig. 4.10).

### 4.5.1. Experimental Procedure

In order to measure the storage time neutrons need to be stored for different total times inside the bottle in order that the remaining neutrons can be counted for each sampled time. By additionally measuring the arrival time for each neutron after storage, an emptying curve is obtained. Therefore, at a stable experimental procedure is needed which can be repeated without any differences influencing the measurement. In the following the procedure for the storage time measurements with the set-up described above is presented. The measurements for the CYTOP coated storage bottle at room temperature are are performed and evaluated at the PF2 TES beam line.

1. **Filling:** The switch is moved to the filling position, connecting the initially closed bottle with the guide from the turbine. The UCN guide is prefilled with neutrons. After a few seconds the storage bottle is opened by pushing the plug into the bottle with the pneumatic feedthrough. Due to the limited remaining measurement time no build up curves could be measured and the filling time $t_{\text{fill}}$ is approximated to:

$$t_{\text{fill}} = 60\,\text{s}$$

2. **Storing** After the filling time is reached, the bottle is sealed by pulling the plug into its seat. Afterwards the switch is turned to the emptying position, connecting the guide with the $^3$He detector, to empty the UCN in the guide. Except for the first measurement time 15 s, the storage time is varied in 30 s steps up to 120 s giving the following storage times

$$t_{\text{store}} = 15, 30, 60, 90 \text{ and } 120\,\text{s}$$

3. **Emptying:** After the storage time is over, the bottle is opened again by pushing the plug with the pneumatic feedthrough into the bottle. The neutrons propagate towards the detector. Immediately after opening the bottle the counts are measured at the detector, where each data point integrates the counts received during a five-second window. This in addition provides a time-resolved emptying curve for each storage time measurement. An example raw storage curve for 30 s storage time is depicted in figure 4.11.

Despite the limited available measurement time at the TES beam, the procedure was performed at least twice for each storage time, minimizing the statistical error, which arise from Poisson statistics ($\Delta N = \sqrt{N}$).

### 4.5.2. Data Processing

A major issue for data treatment is the changing background at the detector due to the movement of the turbine output guides, which changes its position between EDM, UCN and MAM beam lines every three to four minutes. If this changing background were not taken into account, it could influence the measured effective lifetime. Therefore, background measurements for each position were conducted, which revealed two major different background levels.

$$BG_{\text{low}} = (3.7 \pm 0.2)\,\text{Hz}$$
$$BG_{\text{high}} = (6.0 \pm 0.3)\,\text{Hz}$$

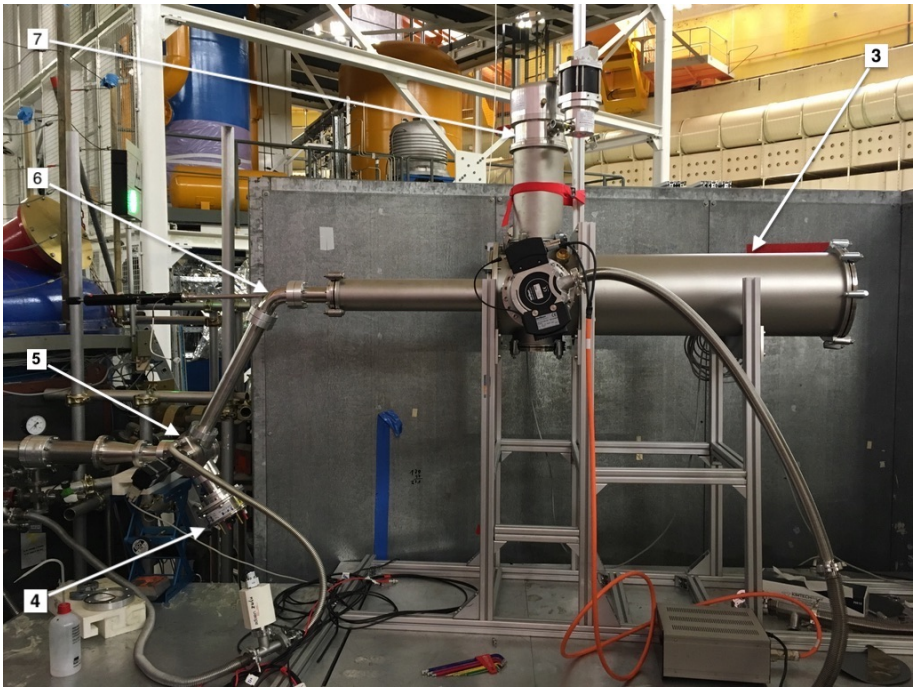


**(a)** Side view of the assembly

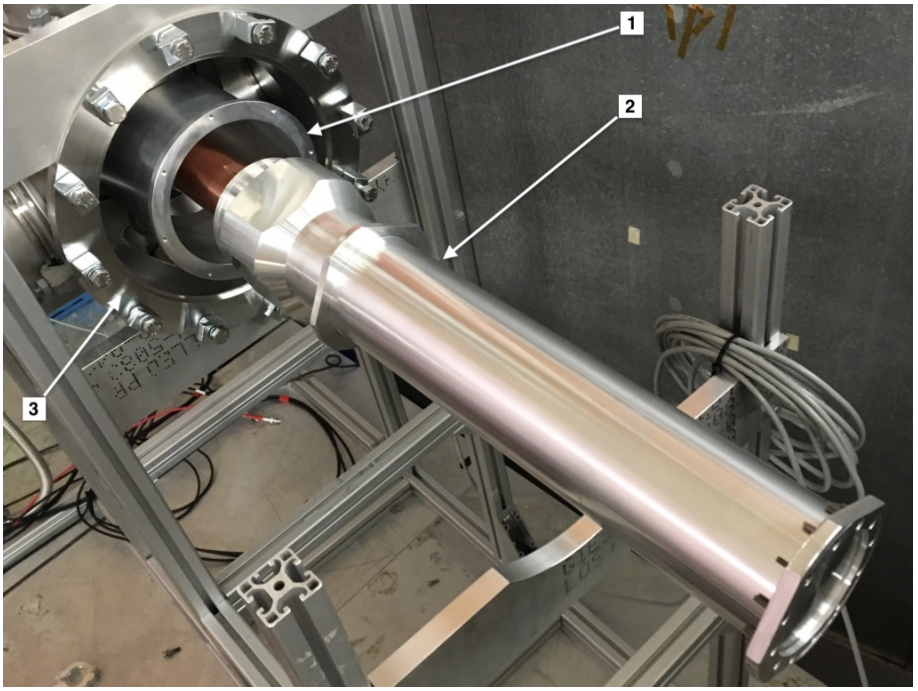


**(b)** Detail of the mounted bottle.

**Figure 4.10.:** Pictures of the storage time set-up assembled at the PF2 TES beam line. In (a) the vacuum vessel (1) is assembled in the aluminum frame with the cold head (7) attached on top. The neutrons are delivered through the NiMo coated switch (5) with the $^3$He detector (4) attached. (6) indicates the 60° bend with the plug closing mechanism. In (b) a detail view the bottle with dismounted vacuum vessel is given. The aluminum bottle (2) screwed onto the neutron guide is clearly visible and (3) marks the central part of the thermal shielding.

Comparing the background at the detector to the leakage rate of the NiMo coated switch, it appears our times higher than expected. An explanation could be the less than one meter distance to the turbine of the unshielded detector, resulting in a $r^{-2}$ higher background of neutrons passing the aluminum detector flange.
However, enabling a proper background treatment is possible since the moment of the changing turbine positions, indicated by the pneumatic valve actuation, was marked in the data. The appropriate background is then subtracted respectively in analysis (see fig. 4.11). Due to the neutron velocity distribution at the bottle and the 1.6 m distance between the bottle and the detectro a short delay time of the arriving neutrons can be seen, leading to a count increase from the first to the second data point. Additionally the emptying curve is fitted with an exponential function verifying the expected decay behavior. After the background treatment, the average for each storage time is taken by weighting each time bin with its inverse squared error (see eq. (3.3)) while the average inverse errors are calculated by the sum of the inverse squared errors (see eq. (3.4)).

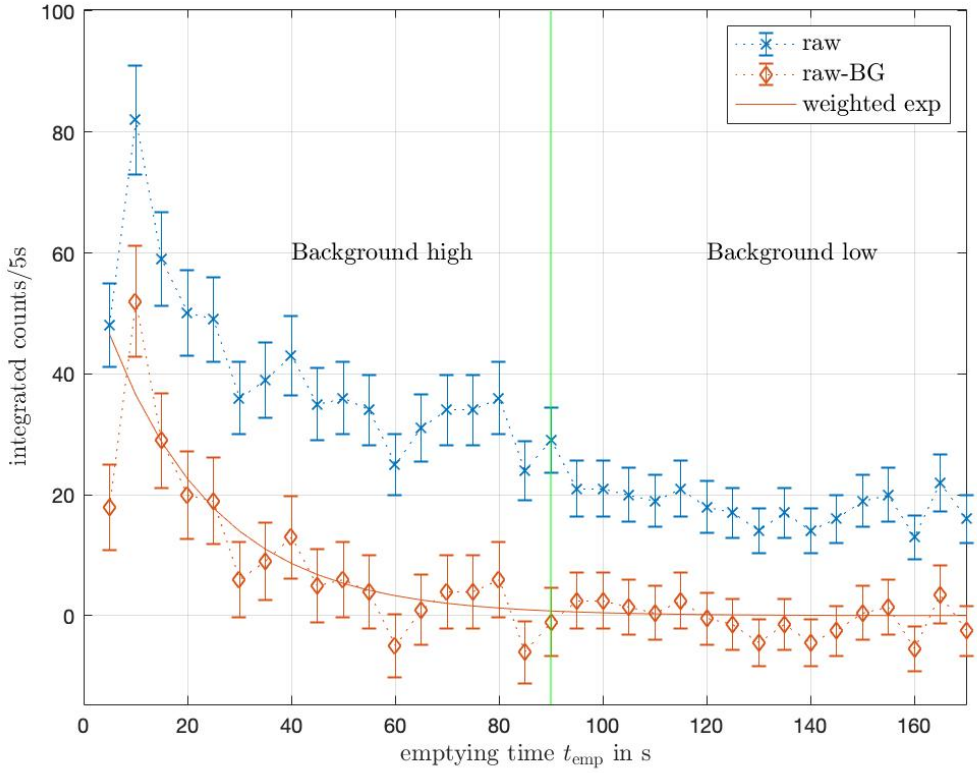


**Figure 4.11.:** Data processing example for an emptying curve at a storage time of 30 s. Each section of the raw data has the appropriate background (low/high) subtracted , depending on the turbine position. The vertical green line indicates a transition between the two different background states during the measurement. A weighted exponential decay is fitted to the processed data showing the exponential decay, where the error bars arise from Poisson statistics.

## 4.5.3. Results and Evaluation

### 4.5.3.1. Determination of the storage life time

The processed counts data set for each storage time are integrated over a 60 s emptying time and plotted against storage time in figure 4.12. The integration time is defined by use of as many counts as possible for the short storage time, while minimizing the possible influence

of the background for long storage times with low count rates. To determine the effective lifetime $\tau_{\text{eff}}$ and the initial number of UCNs $n_0$ confined in the bottle an exponential fit is applied, weighted with the inverse squared errors. The fit results are given in table 4.2.

$$n(t) = n_0 \cdot e^{t/\tau_{\text{eff}}} \tag{4.2}$$

Contrary to certain previous experiments [8, 19], a simple exponential decay is chosen for fitting due to the small set of data points. A double exponential could lead to over fitting, and in addition, no clear trend to a double exponential is visible. This divides the neutron velocity spectrum into a 'faster' and 'slower' part in the emptying curves. The 95 % confident bounds from the fit are shown in figure 4.12, determined by calculating the confidence interval at each fitted point and interpolating between the them.
A variation of the integration time of counting for 30 s and 45 s are within the errors of the determined effective lifetime in good agreement. The corresponding graphs and an additional table with the fit results are provided in the appendix D.2.

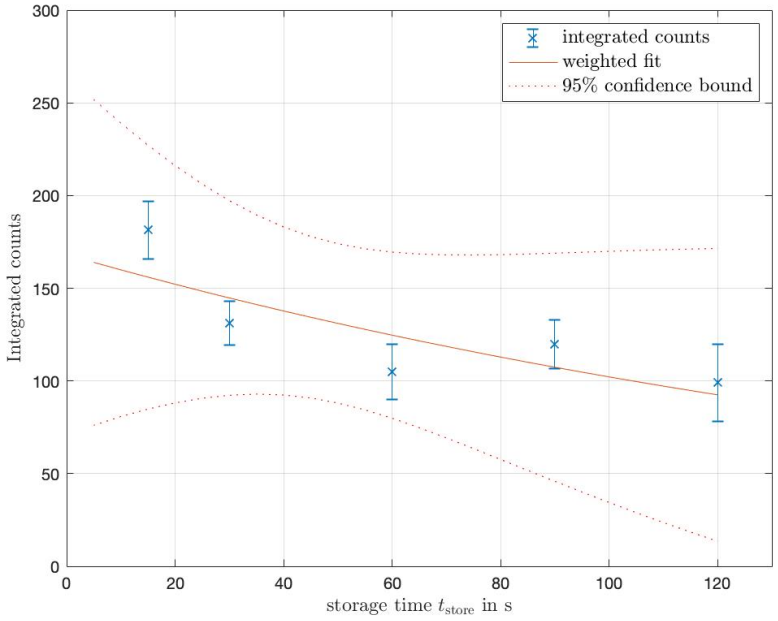


**Figure 4.12.:** Storage curve for the CYTOP coated storage bottle at room temperature. The data points are given by the over 60 s integrated counts for the averaged emptying curves for each storage time. To show the exponential decay behavior, the data is fitted with an exponential function, where the weights are the inverse square of the error for each data point.

**Table 4.2.:** Parameters of the exponential decay fit for the storage curve of the CYTOP coated storage bottle.

| | | |
|---|---|---|
| effective storage time | $\tau_{\text{eff}}$ | $(200 \pm 98)$ s |
| inital UCN number | $n_0$ | $168 \pm 22$ |
| goodness of fit | $\chi^2_{\text{dof}}$ | 2.3 |

Calculating the effective lifetime due to wall losses $\tau_{\text{wall}}$, according to (2.23) the neutron $\beta$-decay of $(779.5 \pm 0.8)$ s [5] and losses due to gaps $\tau_{\text{wall}}$ have to be considered. The gap losses are reduced by coating the assembled bottle. Since for the mounting of the plug the

inlet flange has to be dismounted, the CYTOP sealing is broken. This leads to a possible gap between the body and the flange. An approximation of the in the worst case occurring gaps is done by calculating the length of the edges of the connected surfaces exposed on the inside $l_{gaps} = 289\,\mathrm{mm}$ and multiplying with the average roughness depth for the uncoated components $R_z < 1.6\,\mu\mathrm{m}$ giving a maximum summed up gap of is $0.44\,\mathrm{mm}^2$, which is quite small compared to the inner surface of the bottle ($A_{\mathrm{bottle}} = 0.18\,\mathrm{m}^2$). Additionally, the chosen geometries of flange connection with a long radial contact surface and the design of the plug pushed in a convex formed seat give no direct escape possibility, meaning that a neutron reaches the gap has to be reflected several times before being able to leaf the confinement. Therefore, they have a far higher probability of being reflected back into the bottle than leaving [37] and thus the losses by gaps can be assumed as negligible and the wall loss is given by

$$\tau_{\mathrm{wall}} = (259 \pm 65)\,\mathrm{s}$$

#### 4.5.3.2. Calculation of the loss probability per bounce

Since the storage time strongly time depends on the geometry of the bottle no figure of merit is given to make a comparison with other tested materials in different confinements. Therefore, the loss per pounce probability is calculated to evaluate the velocity dependent storage properties of the tested material. It can be derived for each material by solving equation (2.24) for $\overline{\mu}$ and using the experimentally measured effective storage time $\tau_{eff}$. By using the optical potential of CYTOP 116 neV, corresponding to a maximum velocity of $4.7\,\frac{\mathrm{m}}{\mathrm{s}}$, an average loss per bounce probability of

$$\overline{\mu} = (9 \pm 4) \times 10^{-5}$$

is obtained. According to equation (2.15) this corresponds to a loss per bounce of

$$\overline{\eta} = (3 \pm 1) \times 10^{-5}$$

Comparing this result with the theoretical value in section 4.2 calculated, it is more than two orders of magnitude larger. This might be caused by several effects:

- **Gap losses:** The gap might be bigger than assumed, since the pneumatic closing mechanism, pushing the plug into the seat, due to malfunction could not be used. Therefore, it had to be pushed manually leading occasionally to a greater gaps. Also the loss probability for the assumed gaps could be higher for the given sizes.
- **Temperature dependence:** As already shown for other coatings the storage time depends on the temperature of the wall materials. Thus a test at room temperature leads inevitably to a higher loss rate per bounce.
- **Thin film quality:** The quality and thickness of the thin film could not be observed without destruction of the coating. Thus in the unlikely worst case at the center of the flanges the surface thickness could be event thinner than the assumed 15 µm.

## 4.6. Conclusion and Comparison to Previous Measurements

Within this chapter a newly constructed versatile storage time set-up was presented, enabling storage time experiments ambient and cryogenic temperatures. This system is based on the characterized handling system from chapter 3, including a three way neutron switch to enable emptying and filling the storage bottle through one aperture. A first storage time measurement with the commissioned set-up was performed for a bottle with the same dimensions as used at SUN II. For the first time the water repelling fluoropolymer CYTOPl could be successfully tested as wall material. It was coated via a dip coating process onto the inner walls of the storage bottle, using the oven presented in [33] in order to transform the coated amorphous CYTOP to its glassy phase.
Comparing the calculated loss parameter with the values for Fomblin oil and grease $1.8 \times 10^{-5}$ & $2.4 \times 10^{-5}$ [39] and Be $4 \times 10^{-5}$ [22] at room temperature, the experimental result is in good agreement, with a mean value of $(3 \pm 1) \times 10^{-5}$ already below the experimental loss rate for Be at 6.5 K [22]. The higher value than Fomblin could be cuased due to the breaking of the sealing for mounting of the plug or larger gaps. This may have not been aligned as previously leading to small gaps where neutrons can pass. Another reason could be the mechanical sealing, due to malfunction of the pneumatic closing mechanism it had to be driven manually. This might have led to increasing gap losses during storage. A less likely reason for the low storage time could be a non uniform coating with some residual uncoated areas due to the dip coating process.
Since the tested storage volume has similar dimensions to the production volumes used at SUN II a direct comparison of the effective lifetime and loss rate can be done. The lifetime for the BeO vessel in SUN I ($A = 0.3\,\mathrm{m}$, $V = 5\,\mathrm{l}$, $\bar{l} = 7\,\mathrm{cm}$) was measured during operation at cryogenic temperatures [8]. The emptying curves are fitted with a double exponential leading to $\tau_{\mathrm{slow}} = (132 \pm 2)\,\mathrm{s}$ [6] and $\tau_{\mathrm{fast}} = (43 \pm 3)\,\mathrm{s}$. For SUN II a storage time of $\tau_{\mathrm{eff}} \approx 200\,\mathrm{s}$ was determined, which is coated with a Be thin layer and a special thin Fomblin grease mixture. This shows that within the error of the measured lifetime in CYTOP $\tau_{\mathrm{eff}} = (200 \pm 98)\,\mathrm{s}$, even at room temperature equal or even higher storage times may be achieved. Thus, due to the temperature dependence of the storage behavior [35], at cryogenic temperatures higher effective lifetime may be possible. During the conducted cooling test to 27 K with the storage time set-up with the mounted bottle, no crumbling or cracking of the thin film coating is visible, contrary to most kinds of Fomblin. This strengthens the case for CYTOP as coating material for superthermal sources at cryogenic temperatures. However, to give a final statement on the performance of the coating, further tests with and without neutrons must be conducted. These include as a verification of the optical potential of the coating and its thickness, as well as further storage time measurement with higher precision at ambient and cryogenic temperatures.

# 5. Summary and Outlook

## 5.1. Summary

In this thesis two main issues are addressed, both of which aim to improve the delivered UCN density provided to experiments by superthermal sources. First, the transportation efficiency for UCN in a ∅50 mm neutron handling system was examined, as well as methods to improve it. Second, to assist in the development of new and improved coatings for the converter vessel, a newly designed system for measurements of storage time constants was commissioned. A first measurement was conduced for a storage bottle coated with the fluoropolymer CYTOP, which was previously never tested with UCN.

The transmission of the individual components of neutron handling system was characterized with a horizontal TOF set-up, providing a one dimensional projection of the 3D velocity spectra of the transmitted neutrons. Since the spectra delivered by $^4$He sources can be far softer than the ones provided at PF2, the spectra were down-shifted by raising the experimental set-up. Obtaining velocity-resolved information for neutrons with energies below the optical potential of the aluminum separation foil of the detector, a method was introduced using the TOF set-up vertically.
With these measurements a proposed $1/v^2$ transmission dependence due to the surface roughness was demonstrated for an aluminum foil, which was measured first unpolished and again after polishing.
The transmission measurements of the ∅50 mm stainless steel guides reveal a velocity averaged transmission of $(89 \pm 3)\,\%$. To establish a reference point for the transmission of this new guide diameter, the averaged transmission of the commonly used ∅79 mm guides at the PF2 EDM beam line was defined to be $(92 \pm 2)\,\%$. Whereas, cleaning of one of these guides by hand, which has been used for several years, has already achieved a relative improvement in transmission by $(2.0 \pm 0.2)\,\%$.
Using horizontal TOF, the transmission of bent guide sections with a radius of 70 mm was measured, and are used to raise the experiment assembly for the storage time measurements.
The efficiency of the NiMo and Cu coated glass guides was measured with the vertical TOF set-up, revealing equal transmissions at the count rate maximum of $(82 \pm 1)\,\%$. For velocities below $5\,\frac{\mathrm{m}}{\mathrm{s}}$ NiMo has a $(2.3 \pm 0.4)\,\%$ higher transmission and for velocities above the count rate maximum a $(1.1 \pm 0.6)\,\%$ lower transmission than Cu. This characterization implies that the non-depolarizing Cu coating could be used instead of the NiMo coating for sufficiently slow UCN or short guides.

The transmission spectra for new designed three way rotary neutron switches was measured from $0\,\frac{\mathrm{m}}{\mathrm{s}}$ to $20\,\frac{\mathrm{m}}{\mathrm{s}}$ bu use of both kind of TOF set-ups. This kind of switch can be used to fill and empty the storage bottle through one aperture. One switch is uncoated, and the other one is coated with NiMo on the guiding surfaces and with Ti on the inner walls of the body and outer walls of the inlet. The uncoated switch shows similar transmission behavior to the

60° bend, which has the same radius of curvature. The leakage both switches is determined to $(4 \pm 2) \times 10^{-5}$ for the uncoated and $(0.6 \pm 0.2) \times 10^{-5}$ for the coated switch, which is already within and at the lower end of the leakage range of commonly used shutters.
In addition, with the characterized switch the relative detector efficiency of a boron 10 based cascade and $^{3}$He detector was determined to be $0.41 \pm 0.07$, which is in agreement with two other measurements conducted at PF2 [25, 26].

The designed storage time set-up enables determinations of the effective storage lifetime at ambient and cryogenic temperatures, to investigate the behavior of the wall materials in conditions similar to the environment in superthermal sources. Therefore, the bottle used here has similar dimensions to the one used at SUN II. This bottle has been dip-coated with the water repellent fluoropolymer CYTOP, which supposedly has similar characteristics 5o Fomblin. To provide a storable spectra, the characterized stainless steel guide elements and NiMo coated three way switch were assembled to sufficiently raise the experimental set-up. The storage time measurement conducted at ambient temperature reveals a promising effective lifetime of $(200 \pm 98)$ s. Since a conducted cooling test to 27 K did not reveal noticeable opticallly visible damage to the coating, equal or even higher storage times than so far achieved with a Fomblin coated bottle at SUN II may be possible at cryogenic temperatures.

## 5.2. Outlook

### 5.2.1. Neutron handling system

The transmission of all components with the horizonal and vertical TOF measurements and the components were adequate to perform the storage time measurements. However, optimization of the measurement technique and further steps to improve the quality of the components and analysis could be taken.

- **Surface roughness:** The surface polishing of the guides could be further automated, and for the separation foils it could be conducted at automated table polishing machines to get reproduceable surfaces. Also the roughness could be determined with other optical methods to identify any correlation lengths corresponding to micro roughness.
- **Simulations:** The obtained measurements could be used to compare the results of simulation models to reality, while further simulations could be run to help find optimum parameters.
- **Switch:** To further improve the performance of the switch the repositioning of the insert could be made more reproducable by usage of a zero play feedthrough. In addition, to avoid the first manual positioning an initial position marker should be added. Also the leakage could be optimized by improving the Ti coating and geometry. Since the design of the switch is scaleable, it could be used for any guide width. Also for future rotary switch designs the transmission might be improved by increasing the radius of the curvature.
- **Vertical TOF:** With the measured spectra of lifted set-up and bends using the horizontal and the vertical TOF , a model could be developed to recalculate the reshaped spectra at lower velocities.

### 5.2.2. Storage Time Measurement

#### CYTOP coating

The successful conducted storage time measurements and cooling test, strongly hint that CYTOP may be usable in superthermal sources. In order to verify this outcome and strengthen it further measurements and steps should be taken:

- **Coating Process:** To achieve a constant defined surface thickness, a higher degree of automation of the process is recommended, including the usage of a wobbling aperture. This means an excentric rotation along the bottle axis to coat all surfaces equally with sufficient waiting time and with defined baking temperatures between two successive coatings.
- **Optical Potential** Due to time constraints in this thesis, no additional measurements was conducted to verify the calculated optical potential. This could be done for example with neutron reflectometry measuring the scattering length density. Also the thickness of the coating should be measured using other non destructive methods such as optical ellipsomentry.
- **Thermal cycling:** Thermal cycling from ambient to cryogenic temperatures should be conducted to test the resistance of the coating to thermal stresses, simulating several cycles at a UCN source.

### Storage time set-up

Up to now only a storage time measurement at room temperature with relatively low count rates was conducted. This already provides a promising effective lifetime of $(200 \pm 98)$ s. To verify the performance of the CYTOP coating, the experiment should be repeated with longer storage times at more powerful beam lines at ambient and at cryogenic temperatures. In addition, with longer measurements one could investigate if the performance of the assembly degrades over time, as observed at superthermal sources.
With the this set-up, a wide variety of geometries and wall materials for UCN storage can be tested. However, the experimental results so far obtained and the performance of the set-up could be further improved:

- **Filling time:** The filling time should be measured with a Y-piece (or second switch), to determine when equilibrium is achieved.
- **Multilayer coating:** Storage time measurements have shown an increased storage time for walls coated with a thin layer with high optical potential and Fomblin on top. This could be also done for CYTOP, by measuring a storage volume uncoated, then coated with the high potential wall material, and again with CYTOP coated on top.
- **Different coatings:** A wide range of different coatings such as dPE and DLC could be tested at bottles with simpler geometry to compare their storage performance directly.
- **Shape independence** Due to the versatility of the set-up a wide geometrical range of storage bottles could be investigated, including for example those where gravity limits the mean free path.
- **Thermal shielding:** Since the cooling test reached only 27 K, measures should be taken to reach lower temperatures. This includes wrapping the whole thermal shielding with several layers of superinsulation foil. Also thermal stops could be placed in the UCN delivery guide, avoiding radiative heating directly at the bottle entrance. Since those block the propagation of neutrons in and out the bottle, an optimum between minimizing the radiation and blocking has to be found.
- **Heating:** According to [40] the effective lifetime is increased by previously heating. Therefore in addition to the cooling, a heating system for the storage bottle should be added.

If these further tests with higher precision at ambient and cryogenic temperatures confirm the first experimental results of this thesis, they could be further verified with desired UCN spectrum by measuring at a $^4$He source in 'fill and empty' mode.

# Appendix

## A. ReactorPower Change

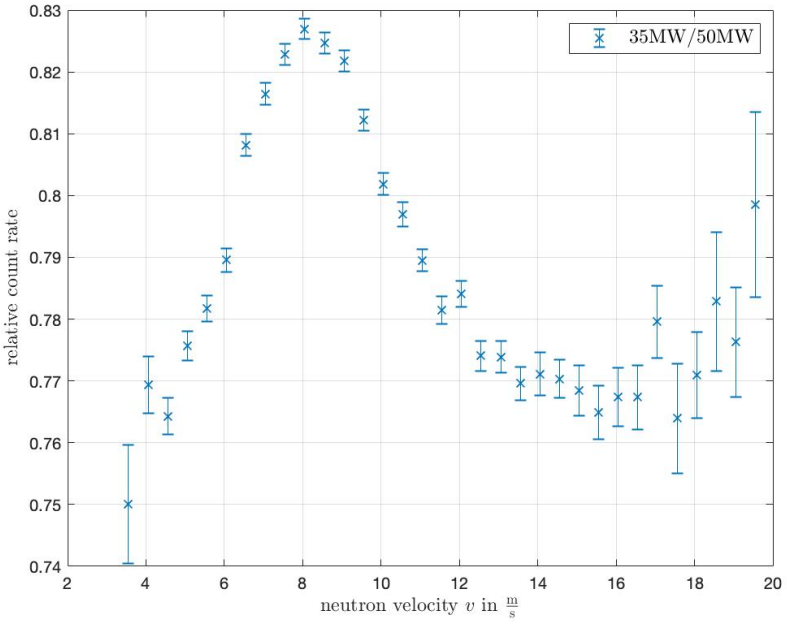


**Figure A.1.:** Relative velocity dependent count rate between the power change from 50 to 35 MW, leading to a 20 % depression of the integrated count rate.

## B. Transmission Inox Guides

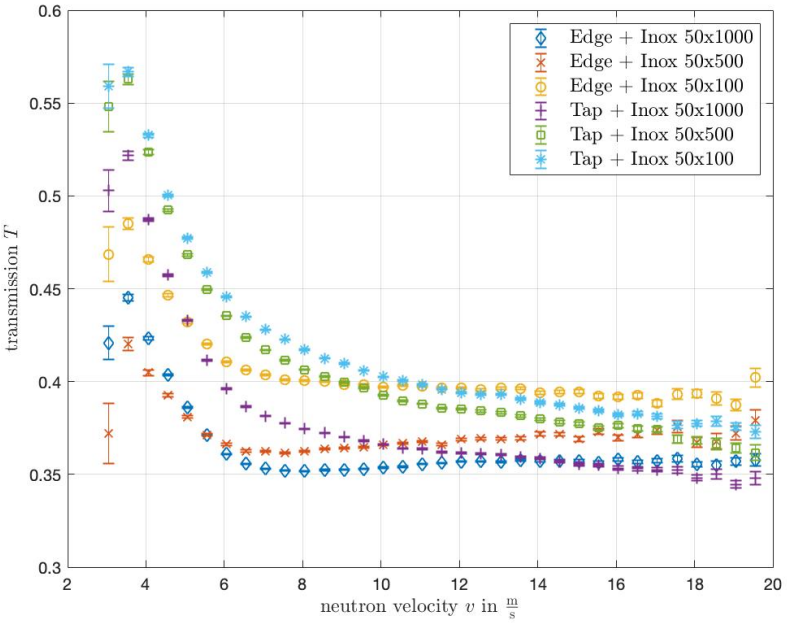


**Figure B.2.:** Transmission of the different ∅50 mm stainless steel guide lengths using the tapered and hard edged reduction. The length units of the labels are in millimeter.

## C. Pictures of the interior of the Bottle

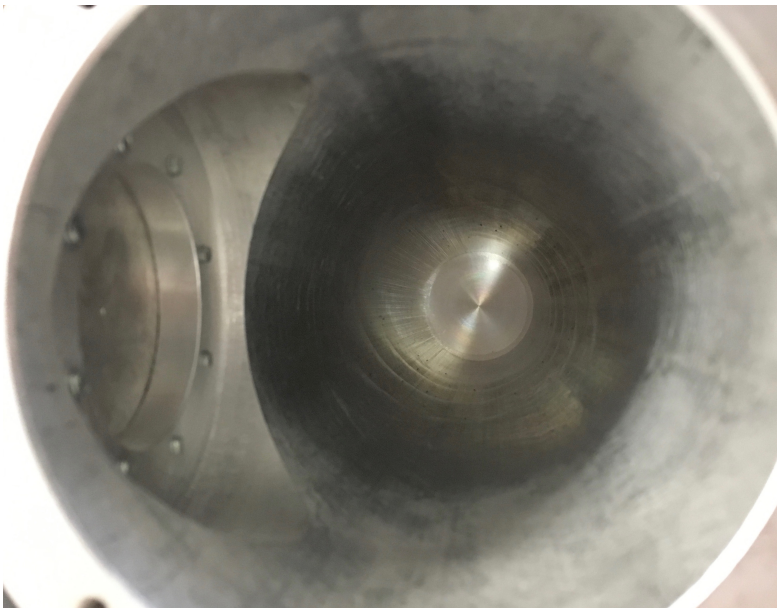

**(a)** Body

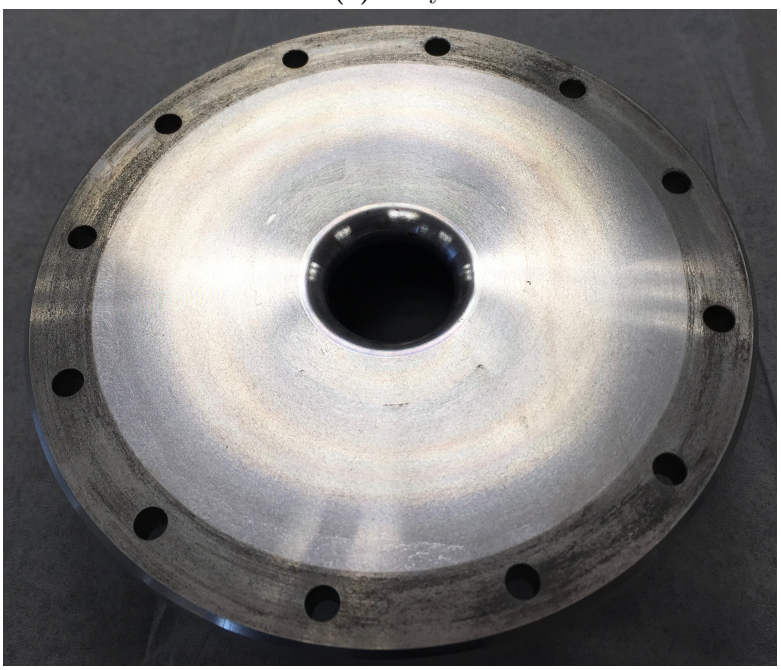

**(b)** Inlet flange

**Figure C.3.:** Pictures of the bottle interior after the cool down to 27 K. The coated surface still appear unchanged with no crumbling or cracking visible.

# D. Storage Time Data

## D.1. Empty Curves

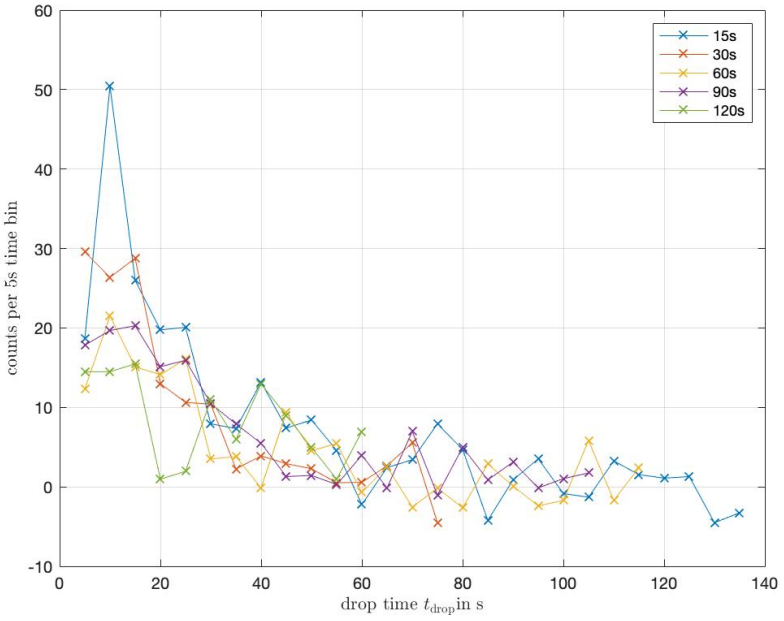


**Figure D.4.:** Overlapping averaged emptying curves plotted against the time $t_{\mathrm{drop}}$ it took the neutrons propagating form the bottle to the detector for all storage times.

## D.2. Storage Curves

**Table D.1.:** Parameters of the exponential fit presented in equation (4.2) for alternative emptying time intervals, leading to different integrated count sums for each data point. The data points are weighted with the squared inverse errors for the storage curve of the CYTOP coated storage bottle.

| integrated empty times | $t_{\mathrm{empty}}$ | 45 s | 30 s |
|---|---|---|---|
| effective storage time | $\tau_{\mathrm{eff}}$ | $(182 \pm 79)$ s | $(153 \pm 51)$ s |
| initial UCN number | $n_0$ | $163 \pm 21$ | $148 \pm 17$ |
| goodness of fit | $\chi^2_{\mathrm{dof}}$ | 2.4 | 2.1 |

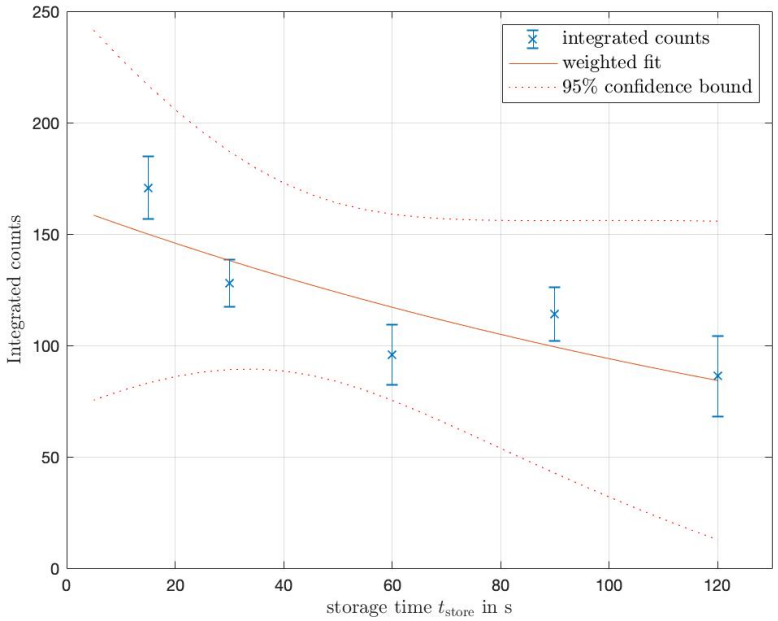


**(a)** 45 s emptying time

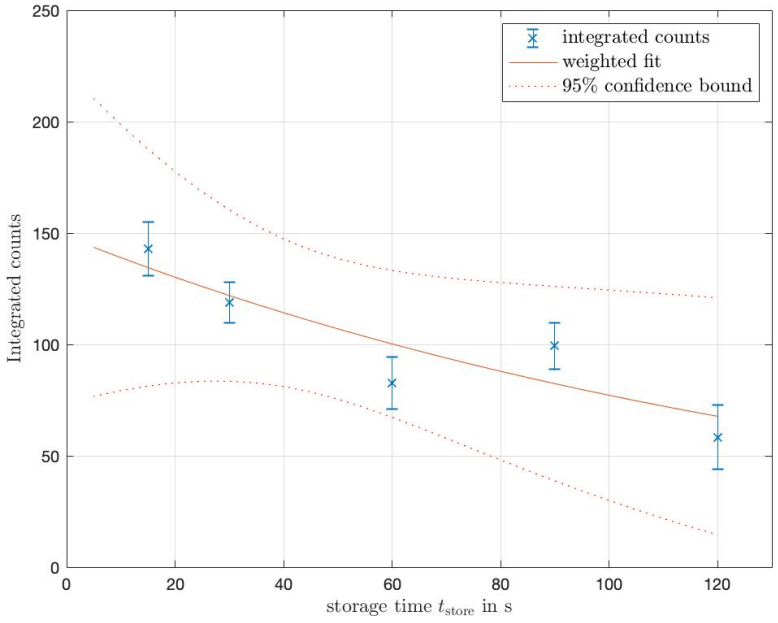


**(b)** 30 s emptying time

**Figure D.5.:** Storage curve for the CYTOP coated storage bottle at room temperature. The integrated counts in each plot are for a given defined emptying time intervals for the averaged emptying curves of each storage time. The data is fitted with an exponential function (see (4.2). The fit is weighted with by the inverse square of the error for each data point.

# List of Figures

# List of Tables

# Bibliography


[1] ESS: *European Spallation Source*, 2018. https://europeanspallationsource.se.

[2] Langevin, Institut Laue: *Ultracold neutron facility PF2*, 2018. https://www.ill.eu/users/instruments/instruments-list/pf2/description/instrument-layout/.

[3] Steyerl, A: *A "neutron turbine" as an efficient source of ultracold neutrons.* Nuclear Instruments and Methods, 125:461–469, März 1975. https://doi.org/10.1016/0029-554X(75)90265-7.

[4] Steyerl, A, H Nagel, F. X Schreiber, K. A Steinhauser, Roland Gahler, W Gläser, P Ageron, J.M. Astruc, W Drexel, G Gervais und W Mampe: *A new source of cold and ultracold neutrons.* Physics Letters A, 116:347–352, Juni 1986.

[5] Neutron lifetime, dark matter und search for sterile neutrino: *A. P. Serebrov, R.M. Samoilov, I.A. Mitropolsky, A.M. Gagarsky.* arXiv:1802.06277 [nucl-ex], 2018.

[6] Zimmer, Oliver: *Performance of the upgraded ultracold neutrons at the Institut Laue-Langevin.* Private communication, 2018.

[7] Zimmer, Oliver, Florian M. Piegsa und Sergey N. Ivanov: *Superthermal Source of Ultracold Neutrons for Fundamental Physics Experiments.* Phys. Rev. Lett., 107:134801, Sep 2011.

[8] Piegsa, F. M., M. Fertl, S. N. Ivanov, M. Kreuz, K. K. H. Leung, P. Schmidt-Wellenburg, T. Soldner und O. Zimmer: *New source for ultracold neutrons at the Institut Laue-Langevin.* Phys. Rev. C, 90:015501, Jul 2014.

[9] R. Golub, D J Richardson und S. K. Lamoreaux: *Ultra-cold neutrons.* Reports on Progress in Physics, 42(3):439, 1979.

[10] K. Lamoreaux, S und R Golub: *Calculation of the ultracold neutron upscattering loss probability in fluid walled storage bottles using experimental measurements of the thermomechanical properties of Fomblin.* Physical Review C, 66, März 2002.

[11] K. Bodek, M. Daum, R. Henneck S. Heule M. Kasprzak K. Kirch A. Knecht M. Kurzniak B. Lauss M. Meier G. Petzoldt M. Schneider G. Zsigmond: *Storage of ultracold neutrons in high resistivity, non-magnetic materials with high Fermi potential.* Nuclear Instruments and Methods in Physics Research Section A: Accelerators, Spectrometers, Detectors and Associated Equipment, 597(2):222 – 226, 2008.

[12] Division, AGC Chemicals Fluoroproducts: *Coating Characteristics of CYTOP*, 2018.

[13] Golub, R. und J. M. Pendlebury: *Ultra-Cold Neutrons.* Hilger, 1991.

[14] Ignatovich, V.K.: *The Physics of Ultracold Neutrons.* Clarendon Press, Oxford, 1990.

[15] Abele, Hartmut: *The neutron. Its properties and basic interactions.* Progress in Particle and Nuclear Physics - PROG PART NUCL PHYS, 60:1–81, Januar 2008.

[16] Division, AGC Chemicals Fluoroproducts: *CYTOP technical brochure*, 2009.

[17] S. Heule, F. Atchison, M. Daum A. Foelske R. Henneck M. Kasprzak K. Kirch A. Knecht M. Kuzniak T. Lippert M. Meier A. Pichlmaier U. Straumann: *Diamond-like carbon coated ultracold neutron guides.* Applied Surface Science, 2007.

[18] Steyerl, A: *Effect of surface roughness on the total reflexion and transmission of slow neutrons.* Zeitschrift für Physik, 254:169–188, April 1972.

[19] Zechlau, T.: *Ultra-Cold Neutron Transport and Spin Manipulation System for the nEDM.* Dissertation, Technischen Universität München, 2016.

[20] Beringer, J. und Others: *Review of Particle Physics.* Phys. Rev. D, 86:010001, Jul 2012.

[21] Atchison, F, T Bryś, Manfred Daum, P Fierlinger, P Geltenbort, R Henneck, S Heule, Malgorzata Kasprzak, K Kirch, A Pichlmaier, C Plonka, U Straumann und C Wermelinger: *First storage of ultracold neutrons using foils coated with diamond-like carbon.* Physics Letters B, 625:19–25, Oktober 2005.

[22] Pokotilovski, Yuri: *UCN anomaly and the possibility for further decreasing neutron losses in traps.* Nuclear Instruments and Methods in Physics Research Section A-accelerators Spectrometers Detectors and Associated Equipment - NUCL INSTRUM METH PHYS RES A, 554:356–362, Dezember 2005.

[23] GmbH, Movatec: *Movatec Chopper*, 2018. `http://www.movatec.de/Engineering`.

[24] GmbH, Detector Technologies: *CDT CASCADE*, 2018. `http://n-cdt.com/products/cascade-detector-systems/`.

[25] Jenke, T.: *private communication*, 2018.

[26] Döge, Stefan: *Scattering of Ultracold Neutrons in Condensed Deuterium and on Material Surfaces.* PhD thesis, Technische Universität München, Munich, Germany, 2018.

[27] GmbH, Hoffmann: *Surface roughness measuring tool ST1 GARANT*, 2018. `https://www.hoffmann-group.com/GR/el/pangakis/Metrology/Microscopes,-surface-roughness-gauges/Surface-roughness-measuring-tool-ST1-GARANT/p/499030`.

[28] Wautischer, Gregor: *Realisation of Quantum Transport Measurements with UCNs within the qBounce Project*, 2015.

[29] Gomeringer, R., M. Heinzler, R. Kilgus, V. Menges, S. Oesterle, F. Wieneke, T. Rapp, C. Scholer, A. Stenzel und A. Stephan: *Tabellenbuch Metall: mit Formelsammlung.* Europa-Fachbuchreihe für Metallberufe. Europa Lehrmittel Verlag, 2017, ISBN 9783808517277.

[30] Babin, L.: *thesis.* Dissertation, Universite Grenoble Alpes, 2019.

[31] *Stepper Motor Controllers/Drivers Operator's Manual.*

[32] Lauer, T.: *private communication*, 2018.

[33] Windmayer, Dominik: *Using Deuterated Polyethylene Coatings for Manipulating Ultra-Cold-Neutrons in Different Applications*, 2016.

[34] A. J. Dianoux, G. Lander: *Neutron data bocklet*, 2003.

[35] Arzumanov, Semen, L N. Bondarenko, V I. Morozov, Yu N. Panin und P Geltenbort: *Storage of Ultracold Neutrons in Vessels Whose Walls are Made from Graphite, Fluorine Polymer Oil, or Heavy-Water Ice.* Physics of Atomic Nuclei, 66:1820–1830, Oktober 2003.

[36] Koster, M.P.: *Constructieprincipes voor het nauwkeurig bewegen en positioneren.* Twente University Press and others, 2008.

[37] P.A., Schmidt Wellenburg: *Production of ultracold neutrons in superfluid helium under pressure*, 2009.

[38] Mampe, W., L. N. Bondarenko, V. I. Morozov, Yu. N. Panin und A. I. Fomin: *Measuring neutron lifetime by storing ultracold neutrons and detecting inelastically scattered neutrons.* JETP Lett., 57:82–87, 1993. [Pisma Zh. Eksp. Teor. Fiz.57,77(1993)].

[39] Richardson, D.J., J.M. Pendlebury, Plamen Iaydjiev, W Mampe, Kurderrious Green und A.I. Kilvington: *Measurement of the energy dependence of the neutron loss per bounce function on reflection from oil and grease surfaces using monochromatic ultracold neutrons.* Nuclear Instruments and Methods in Physics Research Section A: Accelerators, Spectrometers, Detectors and Associated Equipment, 308:568–573, Oktober 1991.

[40] Korobkina, E, R Golub, James Butterworth, P Geltenbort und Semen Arzumanov: *Temperature dependence of ultracold neutron loss rates.* Physical Review B, 70, Juli 2004.

# Acknowledgments

Instead of a long list thanking the numerous people who contributed to the success of this thesis, I would like to conclude with a phrase from my mother tongue.

*Ned g'schimpft is globt gnuag.*

*Merce!*